RHEINISCHE FRIEDRICH–WILHELMS–UNIVERSITÄT
BONN

Starburst clusters in the Galactic center

Dissertation

zur

Erlangung des Doktorgrades (*Dr. rer. nat.*)

der

Rheinischen Friedrich–Wilhelms–Universität, Bonn

vorgelegt von
Maryam HABIBI
aus
Ghazvin, Iran

Bonn 2014

Angefertigt mit Genehmigung der Mathematisch-Naturwissenschaftlichen Fakultät
der Rheinischen Friedrich–Wilhelms–Universität Bonn

Diese Dissertation ist auf dem Hochschulschriftenserver der ULB Bonn unter
http://hss.ulb.uni-bonn.de/diss_online elektronisch publiziert

Scientific supervisor: Dr. Andrea Stolte

1. Referent: Prof. Dr. Norbert Langer
2. Referent: P.D. Dr. Jürgen Kerp
Tag der Promotion: 08.09.2014
Erscheinungsjahr: 2015

To my parents,
and those who live a belief that all great changes begin
with small steps.

Poets say science takes away from the beauty of the stars, mere globs of gas atoms. Nothing is 'mere'. I too can see the stars on a desert night, and feel them. But do I see less or more? The vastness of the heavens stretches my imagination–stuck on this carousel my little eye can catch one-million-year-old light. A vast pattern–of which I am a part... What is the pattern or the meaning or the why? It does not do harm to the mystery to know a little more about it.

Richard Feynman

RHEINISCHE FRIEDRICH–WILHELMS–UNIVERSITÄT BONN

Abstract

by Maryam Habibi

for the degree of

Doctor rerum naturalium

The central region of the Galaxy is the most active site of star formation in the Milky Way, where massive stars have formed very recently and are still forming today. The rich population of massive stars in the Galactic center provide a unique opportunity to study massive stars in their birth environment and probe their initial mass function, which is the spectrum of stellar masses at their birth. The Arches cluster is the youngest among the three massive clusters in the Galactic center, providing a collection of high-mass stars and a very dense core which makes this cluster an excellent site to address questions about massive star formation, the stellar mass function and the dynamical evolution of massive clusters in the Galactic center.

In this thesis, I perform an observational study of the Arches cluster using K_s-band imaging obtained with NAOS/CONICA at the VLT combined with Subaru/Cisco J-band data to gain a full understanding of the cluster mass distribution out to its tidal radius for the first time. Since the light from the Galactic center reaches us through the Galactic disc, the extinction correction is crucial when studying this region. I use a Bayesian method to construct a realistic extinction map of the cluster. It is shown in this study that the determination of the mass of the most massive star in the Arches cluster, which had been used in previous studies to establish an upper mass limit for the star formation process in the Milky Way, strongly depends on the assumed slope of the extinction law. Assuming the two regimes of widely used infrared extinction laws, I show that the difference can reach up to 30% for individually derived stellar masses and $\Delta A_{Ks} \sim 1$ magnitude in acquired K_s-band extinction, while the present-day mass function slope changes by ~ 0.17 dex. The present-day mass function slope derived assuming the more recent extinction law, which suggests a steeper wavelength dependence for the infrared extinction law, reveals an overpopulation of massive stars in the core ($r < 0.2$ pc) with a flat slope of $\alpha_{Nishi} = -1.50 \pm 0.35$ in comparison to the Salpeter slope of $\alpha = -2.3$. The slope of the mass function increases to $\alpha_{Nishi} = -2.21 \pm 0.27$ in the intermediate

annulus ($0.2 < r < 0.4$ pc). The mass function steepens to $\alpha_{Nishi} = -3.21 \pm 0.30$ in the outer annulus ($0.4 < r < 1.5$ pc) indicating that the outer cluster region is deficient of high-mass stars. The comparison between the observed trend in the present-day mass function of the Arches cluster to existing N-body simulations of the cluster shows that this picture is consistent with mass segregation owing to the dynamical evolution of the cluster.

Recently, more than 100 Wolf-Rayet and OB stars were identified in the Galactic center. About a third of these sources are not spatially associated with any of the known star clusters in this region. As the comparison of our observational study to N-body models of the cluster revealed, the clusters in the Galactic center region are dynamically evolved at younger ages due to their high cluster mass and the special Galactic center environment. Therefore, I probed the contribution of drifted sources from numerical models of the massive clusters in the Galactic center to the observed distribution of isolated massive sources in this region. This study shows that stars as massive as $100\,M_{\odot}$ drift away from the center of each cluster by up to $\sim$ 60 pc using the cluster models. The best analyzed model reproduces $\sim 60\%$ of the known isolated massive stars out to 80 pc from the center of the Arches cluster. This number increases to $70 - 80\%$ when we only consider the region that is $\sim$ 20 pc from the Arches cluster. Our finding shows that most of the apparently isolated high-mass stars might originate from the known star clusters. This result, together with the fact that no top-heavy mass function is required to explain the spatial variation of the mass function in the Arches cluster, implies that no evidence is seen for a deviating (top-heavy) initial mass function in the wider environment of the Galactic center.

Contents

List of Figures

List of Tables

Nomenclature

Frequently Used Symbols and Abbreviations

2MASS	Two Micron All Sky Survey
α	slope of the mass function
A	Extinction
AO	Adaptive optics
b	Galactic latitude
EL	Extinction law
CCD	Color-color diagram
CMD	Color-magnitude diagram
CMZ	Central molecular zone
Dec.	Declination
DIT	Detector integration time
F	Field of observation
FWHM	Full width at half maximum
GC	Galactic center
GPS	Galactic Plane Survey
HST	Hubble Space Telescope
IMF	Initial mass function
l	Galactic longitude
LBV	Luminous blue variable
L	Luminosity
LMC	Large Magellanic Cloud
m	Mass (or apparent magnitude)
NACO	NAOS-CONICA
ONC	Orion Nebula Cluster
P	probability
Paα	Paschen-α
PDMF	Present-day mass function
PSF	Point-spread function
r	Distance
R.A.	Right ascension
t	Time
UKIDSS	UKIRT Infrared Deep Sky Survey
v	Speed

VLT	Very Large Telescope
WFC3	Wide Field Camera 3
WR	Wolf-Rayet stars
WN	Nitrogen-rich Wolf-Rayet stars
WC	Carbon-rich Wolf-Rayet stars
YMC	Young massive clusters

Physical and Astronomical Constants

Speed of light	$c = 2.9979 \times 10^{10}\,\mathrm{cm\,sec^{-1}}$
Parsec (1 pc)	$= 3.086 \times 10^{18}\,\mathrm{cm}$
Solar mass ($1\,\mathrm{M_\odot}$)	$= 1.989 \times 10^{27}\,\mathrm{gr}$
Solar radius ($1\,\mathrm{R_\odot}$)	$= 6.960 \times 10^{10}\,\mathrm{cm}$
Solar luminosity ($1\,\mathrm{L_\odot}$)	$= 3.9 \times 10^{33}\,\mathrm{erg\,s^{-1}}$

Chapter 1

Introduction

Contents

1.1 Massive stars

The spatial distribution of stars and their mass spectrum are profound characteristics of the stellar content of galaxies. Only through understanding the basic properties of the stellar population in our nearby universe, where we can to some extent resolve stars, we are able to study distant galaxies. Among all the stars, massive stars play a dominant role regarding how they shape their environment via their radiation, their mechanical feedback and dispersal of heavy elements. To reach a full understanding of their formation precesses and properties as a population isiouefore an important goal of current astrophysics.

1.1.1 Spatial distribution of massive stars

The spatial distribution of stars and particularly massive stars can provide us with traces of their formation. This information has important implications on our understanding of how the stellar initial mass distribution is sampled, that is, in what order the stars are formed. The very influential work by Lada & Lada (2003) constructed

a catalog of studied embedded young regions within $\sim$ 2 kpc of the sun which was complete within a few hundred parsecs of the Sun. Their study was based on the astronomical literature between 1988 and 2003. They defined a cluster as a group of 35 or more spatially related stars above field-star background, whose stellar mass density is greater than $1.0\,M_{\odot}/pc^2$. According to this definition, Lada & Lada (2003) determined that $\sim$ 90% of all young observed stars in the catalog are located in clusters. Their finding was later modified by higher resolution mid-infrared data from the Spitzer Space Telescope (Werner et al., 2004) which allows for a better differentiation of young stellar objects from field stars. Many surveys of nearby embedded clusters were carried out using Spitzer (e.g., Gutermuth et al. 2011, Allen et al. 2007). Although previous studies showed that there is no characterizing density for the population of young stars which allows one to distinguish clusters from the extended field distribution (Allen et al., 2007; Bressert et al., 2010), they agree that in the nearest 1 kpc about 75% of the embedded stars are in groups with 10 or more members (Carpenter, 2000; Allen et al., 2007). Among the aforementioned 75% young stars, approximately 80% are observed in clusters with more than 100 stars (Lada & Lada, 2003; Porras et al., 2003; Allen et al., 2007).

Studies which focused on massive stars in our Galaxy obtained a higher fraction of stars formed in clusters. A comprehensive study on a group of massive Galactic O-type field stars (de Wit et al., 2004, 2005) shows that more than 95% of all O-type stars can be considered as formed within a cluster environment. Further studies revealed that even some of the remaining 5% may be run-away stars (Gvaramadze & Bomans, 2008). Schilbach & Röser (2008) studied the origins of field O-stars in the nearest 2-3 kpc around the Sun and could associate the origin of $\sim$ 91% of the observed stars to groups and clusters.

Although various definitions of a massive star and group environment yield a different fraction of stars formed in clusters, it is confirmed that the majority of massive stars form in a group environment. For the remaining population of a few percent the question of their origin is not solved.

1.1.2 The initial mass function: general theory and the upper initial mass function

The stellar mass is the most important parameter which determines the fate of a star. The mass function of stars, the relative numbers of stars as a function of their mass, is one of the key observables which can guide us to understand stellar origins and evolution. The spectrum of stellar masses at their birth, known as the initial mass function (IMF), is of fundamental importance as it is the direct outcome of star formation and determines the chemical and the kinematic feedback of the star formation process.

The observational effort to measure the initial mass function started with Salpeter (1955), who studied the distribution of field stars in the solar neighbourhood. This study adopted a power-law distribution of the form

$$dN/dm \propto m^{\alpha}, \tag{1.1}$$

where m is the stellar mass and N is the number of stars within the mass interval $[m, m+dm]$. A power-law function with a power law exponent of $\alpha = -2$ represents a distribution with equal amounts of mass per equal-sized logarithmic mass ranges, for instance $1-10\,M_{\odot}$ and $10-100\,M_{\odot}$ bins. For $\alpha < -2$, the amount of mass per equal-sized logarithmic mass bin is larger for the lower mass bins. Salpeter (1955) measured the index α, known as the slope of the IMF, to be -2.35, by fitting observational data. The pioneering study by Salpeter (1955) which derived the IMF from old field stars corrected for their age, led to an extensive number of observational and theoretical studies of the IMF in different environments. In particular clusters were extensively studied since they provide a coeval population with the same chemical composition at a common distance, that preclude large uncertainties hindering studies of the field star IMF (Kroupa 2001; Chabrier 2005; Bastian, Covey & Meyer 2010; Kroupa et al. 2013; Offner et al. 2013; Paresce & De Marchi 2000, and references therein). These different studies yielded approximately consistent IMFs irrespective of the formation epoch and cluster environment (Fig. 1.1).

The suggested power-law form of the IMF by Salpeter (1955) diverges as mass decreases, which implies a piecewise function or a continuous function with a turnover at low masses. There are various functional representations suggested for the IMF. For example, Chabrier (2003, 2005) proposed a log-normal distribution of low masses coupled with a power-law function above the peak of the IMF at $1\,M_{\odot}$. The suggested sequence of power-laws in different mass ranges by Kroupa (2001, 2002), is as follows

$$dN/dm \propto \begin{cases} m^{0.3} & , 0.08 M_{\odot} < m \\ m^{-1.3} & , 0.08 < m \leq 0.5\,M_{\odot} \\ m^{-2.3} & , 0.5 < m \leq 150\,M_{\odot} \end{cases} . \tag{1.2}$$

The stellar population with masses above $0.5-1 M_{\odot}$ constitute the higher mass single power law part of the mass function, $\alpha = -2.3$, which is considered the "standard slope" of the mass function in this mass range. The various suggested functional forms of the IMF agree with each other in the massive range within the observational uncertainties. However, determining the mass spectrum of massive stars is observationally challenging. The population of Galatic field stars do not reflect the IMF of massive stars due to their fast mass-loss/mass transfer, and short life-times. The only observable mass spectrum is the present-day mass function (PDMF) of stars. As discussed in Sect. 1.1.1, massive stars tend to form in groups and clusters. The dynamical evolution of the birth cluster leads to the rearrangement of the distribution of stars. Dynamical processes like mass segregation and cluster dynamical mass loss complicate the determination of the IMF in clusters. Finally, massive stars are more likely to have companions compared to lower mass stars (Sana et al., 2012; de Mink et al., 2013). At present, it is not feasible to resolve binaries or correct for binarity of the measured photometric high-mass IMF in clusters. However, as shown by statistical studies by

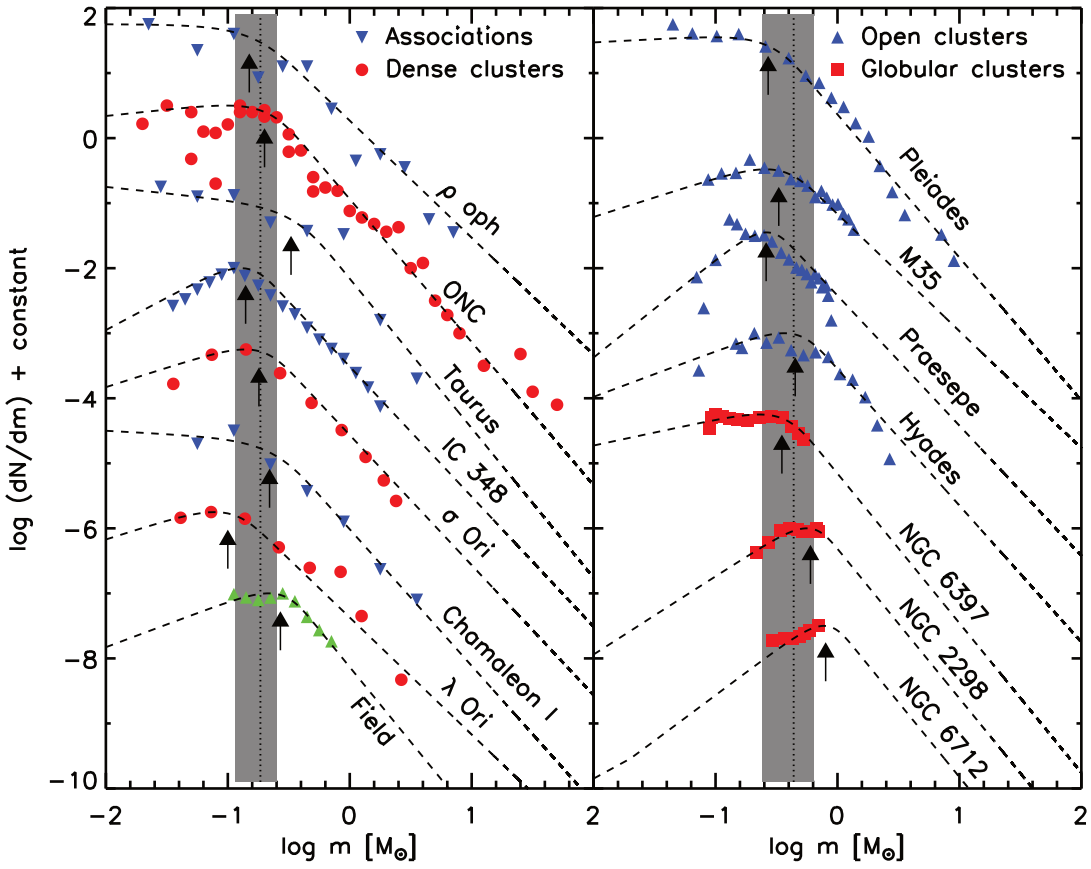

Figure 1.1: The derived present-day mass function for some young clusters and associations (left) and some older open and globular clusters (right) (Bastian, Covey & Meyer 2010 and references therein). The field star IMF is also presented at the bottom of the left panel. The mean characteristic mass in each cluster is shown with the shaded gray region, separately for each panel. The dashed lines represent fitted segmented power-laws to the mass function of each cluster. The image is taken from Bastian, Covey & Meyer (2010).

Maíz Apellániz (2008) and Weidner, Kroupa & Maschberger (2009), the power-law index of the observed mass function for massive stars is not dramatically altered due to unresolved binaries. Weidner, Kroupa & Maschberger (2009) showed that the observed power-law index of the mass function agrees with the underlying true stellar IMF to within 0.1 dex, even if all massive stars reside in binary or multiple systems. A different approach by Schneider et al. (2014), which modeled the observed mass functions of the young Galactic Arches and Quintuplet clusters using their rapid binary evolution code, shows that the mass change of the most massive stars and their companions leave characteristic signatures in the observed upper mass function. Apart from the debated role of binaries or multiple systems on the observed slope of the high-mass IMF, they can appear as super-massive stars and affect our mass estimate of the most massive stars.

1.1.3 The upper mass limit

One of the open questions in the study of the high-mass IMF is to determine a possible upper limit to the masses of stars. It is of great interest to answer whether the possible observed upper mass limit of the mass function is a physical limit rather than a statistical one. Previously, the origin of the observed upper limit of stellar mass was attributed to the Eddington limit, which is based on the balance between the outward pressure of the star's radiation and the inward gravitational force (Eddington, 1926). It was suggested that stars more massive than $60\,M_{\odot}$ become unstable to pulsations (Schwarzschild & Härm, 1959), however, later studies showed that the pulsations may be damped up (e.g., Beech & Mitalas 1994). Simulations can produce the main sequence evolution of massive stars even for a supermassive star of $10^5 M_{\odot}$ (Hillebrandt, Thielemann & Langer, 1987). Later studies suggested that the formation process, rather than the stability of massive stars, may limit the stellar mass. The limitation might originate from the stellar mass growth through accretion which is shown to become increasingly difficult at larger masses (Larson & Starrfield, 1971). Some star formation models found that feedback on spherical accretion entities, produce an upper mass limit (e.g.Kahn 1974; Wolfire & Cassinelli 1987). However, more recent hydrodynamic simulations present models of massive star formation through an accretion disc which produce massive stars far beyond the upper mass limit of spherical accretion (e.g. Yorke & Sonnhalter 2002; Kuiper et al. 2010).

In the last decade, many studies searched for an indication of a physical upper limit of stars in clusters. Many massive young clusters, $M_{cluster} > 10^4 M_{\odot}$, were observed to have an upper cutoff mass. Studies based on observations of the Arches cluster in the Galactic center region (Figer, 2005), R136 in the Large Magellanic Cloud (LMC) (Weidner & Kroupa, 2004; Koen, 2006), and statistical methods compared with observations of the Milky Way and LMC associations (Oey & Clarke, 2005), suggested an upper limit of $140 - 200\,M_{\odot}$ for the mass distribution of stars. However, these findings are challenged by more recent observations of the R136 cluster in the LMC by Crowther et al. (2010), which propose an upper mass limit as high as $\sim 300\,M_{\odot}$. On the theoretical side, recent simulations suggest that limitations from the stellar

evolution or star formation may be breached by the dynamical merger of less massive stars (Schneider et al., 2014) or mass transfer in binary systems (e.g., Portegies Zwart et al. 1999; Banerjee, Kroupa & Oh 2012.)

The theoretical investigation to understand the formation and evolution of the most massive stars which ultimately help us to explain the observed upper mass cutoff is an ongoing effort. However, the observational estimates for an upper mass limit is likely to be affected by uncertainties due to unresolved binaries, extinction correction toward the target cluster and crowding in the core of the cluster.

1.1.4 Young massive clusters

Young clusters are excellent laboratories to observe the IMF. They host a population of coeval stars with similar metallicities, located at the same distance. Young massive clusters (YMCs), with $M_{cluster} > 10^4 M_{\odot}$ and $age \leq 10\,\mathrm{Myr}$, together with OB associations, are the only and unique environments to constrain the mass distribution of short lived high-mass stars. The properties of YMCs are the key to probe star formation in extreme conditions of dense clusters, such as the ionizing flux and the kinematic feedback from nearby massive stars.

Currently, five YMCs are found in the Milky Way Galaxy and are extensively studied. Two of these YMCs are formed in the Milky Way's spiral arms. The most massive YMC known today in our Galaxy is Westerlund 1 which is located at the relatively close distance of 4 kpc (Gennaro et al., 2011; Kudryavtseva et al., 2012). This cluster is observed to have a flat IMF within its core (Brandner et al., 2008; Gennaro et al., 2011; Lim et al., 2013). While all studies confirm the steepening of the slope of the mass function in the outer parts, different studies on the observed global mass function of the cluster are inconsistent. Gennaro et al. (2011) reported a normal IMF, although Lim et al. (2013) find a flat IMF compared to the standard mass function slope (i.e., -2.3)[1]. The other somewhat less massive Galactic cluster NGC3603 is located at a distance of $\sim$ 6kpc (Stolte et al. 2004). An excess of massive stars in the core of the NGC 3603 young cluster is observed by different studies (Sung & Bessell, 2004; Stolte et al., 2004; Harayama, Eisenhauer & Martins, 2008; Pang et al., 2013). The latest study of NGC 3603 YC found a flat global slope of $\alpha = -1.88 \pm 0.15$ within $r \lesssim 1.6\,\mathrm{pc}$ for proper-motion members in the cluster (Pang et al., 2013). Three YMCs are detected in the Galactic Center region: Arches (Nagata et al., 1995; Cotera et al., 1996), Quintuplet (Okuda et al., 1990; Nagata et al., 1990) and the Young Nuclear Cluster (Becklin & Neugebauer, 1968). The three clusters are observed to have a flat PDMF within their central region (Figer et al., 1999; Stolte et al., 2005; Hußmann et al., 2012). The PDMF of the Arches and Quintuplet clusters, which are discussed with more detail in Sect. 1.2.2, steepen toward the outskirts of each cluster.

[1] Gennaro et al. (2011) and Lim et al. (2013), similar to many other mass function studies which we review throughout this thesis, have used the initial masses corresponding to the observed stellar luminosities to construct a presumable *initial* mass function. The rapid dynamical evolution of massive star clusters implies that the observed stellar mass function can be influenced by stellar evolution, as well as by the dynamical evolution of the cluster, so it does not represent the IMF even at the current young cluster age.

R136 in the 30 Dor region in the LMC is one of the few extragalactic YMCs where its stellar content is resolvable. The mass function of R136, with a mass comparable to Westerlund 1, has been visited by many studies (e.g., Selman & Melnick 2013). Massey & Hunter (1998) reported a completely normal IMF, with a slope of $\alpha \simeq -2.3$, within the mass range $2.8 - 120\,M_{\odot}$. Andersen et al. (2009) revisited the cluster to constrain the lower mass mass function in the mass range $1 - 20\,M_{\odot}$ and found a slope of $\alpha \simeq -2.2$ within the annulus $3 < r < 7\,\mathrm{pc}$.

As most YMCs exhibit flattened PDMFs in their cluster centers compared to a Salpeter-like mass function, the question whether their global mass function is normal remains unsolved. Some of these clusters clearly show signs of mass segregation (e.g., Pang et al. 2013). However, it is necessary to combine the observations of the outskirts of these clusters with their core region to probe the steepening of the mass function slope toward larger radii and compare the results with numerical simulations. Only through numerical simulations compared to the detailed observations of the mass profile of the cluster, we can determine if the observed flat PDMF of YMCs is a result of dynamical evolution or is an indication for a deviating IMF in extreme environments.

1.1.4.1 Link to extragalactic clusters

Within our local environment of $\sim 1\,\mathrm{kpc}$ from the Sun the observed IMF shows surprisingly little variation with local conditions (Salpeter, 1955; Scalo, 1998; Kroupa, 2001, 2002; Chabrier, 2005). A simple argument according to the Jeans-mass equation (see eq. 1.3) illustrates the basic dependence of star formation and the mass of the early core of the stars to the environmental conditions. In a molecular cloud, or within part of a cloud, when the outward gas pressure is not high enough to overcome the inward force of gravity, the cloud collapses gravitationally. If contraction of a massive cloud of gas and dust does not stop by increasing internal pressure, it can lead to star formation in the cloud (Jeans, 1919). The Jeans-mass equation

$$M_J \propto \rho^{-\frac{1}{2}} T^{\frac{3}{2}}, \tag{1.3}$$

shows that higher temperature can lead to the formation of heavier cores and thus effectively higher mass stars. In the warmer and dustier starburst environments, like the central region of the Galaxy, an elevated Jeans-mass can lead to formation of a stellar mass-spectrum which is dominated by massive stars and is known as *top-heavy* IMF[2]. If the IMF is so altered that more mass is formed in the upper mass bins as compared to the lower-mass stars, this implies $\alpha > -2$ (see Sec. 1.1.2).

One crucial step to understand the origin of the IMF is to contemplate in what kind of environment the IMF is likely to vary. Therefore, finding IMF variations in our local group or other galaxies is of fundamental importance to develop our understanding of the star formation process. Spiral galaxies, especially gas-rich merging spiral galaxies, can produce extraordinarily massive YMCs with masses up to $10^6\,M_{\odot}$ (e.g., YMCs

[2] Klessen, Spaans & Jappsen (2007) presented numerical hydrodynamical calculations of star-formation from warm gas in the GC and predicted a top-heavy IMF.

in the Antennae galaxies (NGC 4038/39), Whitmore et al. 1999; Mengel et al. 2002). Many extragalactic YMCs show evidence for IMF variations via indirect methods.

The most common indirect method to constrain the mass distribution of unresolved galaxies is to measure the dynamical mass of galaxies and compare their mass-to-light ratios to predictions of stellar population synthesis models. Attempts to use velocity dispersion measurements to derive the mass-to-light ratios of YMCs was started by Sternberg (1998) to study NGC 1569A and NGC 1705-1 YMCs located in two nearby dwarf galaxies. One of the most irregular studied YMCs is the cluster "F" in M82 Galaxy which its mass-to-light ratio is about three times smaller than the ratio expected from the Kroupa (2001) IMF (Smith & Gallagher, 2001) suggesting that the cluster is highly deficient in low mass stars. Various studies which attempted to measure the mass-to-light ratios of YMCs in different environments derived various results. Some studies measured mass-to-light ratios consistent with standard IMF (e.g. Larsen, Brodie & Hunter, 2004), while some found indication of top-heavy IMF (Smith & Gallagher, 2001) or bottom-heavy IMF (e.g. Mengel et al., 2002). Nevertheless, indirect extragalactic studies of the IMF in YMCs are subject to various uncertainties. For example, it is commonly assumed that clusters are in virial equilibrium. As shown by Goodwin & Bastian (2006) this assumption can be invalid for young clusters.

As mentioned above, some YMCs in our local group have properties that rival those found in globular clusters. Globular clusters are extremely massive clusters, that have a typical mass of $\sim 10^5 M_\odot$ (e.g. Harris 1996), which survive a Hubble time of dynamical evolution. The physical properties of YMCs are between of those found in typical open clusters and those in globular clusters. Local YMCs and their possible IMF variations are studied also as progenitors of massive and long-lived globular clusters, to bridge cluster formation environments in the local universe and in extra-galactic environments.

The claimed extragalactic IMF variations together with the observations of resolved local YMCs to date are among the few evidences we have to probe IMF variations in extreme environments. Among all of the resolved YMCs, those formed in the most extreme site of star formation in the Galaxy, the GC region, are valuable targets to understand the variations and origin of the IMF.

1.2 Massive stars in the Galactic center

The center of our Galaxy provides an exceptional collection of massive stars. Massive star formation in the GC region has three main components. First component is the giant molecular clouds in the region, which represent the early stage of star formation. These clouds are extraordinarily dense compared to elsewhere in the Galaxy ($n > 10^4 \mathrm{cm}^{-3}$, Morris & Serabyn 1996a) and are the birth places of the population of massive stars we see in the central few hundred parsecs of the Milky Way Galaxy. The second component is the three young and massive clusters in the GC region: The young Nuclear cluster close to the central black hole ($r < 1\,\mathrm{pc}$), the Arches and the Quintuplet clusters at projected distances of $\sim 30\,\mathrm{pc}$ from the Sgr A* (Krabbe et al., 1991; Nagata et al., 1995; Okuda et al., 1990; Becklin & Neugebauer, 1968). Finally, the third component

is population of massive stars which appear isolated throughout the GC region (Dong et al., 2011a; Mauerhan et al., 2010a,b; Wang et al., 2010). In this section, we introduce each of these components via previous studies, and as we try to do in this entire thesis, we try to introduce the role of each population in answering the main questions related to massive star formation in the GC.

The question of massive star formation in the GC is coupled with the dynamical evolution of the Arches and Quintuplet clusters. The dynamical evolution of the Arches and Quintuplet clusters not only changes the distribution of stars inside the cluster, but also changes the distribution of massive field stars in the GC region. In this thesis, we try to constrain the present-day properties of the Arches cluster, with the ultimate goal to distinguish its inherited initial properties from the properties which are appeared as a result of its dynamical evolution. In the following sections of the introduction, as we review the studies of these clusters, we try to address the link between observed properties of massive populations in the GC, and the dynamical evolution of the clusters.

1.2.1 Massive star formation in the Galactic center

The inner few hundred parsecs of the Galactic center also called the Central Molecular Zone (CMZ), contain up to 10% of the Galaxy's molecular gas (Morris & Serabyn, 1996a). The molecular gas in the CMZ form clouds with densities of $n \geq 10^4\,\mathrm{cm}^{-3}$ which is at least one order of magntude denser than molecular clouds in the disc of the Milky Way (Morris & Serabyn, 1996a). The CMZ holds few times $10^7\,M_\odot$ of molecular gas (Morris & Serabyn, 1996a; Launhardt, Zylka & Mezger, 2002a; Ferrière, Gillard & Jean, 2007) and it hosts many compact HII regions which extend mostly toward the Galactic eastern side. The presence of the YMCs in the CMZ suggests an episode of star formation with high star formation rate within the last ten Myr in the CMZ. At the present-time, the CMZ contains several sites of ongoing star formation. The star formation rate in the CMZ is measured to be $0.07 - 0.14\,\frac{\mathrm{M}_\odot}{\mathrm{yr}}$ (Yusef-Zadeh et al., 2009; An et al., 2011), which is ~ 0.1 of the total star formation in the Milky Way disc with a rate of $1.2\,\frac{\mathrm{M}_\odot}{\mathrm{yr}}$ (Lee, Murray & Rahman, 2012).

Among the star-forming regions in the CMZ, Sgr B and Sgr C are suggested to host present-day massive star formation (e.g., Mehringer & Menten 1997; Sato et al. 2000; Kendrew et al. 2013). Sgr C is the only known star-forming region in the western CMZ ($l < 0$). The Sgr B2 molecular cloud is located at a projected distance of $\sim 120\,\mathrm{pc}$ from the Galactic center (Lis & Goldsmith, 1990) in the eastern site of the CMZ (see Fig. 1.2). It contains a number of young O-type stars and compact H II regions and is known to be one of the most extreme star-forming complexes in the Milky Way (e.g. Martin & Downes, 1972; Gaume et al., 1995; Mehringer & Menten, 1997). Sgr B2 is believed to be more evolved compared to the other star-forming sites in the CMZ, especially as one of its three dense cores, Sgr B2(N) might represent an embedded stage of the formation of a massive star cluster (Qin et al., 2011). If so, the study of Sgr B2 and other massive molecular clouds in the CMZ can guide us to understand the little known stages of YMC formation. Based on the observed structure of the CO emission from the

molecular cloud near Sgr B2, i.e. a shell and a hole structure, Hasegawa et al. (1994) proposed a scenario in which a dense, massive cloud has collided with the extended less dense gas of the molecular cloud complex in the Galactic center region. Later, other observed properties like characteristic kinematic features, distortions in the magnetic field directions, and shock-enhanced molecular emission confirmed that the extreme star formation in Sgr B2 is triggered by large-scale collisions between molecular clouds (Sato et al., 2000).

Using Herschel satellite data (Pilbratt et al., 2010), Molinari et al. (2011) proposed that much of the CMZ material resides in a twisted elliptical ring that encircles the GC (see Fig. 1.2) and harbors several active sites of star formation. The structure has semi-major axes of 100×60 pc and is home to cold and dense molecular clouds. Sgr B and Sgr C are located at the eastern and the western extrema of the ring, respectively.

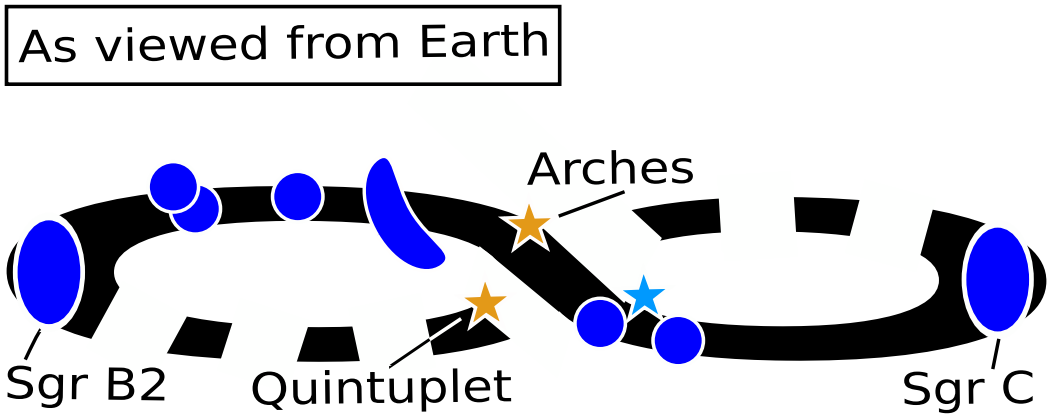

Figure 1.2: The suggested twisted elliptical ring structure with semi-major axes of 100 and 60 pc molecular gas by Molinari et al. (2011). Dashed black lines represent the far side of the ring. The light blue star illustrates the location of Sgr A*. Regions marked with darker blue illustrate the prominent molecular clouds in the region including the "Brick" which is shown by an elongated shape close to the Arches cluster. The image is taken from Longmore et al. (2013).

It is suggested that the interstellar gas subject to the gravitational potential of the bar tends to settle onto two families of stable orbits. The two families of orbits meet at the extrema of the ring introduced by Molinari et al. (2011). The x1 orbits are elongated along the Galactic bar (Binney et al., 1991; Englmaier & Gerhard, 1999). The x1 orbits enclose other systems of orbits, called x2, which are mostly aligned perpendicular to the bar and contain dense clouds. The twisted ring introduced by Molinari et al. (2011) is likely located on the x2 orbit system. One scenario is that at the two projected longitude extrema of the twisted ring, gas on x1 and x2 orbits collides and produces triggering shocks supporting star formation and leading to the formation sites of clusters in the region at the extrema of the ring, where we can observe Sgr B and Sgr C (e.g. Hasegawa et al. (1994)).

A similar scenario is suggested for the formation of the Arches and Quintuplet YMCs. Stolte et al. (2008a) discuss the possibility that a cloud-cloud collision at the boundary between x1 and x2 orbits could have triggered the formation of the Arches cluster. Related to studies which constrain the initial condition and formation scenario of the Arches-like clusters, Longmore et al. (2012) found a massive candidate YMC progenitor cloud. They used multi-wavelength data to study G0.253 + 0.016, known also as the "Brick". The Brick cloud, located between Sgr A and Sgr B2 (see Fig. 1.2) has enough mass, $1.3 \times 10^5\,M_\odot$, to produce an Arches-like cluster. The cloud is observed to have a low dust temperature, $T \sim 20K$, and high volume density, $8 \times 10^4\,\mathrm{cm}^{-3}$, and shows no sign of ongoing star formation (Longmore et al., 2012). In a study which led to the detection of three other clouds similar to the "Brick" in the CMZ, Longmore et al. (2013) suggested that passing the closest approach to Sgr A* can induce the gravitational collapse of the clouds and therefore YMC formation. Although the observed massive clouds between the Sgr A* and Sgr B2 regions have enough mass to form eventually YMCs (Longmore et al., 2013), in order to explain the formation of the Arches and Quintuplet clusters, the proposed scenario should explain the observed three-dimensional space motion of the clusters. With a young age of ~ 2.5Myr for the Arches cluster, the cluster's 3D motion should be consistent with its parent gas cloud. The direction of motion and a large proper motion of the cluster are not consistent with any of the x2 orbital families (Stolte et al., 2008a).

1.2.2 Massive clusters

1.2.2.1 The Nuclear cluster

Nuclear clusters are found in the center of many spiral and irregular galaxies (e.g., Phillips et al. 1996, Carollo, Stiavelli & Mack 1998). The nuclear cluster of the Milky Way is one of the three massive clusters in the GC region. As a cluster in the vicinity of a supermassive black hole, SgrA* (distance $\sim$ 8kpc, Ghez et al. 2008), the nuclear cluster evolves and maybe formed under different physical conditions compared to the Arches and Quintuplet clusters, which are in the focus of this thesis. Accordingly, the observed various types of stars in the nuclear cluster and their dynamical properties serve to answer different puzzling phenomena. However, many of the raised questions

by the study of the nuclear cluster demand understanding how star formation in the CMZ proceeds in general.

More than 90% of the observed stars in the central parsec of our Galaxy are low to intermediate mass stars, older than 1 Gyr, which are naturally expected in an old nuclear star cluster (Genzel, Eisenhauer & Gillessen, 2010). In addition to the population of old stars, surprisingly, the nuclear cluster contains many bright, massive young stars (e.g., Allen, Hyland & Hillier 1990; Krabbe et al. 1995; Paumard et al. 2006,). Currently, more than 170 young massive stars are observed in the central parcec which their spectral-type are identified. The majority are O and B-type supergiants and Wolf-Rayet stars (Paumard et al., 2006; Martins et al., 2008a; Bartko et al., 2009, 2010; Do et al., 2013). Among them a tight collection of mostly older B-type stars, the so-called S-stars, within the central 0.04 pc are distinguished (age: 6–400 Myr; Eisenhauer et al. 2005). S-stars are randomly oriented on near-Keplerian orbits (e.g., Schödel et al. 2003; Ghez et al. 2005).

The presence of young stars in the GC is a question usually referred to as "the paradox of youth" (Ghez et al., 2003). Does the existence of the population of young massive stars show that, in spite of the strong tidal forces near the GC, star formation must have taken place within the last few million years? The origin of these sources is still to be resolved in our understanding of the mechanisms involved in the vicinity of a black hole.

One of the main goals of observational studies of the Milky Ways's nuclear cluster is to distinguish between two possible scenarios to explain the origin of young stars in the central few parsecs: (i) Infall of a young star cluster, which is formed outside the hostile central few parsecs, toward the GC (e.g., Gerhard 2001; Portegies Zwart, McMillan & Gerhard 2003), (ii) formation of a disc structure from molecular clouds which helps to overcome high tidal shear from the black hole, where the disc quickly fragments to form stars (e.g., Bonnell & Rice 2008). It may well be that both scenarios have partly provided the observed population of young stars in the nuclear cluster. The intriguing existence of the two YMCs in the GC, the Arches and the Quintuplet, is probably the mainspring of the infall theory. It is suggested by Gerhard (2001) that a massive cluster spirals in toward the GC due to dynamical friction. As the infalling cluster becomes disrupted its young population is captured by the nuclear cluster. Studies have shown extremely massive counterparts of the Arches and Quintuplet clusters ($M \sim 10^6 M_\odot$), only if initially located at R $<$ 10 pc, can provide the observed young population in the central parsec with young stars (e.g., Kim & Morris 2003).

The origin of young stars in the nuclear cluster has led to extensive observational studies to constrain the mass function and dynamical properties of its young population. Such observations can provide constraints for the initial conditions and thus formation scenarios of the young stars in the central parsec of the Galaxy. Within the central $r \leq 0.5\,\mathrm{pc}$, the distribution of the observed massive stars in the Hertzsprung-Russell diagram and the number ratios of different sub-types indicate that most of the O/WR-stars are coeval, with an estimated age of about $4 - 6 \times 10^6$ years (e.g. Genzel et al. 1996; Paumard et al. 2006; Do et al. 2013; Lu et al. 2013). Monte Carlo analysis of the individual orbits of the young massive stars combined with their 3D velocity

information (Lu et al., 2006, 2009; Bartko et al., 2009, 2010), revealed that slightly more than half of the young stars (maximum 60%; Bartko et al. 2009, 2010) exhibit a clockwise motion on the sky in an inclined disc. It is debated if the remaining stars form a second less well-defined disc or they are distributed more isotropically (Genzel et al., 2003; Paumard et al., 2006; Lu et al., 2009).

Depending on which of the two scenarios, i.e inspiraling cluster vs. in-situ star formation, is the origin of the young stars in the nuclear cluster, we expect to observe a different spatial distribution and mass function. Bartko et al. (2010) constructed the K-band luminosity function of the young nuclear cluster. They found that in the central $\sim$ 0.04 pc and also outside the disc ($r > 0.48$ pc) the measured slops agree with a standard IMF, however, the luminosity function of the distinguished disc of young stars ($0.04 \leq r \leq 0.48$ pc) is ~ 2 dex flatter than a Salpeter-like slope. More recently, Lu et al. (2013) measured the slope of the mass function in the central 0.48 pc of cluster to be $\alpha = -1.7 \pm 0.2$, which is steeper than the previous measurement, but still significantly flatter than the standard slope. So far, the measured slope of the mass function of the young nuclear cluster provides the strongest evidence for a top-heavy IMF. We briefly discussed the effect of the environmental conditions on the IMF in Sect. 1.1.4.1. The properties of the molecular clouds in the whole central 200 pc of the Galaxy are different compared to other places in the Milky Way (see Sect. 1.2.1). However, the star formation condition within the area of a few parsecs around the black hole is extreme, even compared to the central 200 pc. Therefore, at the time it is not clear whether the IMF deviates in the entire CMZ, i.e. out to the redii where the Arches and Quintuplet clusters have formed, or just concerns the central region around the super massive black hole.

1.2.2.2 The Quintuplet cluster

The Quintuplet cluster, located at the projected distance of about 30 pc from the GC, was first noted and named for its five bright infrared stars (Okuda et al., 1990; Nagata et al., 1990). The collection of the five bright stars with many more bright infrared sources which were found later (Moneti, Glass & Moorwood, 1994; Figer, McLean & Morris, 1995; Figer, Morris & McLean, 1996) revealed the presence of a cluster in the GC region. The Quintuplet cluster, similar to the two other YMCs in the GC, is a young starburst cluster. Figer, McLean & Morris (1999) conducted a photometric and spectroscopic study on massive stars in the cluster and derived an age of 3–5 Myr based on the types of the stars they found. Later studies found an age discrepancy between the brighter WN stars and the less luminous O stars. The analysis of three WN stars by Liermann et al. (2010) favors a younger age of about 3 million years. However, OB stars in the cluster populate a 4 Myr isochrone on the HR diagram (Liermann, Hamann & Oskinova, 2012). The presence of more evolved WC stars in the cluster suggests older ages for the Quintuplet cluster, compared to the Arches which is observed to host no WC stars.

Up to now observations in the Quintuplet cluster confirm a collection of about 100 OB stars (Figer, McLean & Morris, 1999; Figer, 2004), 7 WN, 14 WC (e.g.,Homeier

et al. 2003; Liermann et al. 2010; Liermann, Hamann & Oskinova 2009), and 2 LBV stars (Geballe, Najarro & Figer, 2000; Figer et al., 1998). The total photometric mass of the Quintuplet cluster, extrapolated down to 1 $M_{\odot}$, is estimated to $\sim 1.6 \times 10^4 M_{\odot} (r <$ 1.8pc) (Hußmann, 2014).

Liermann, Hamann & Oskinova (2009) measured radial velocities of 98 early-type stars and 62 late-type stars in the Quintuplet cluster and found a mean radial velocity of $113 \pm 2\,\mathrm{km\,s^{-1}}$. From two epochs of high-spatial resolution data with VLT, Hußmann (2014) found the bulk proper motion to be $128 \pm 17\,\mathrm{km\,s^{-1}}$ parallel to the Galactic plane. Combining the measured proper motion with the previously known radial velocity of the cluster, Hußmann (2014) calculated a three-dimensional velocity of $164 \pm 17\,\mathrm{km\,s^{-1}}$ which is similar to the orbital motion of the Arches cluster (see Sect. 1.2.2.3).

The mass function of the Quintuplet cluster was derived by Hußmann et al. (2012), who discovered a slow radial trend as they constructed the present-day mass function of the Quintuplet cluster in three radial ranges. They confirmed a top-heavy mass function, $\alpha = -1.5 \pm 0.1$, in the central 0.5 pc. In the intermediate annulus of $0.6 < r < 1.2\,\mathrm{pc}$ the slope of the PDMF slightly steepens to a slope of $\alpha = -1.8 \pm 0.2$. In the outer annulus of $1.2 < r < 1.8\,\mathrm{pc}$ the slope reaches $\alpha = -2.1 \pm 0.3$, where the standard slope of the mass function is -2.3. Compared to the Arches cluster (see Sect. 1.2.2.3), the Quintuplet cluster exhibits a flat mass function within a larger area. The density of the Quintuplet cluster is calculated to be $\sim 10^{2.4} M_{\odot} pc^{-3}$ which is ~ 100 times less dense than the Arches cluster (Figer, McLean & Morris, 1999). Whether these differences arise from the longer dynamical evolution of the more evolved Quintuplet cluster or is whether they are due to different initial conditions probably needs dedicated numerical simulations of the Quintuplet cluster from its time of birth to its present age.

1.2.2.3 The Arches cluster

The Arches cluster, located at the projected distance of $\sim$ 26 pc from the Galactic center, was first found in infrared surveys by Nagata et al. (1995) and Cotera et al. (1996). The Arches cluster with an age of $\sim$ 2.5 Myr (Blum et al., 2001; Najarro et al., 2004; Martins et al., 2008b) is the youngest cluster in the GC. An estimated mass of $M_{cl} \sim 2 - 7 \times 10^4\, M_{\odot}$ (Figer et al., 1999, 2002; Espinoza, Selman & Melnick, 2009; Clarkson et al., 2012) combined with a measured half mass radius of 0.4 pc (Stolte et al., 2002) makes it one of the densest clusters in our Galaxy ($\rho = 2 \pm 0.4 \times 10^5 M_{\odot} pc^{-3}$; Espinoza, Selman & Melnick 2009).

The Arches cluster hosts more than 160 O-type stars (Figer et al., 1999; Blum et al., 2001; Figer et al., 2002; Najarro et al., 2004; Martins et al., 2008b) and 15 WNL stars (e.g. Cotera et al., 1999; Martins et al., 2008b; Mauerhan et al., 2010a). Studies which determine the age of the Arches cluster are based on spectroscopy of WN stars and O super-giants, along with the absence of WC stars that establish an upper limit for the age of the cluster (Blum et al., 2001; Najarro et al., 2004; Martins et al., 2008b). The young estimated age of the cluster implies that the most massive stars are still present. This has made the cluster a popular target for the study of the high-mass part of the mass function. Figer (2005) has studied the Arches cluster to observationally test the

existence and the amount of the upper mass limit for star formation. Assuming the most massive stars are still present in the cluster, Figer (2005) calculated an expected number of 18 stars more massive than $150M_{\odot}$ in the Arches cluster. As he could observe no star more massive than $150M_{\odot}$, he concluded that $150M_{\odot}$ is a fundamental stellar upper mass limit. In Sect. 1.3, we discuss the issue of the high extinction toward the GC, which can affect any derived individual mass based on photometry and spectroscopy. As part of this thesis, we try to quantify the effect of extinction on the main findings based on the observations of the Arches, including the claimed upper mass limit.

Different studies tried to constrain the high-mass IMF via characterizing the Arches cluster mass function. Figer et al. (1999) first showed that the PDMF of the central part of the cluster is top-heavy. This finding was later confirmed with studies which employed high-resolution data using adaptive optics (AO) instruments. Stolte et al. (2005) find a slope of -1.26 for the mass range of $10M_{\odot} < M < 63M_{\odot}$ in the inner core. Espinoza, Selman & Melnick (2009) observed a slope of -1.88 for the IMF in the cluster core. These findings were confined to the central 0.2 pc of the cluster. The intermediate annulus of $0.2 < r < 0.4$ pc is partly covered by Kim et al. (2006) and Espinoza, Selman & Melnick (2009). Kim et al. (2006) found a slope of -1.71 within the spatial range $0.2 < r < 0.35$ pc for stars with $5M_{\odot} < M < 50M_{\odot}$. Espinoza, Selman & Melnick (2009) fitted the slope of $\alpha = -2.28$ for the IMF of stars above $10M_{\odot}$. Therefore, in contrast to the core of the cluster which is confirmed to have a flat mass function, for the intermediate annulus of $0.2 < r < 0.4$ pc the reported observed slopes of the mass function do not agree. The tidal radius of the Arches cluster is estimated to be ~ 1 pc (Kim et al., 2000) which is about two times larger than the area covered by the previous studies and is yet to be observed. The observed flat slope of the mass function in the central part of the Arches cluster together with the proximity of the cluster to the GC make the cluster an excellent candidate for observing IMF variations in extreme environments. As discussed in Sect. 1.1.4.1, physical conditions like high cloud temperatures, and gas pressure are considered to influence the IMF. Morris (1993) and Klessen, Spaans & Jappsen (2007) discussed characteristics of the interstellar medium in the GC, for example high cloud temperatures and strong magnetic fields. They concluded that the special cloud conditions in the GC lead to a larger Jeans mass, compared to other parts of the Galaxy. However, the Jeans mass is not strictly related to the IMF, therefore increased Jeans mass is not enough evidence for a top-heavy IMF alone. Some studies like Elmegreen, Klessen & Wilson (2008) show the Jeans mass depends weakly on density, metallicity, temperature, and the radiation field which may lead to IMF variations that are too small to be observable.

The question of the IMF of the Arches cluster is coupled with the dynamical evolution of the cluster. The dynamical evolution of star clusters in the GC region can become dramatic under the strong effect of the GC tidal field. Simulations of the dynamical evolution of the cluster by Kim et al. (2006) showed that the observed flat IMF may be the effect of mass segregation. A study by Harfst, Portegies Zwart & Stolte (2010) implemented N-body simulations of the Arches cluster to investigate the internal dynamical evolution of the cluster. By comparing their models to the available

observational data within the central 0.4 pc of the Arches cluster, they could constrain the initial conditions and construct a dynamical model of the Arches cluster that best represented the central PDMF. From this model, a steep increase of the stellar mass function slope as a function of the cluster center distance was predicted. In this thesis, we try to extend the observational studies of the Arches cluster toward larger radii up to its tidal radius. By observing the outskirts of the cluster for the first time, we try to constrain the spatial variation of the mass function through the cluster and compare it to dynamical simulations of the cluster over its lifetime.

To understand the present-day properties of the Arches and the Quintuplet clusters, we need to constrain the dynamical evolutionary stages of both clusters. This goal is achievable only if we can trace back the evolution of the cluster during it's life-time. Previous studies constrained the orbital motion of the Arches cluster. The line-of-sight velocity of the Arches cluster is $\sim 95\,\mathrm{km\,s^{-1}}$ (Figer et al., 2002). Stolte et al. (2008a) determined the proper motion of the Arches cluster and found a 2D velocity of $212\,\mathrm{km\,s^{-1}}$ parallel to the Galactic plane. The proper motion of the cluster was later revised to a slightly lower value of $172 \pm 15\,\mathrm{km\,s^{-1}}$ (Clarkson et al., 2012). Because of the uncertainty in the cluster's distance along the line of sight, the exact formation site and the orbit of the cluster is not verified. However, Stolte et al. (2008a) discussed the formation of the Arches cluster inside the central 200 pc of the Galaxy as one of the most likely formation scenarios. In this thesis, we analyze more detailed models of the Arches and Quintuplet clusters, in order to study the evolution of the clusters as they move along their orbits. The detailed study of the evolution of the Arches and Quintuplet clusters can also guide us to understand the massive field stars in the GC region.

1.2.3 Isolated massive stars

As discussed in the three previous chapters, the GC region hosts three starburst clusters with masses in excess of $\sim 10^4\,M_\odot$. Recent observations of isolated stars in the GC region revealed that the field stars in this area, similar to these three clusters, encompass many massive sources (Dong et al. 2011a; Mauerhan et al. 2010a; Mauerhan et al. 2010b; Wang et al. 2010). A population of distributed, massive WR stars with initial masses in excess of $20-40\,M_\odot$ were detected within the central $91\times35\mathrm{pc}^2$ of the Galaxy by X-ray observations, which are accompanied by spectroscopic studies and Paschen-α (Paα) narrow-band imaging with the Hubble Space Telescope (HST) (Wang et al. 2010; Dong et al. 2011a). Up to now, more than 100 WR stars and O supergiants have been spectroscopically identified in the Galactic center region (Mauerhan et al., 2010a), including the known cluster members.

As about a third of these sources are located outside of the three massive starburst clusters, it was suggested that they provide evidence for *isolated* high-mass star formation in the GC (Dong et al. 2011b, Oskinova et al. 2013). As discussed in Sect. 1.1.1, observations of massive stars in the solar neighborhood show that generally massive stars form in groups and associations (Lada & Lada 2003; Zinnecker & Yorke 2007; Gvaramadze & Bomans 2008), but it is not clear if we can generalize these findings to

different Galactic environments. On the other hand, the dynamical evolution of stellar populations in the GC region can become dramatic under the strong effect of the GC tidal field. If so, dense and massive clusters like the Arches and Quintuplet can shape the distribution of the field stars in this region.

The Arches and Quintuplet clusters are observed to be already mass segregated at ages of $2-6\,\mathrm{Myr}$. The Quintuplet cluster at an age of 3-5 Myr exhibits a flat mass function slope of -1.5 ± 0.1 in the cluster center compared to the standard Salpeter (1955) initial mass function (IMF) of -2.3 (Hußmann et al., 2012). A similarly flat mass function was found in the central region of the Arches cluster, the slope of which may increase toward larger radii (Figer et al. 1999, Stolte et al. 2005, Espinoza, Selman & Melnick 2009, see also Sect. 1.2.2.3). The dynamical evolution of the Arches and Quintuplet clusters, however, not only changes the distribution of stars inside the cluster, but also changes the distribution of field stars in the GC region. Through gravitational interactions between stars in dense, compact clusters, stars can accelerate to become runaways (e.g., Poveda, Ruiz & Allen 1967; Gies & Bolton 1986). Moreover, the dynamical evolution of clusters under the influence of the Galactic tidal field leads to the formation of tidal arms. These tidal structures are mostly observed for globular clusters, which evolve for many Gyrs (e.g., Odenkirchen et al. 2001). As massive clusters in the GC dissolve within a few Myrs (Kim et al. 2000; Portegies Zwart et al. 2001a), dynamical evolution under the effects of the strong tidal field of the GC leads to the formation of extended tidal structures during shorter timescales. These tidal structures, in turn, can significantly contribute to the field stars in the GC region.

As part of this thesis, we analyze the best-fitting Arches model presented by Harfst, Portegies Zwart & Stolte (2010), which is extended to incorporate the effect of the Galactic center tidal field, to investigate the contribution of the Arches and Quintuplet clusters to the observed population of isolated massive stars detected by Mauerhan et al. (2010a).

1.3 Extinction toward the Galactic center

The center of our Galaxy is the most extreme site of massive star formation in the Milky Way where we can resolve the stellar content. However, the investigation of its stellar content is hampered by high extinction. A visual extinction of up to 30 magnitudes allows the GC to only be accessed in the radio, infrared, and X-ray regimes. The extinction toward the GC is caused by the diffuse interstellar medium (Lebofsky 1979), as well as dense molecular clouds in the central molecular zone (Morris & Serabyn 1996a). The latter are suggested to contribute one-third of the total extinction (Williams, Blitz & McKee 2000). The substructure of molecular clouds (e.g., Williams, Blitz & McKee, 2000) causes patchy extinction along the GC line of sight.

The line-of-sight extinction toward the GC was first investigated by Becklin & Neugebauer (1968). The visual to near-infrared extinction law was derived by Rieke & Lebofsky (1985) by studying the color excess of five supergiants near the GC and the star o Sco in the upper scorpius region. The extinction derived by Rieke & Lebofsky

(1985) was later fitted to a power law $A_\lambda \propto \lambda^{-1.61}$ (Cardelli, Clayton & Mathis, 1989) and considered in many studies as the standard extinction law toward the GC. Later studies analyzed nebular hydrogen lines (eg. Lutz et al., 1996), near-infrared surveys (Nishiyama et al., 2009; Stead & Hoare, 2009), and the photometry of red clump stars in the GC (Schödel et al., 2010). They have revealed that the near-infrared extinction law in the range of the J, H, and K_s bands is better described by a steeper power law with an index of $\alpha \sim -2.0$.

The slope of the extinction law influences the derivation of individual masses from the luminosities of cluster members, so is expected to influence the shape of the stellar mass function and to have an especially severe impact on the upper mass limit derived from comparison with stellar evolution models. As part of this thesis, we study the effects of the new regime of the steeper near-infrared extinction law on the derivation of individual stellar parameters toward one of the three massive clusters in the GC, the Arches cluster.

1.4 Brief outline of this thesis

In this thesis, we analyze high-spacial resolution observations of the Arches cluster out to the cluster's tidal radius for the first time. The Chapter 2 of the thesis is devoted to explain the observations of the Arches cluster and the data reduction steps. We determine individual extinction values and stellar masses of the cluster members in Chapter 3. As part of Chapter 3, Sect. 3.2 , we construct the extinction map of the cluster and study the effects of the new regime of steeper near-infrared extinction laws on the derivation of individual stellar parameters toward the Arches cluster. We show the effect of extinction law assumptions on previous observation of the cluster to establish an upper mass limit for the star formation process in the Milky Way. In Chapter 3, Sect. 3.3, we construct the PDMF of the Arches cluster for an area that reaches approximately to the tidal radius of the cluster. We probe the radial variation in the slope of the mass function and compare it with the existing dynamical models of the cluster in order to distinguish between primordial or dynamical mass segregation in the Arches cluster.

Based on our findings in Chapter 3, we investigate the dynamical evolution of the Arches and Quintuplet clusters in Chapter 4 to probe the contribution of drifted sources from both star clusters to the observed population of isolated massive stars in the GC. We present a grid of different models based on distinct physical assumptions and a method to find the best-matching model to reproduce the observations in Sect. 4.3.2 of Chapter 4. A summary of our findings followed by an outlook for future studies is presented in Sect. 5.

Chapter 2

Observations and data reduction

Sections 2.1 and 2.2 of this chapter are based on Section 2 of the publication in Astronomy & Astrophysics: "The Arches cluster out to its tidal radius: dynamical mass segregation and the effect of the extinction law on the stellar mass function.", Habibi, M., Stolte, A., Brandner, W., Hußmann, B., & Motohara, K. 2013, A&A, 556, A26.

Contents

2.1 Observations

K_s-band images ($\lambda_c = 2.18\mu$m, $\triangle\lambda = 0.35\mu$m) of the outer parts of the Arches cluster were obtained on June 6-10, 2008, with the Very Large Telescope (VLT). Images were acquired with the near-infrared camera CONICA (Lenzen et al., 2003). The atmospheric turbulence was corrected with the AO system NAOS to enhance the spatial resolution (Rousset et al., 2003). We used the brightest star in K_s in each field as the natural guide source for the infrared wave-front sensor. Since the available natural guide stars are with $9.2 < K_s < 10.4$ mag at the faint limit of the infrared wave-front sensor magnitude range, we had to use the N90C10 dichroic, which distributes 90% of the light to NAOS, while only 10% is delivered to the science detector. We used Fowler sampling to enhance the sensitivity that allowed us to detect sources as faint as $K_s = 17$ mag (Fig. 2.1). The acquired images cover four fields of 27.8" × 27.8" each, provided by the medium-resolution camera (S27) with a pixel scale of 0.027"/pixel.

On each of the four fields we obtained 44 dithered images with a detector integration time of 15 s and two exposures (NDIT=2), yielding 30 s of total exposure time per frame. We refer to the four outer fields as fields two to five. Small dither shifts with a maximum of 2" allowed a good background subtraction using the science frames, while at the same time the optical distortions at the edges were minimized. During the K_s-band observations, the natural visual seeing varied from 0.61" to 0.98" (see Table 2.1). We achieved typical spatial resolutions of three to four pixels (0.081"-0.135") on individual frames using this AO setup. The properties of all fields are summarized in Table 2.1.

Seeing-limited J-band ($\lambda_c = 1.25\mu$m, $\triangle\lambda = 0.16\mu$m) observations were performed on July 17, 2000, with the 8.2 meter Subaru optical-infrared Telescope on Hawai'i (Iye et al. 2004) under excellent weather conditions. The CISCO spectrograph and camera (Motohara et al. 2002) provided a pixel scale of 0.116"/pixel and a field of view of $2' \times 2'$. We obtained 86 dithered J-band images with 10 s exposure time per image. An average seeing of 0.49" resulted into a full width at half maximum (FWHM) of the point-spread function (PSF) of 0.39" on the combined image (Table 2.1). The locations of the NACO fields overlaid on the Subaru J-band image are shown in Fig. 2.2. The luminosity functions (Fig. 2.1) illustrate that the detection limits on the combined images are $J < 21.5$ mag (CISCO) and $K_s < 17$ mag (NACO) in fields 2-5 (hereafter referred to as "outskirts of the cluster"). For K_s-band data in the field 1 we used a detection limit of 17.5 mag. The H-band was limited by the applied K-band detection limit.

For calibration purposes, two calibration fields in the K_s-band were applied. These frames obtained on June 6-12, 2012, with the NAOS/CONICA instrument (Table 2.1). Each frame was positioned to have a large overlap area with two of the outskirts fields and small overlap field area with the central field (see Fig. 2.2). These calibration frames together with the NACO ground-based photometry of Espinoza, Selman & Melnick (2009) were applied to calibrated fields 1, 3, 4, and 5. Only for calibration of field 2, we used the Galactic Plane Survey (GPS) of the UKIRT Infrared Deep Sky Survey (UKIDSS). The UKIDSS survey started in 2005 using the wide field camera on the United Kingdom Infrared Telescope on Mauna Kea, Hawai'i. The GPS covered an area of 1800 square degrees in JHK to a depth of $K = 19$ mag and $J = 20$ mag (Lucas et al., 2008).

We used the NAOS-CONICA observations obtained in March 2002 in the central part of the Arches cluster to cover the whole cluster area. A visual guide star with V=16.2 mag was used as the guide probe for the visual wave-front sensor. The data properties and reduction steps are described in Stolte et al. (2005) (see also Stolte (2003) for details). In this paper, we label this dataset as field 1.

2.2 Data reduction

In a CCD imaging, the collected charge during the exposure time, t_e, at a particular pixel located at (p, q) on the detector can be written as:

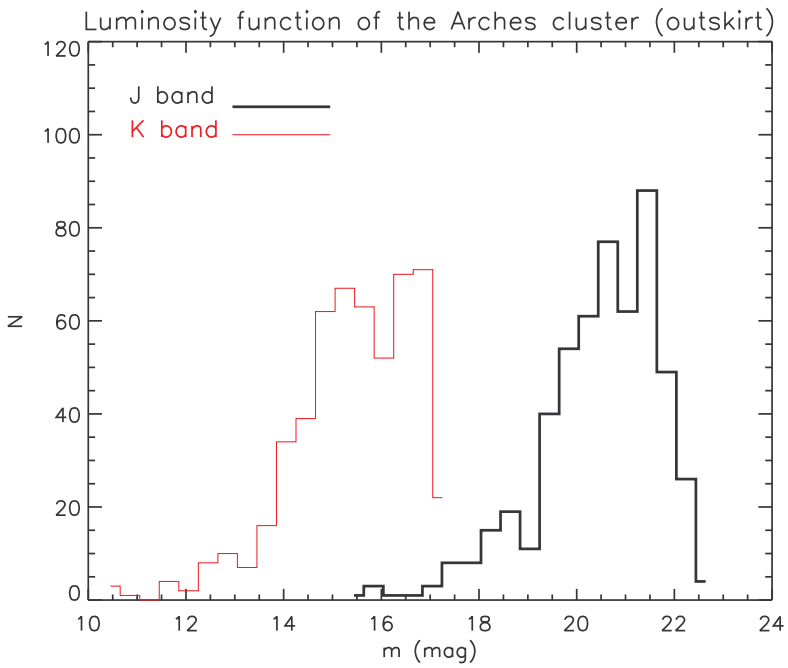

Figure 2.1: Luminosity functions of all detected sources in the outskirts of the cluster (field 2-5, see Fig. 2.2) in J-band and K_s-band. The luminosity at which the number of stars decreases represents the detection limit of 21.5 mag and 17 mag on the CISCO J-band and NACO K_s-band images, respectively.

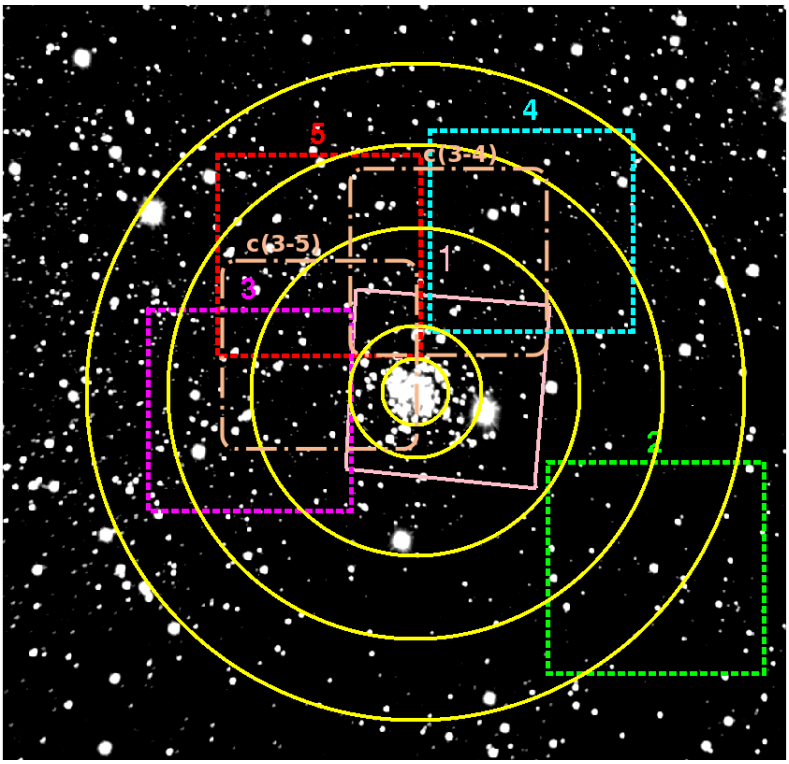

Figure 2.2: The locations of the NACO fields (K_s-band observations) overlaid on the Subaru/CISCO J-band image of the Arches cluster. Circles illustrate distances of 0.2, 0.4, 1, 1.5, and 2 pc from the center of the cluster. The central field (field 1) was observed in K_s and H. The two dot-dashed boxes represent the K_s calibration frames (see Sect. 2.2.5). North is up and east to the left.

Table 2.1: Overview of the observations.

Field	Date	Filter	DIT × NDIT (s)[a]	N_{frames}	N_{use}	Airmass	Seeing[b] ($''$)	FWHM of PSF ($''$)
VLT / NACO								
field 1 (center)	2002-03-30	H	30.00×2	35	14	1.15	0.8	0.084
field 1 (center)	2002-03-30	K_s	15.00×4	15	7	1.15	0.8	0.084
field 2 (outskirt)	2008-06-06	K_s	15.00×3	44	38	1.01	0.61–0.78	0.073
field 3 (outskirt)	2008-06-06	K_s	15.00×3	44	32	1.06	0.69–0.92	0.089
field 4 (outskirt)	2008-06-06	K_s	15.00×3	44	33	1.14	0.78–0.98	0.079
field 5 (outskirt)	2008-06-10	K_s	15.00×3	44	30	1.01	0.7–0.84	0.116
Suburu / Cisco								
wide field	2000-07-17	J	10.00×1	86	72	1.72	–	0.39
Calibration fields								
calib3-5	2012-06-12	K_s	3.00×1	88	88	1.01	0.78	0.151
calib4-5	2012-06-12	K_s	3.00×1	71	71	1.72	0.9	0.108

[a] Integration time for each exposure × number of exposures.
[b] Optical (V-band) seeing.

$$N_{total}(p,q) = N_d(t_e,p,q) + N_s(p,q)F(p,q) + N_o(p,q)F(p,q) \quad (2.1)$$

where N_d represents the dark signal, F is the efficiency in each pixel, N_s is the sky background signal and N_o is the signal received from the target objects. The dark signal of near-infrared detectors is composed of detector bias and dark current. The "bias" is the zero level offset and is the noise due to the electronics. It also contains the dark current from thermally excited electrons. The dark current of the near-infrared detectors is small, so the dominant feature in dark signal is the detector bias. Since the dark current is a function of the time, the dark signal is also dependent on the exposure time, t_e. The sky signal and flux coming from the target stars are assumed not to be variable. Both the sky and the astronomical signals are modulated by a flat field showed by the function $F(p,q)$ in equation 2.1. Flat fields account for illumination functions of the telescope and the instruments, and also the sensitivity variation of the detector which can be different for each pixel. Flat fields are usually obtained by observing a uniformly illuminated source like a halogen lamp or observing the sky at twilight, when the sky is much brighter than astronomical sources.

In the following sub-sections we explain the data reduction steps performed to derive the masterdark, mastersky, and the flat frames to calibrate our data. The data taken by Subaru/CISCO was reduced manually using IRAF routines. In order to reduce the VLT/NACO data, we used a self-developed data reduction pipeline. The body of this pipeline was written in Python, and it invokes several IRAF[1] tasks (Tody, 1993), as well as custom-made IDL and Python routines. The details of the NACO pipeline data reduction are summarized in Hußmann (2014).

2.2.1 Subaru/CISCO data reduction

2.2.1.1 Dark and flat calibration frames

The CISCO data were reduced within IRAF and by employing some custom-made IDL routines. Dark calibration frames, which are frames without detector illumination, were taken with 10 s exposure time, similar to the science frames. Dark frames were combined to create a master dark frame using the `imcombine` task of the IRAF. We used the `minmax` option to reject the hot or dead pixels and create a preliminary bad pixel mask. The masterdark frame is subtracted from all the science and sky frames.

To obtain the pixel sensitivity as a function of brightness variation in each pixel, 47 twilight flat frames were used, which were taken off-cluster in the evening before the observations. We excluded two twilight flat frames whose median flux was above the linearity limit of the detector, which is 10000 ADU (analog to digital units). Prior to construction of a master flat, the masterdark with the same DIT as the twilight flats (10 s) was subtracted from each twilight frame. The flat frames were coadded using the routine `imcombine` with scale parameter set to `mode`, which scales the images to a

[1]IRAF is distributed by the National Optical Astronomy Observatory, which is operated by the Association of Universities for Research in Astronomy (AURA) under cooperative agreement with the National Science Foundation.

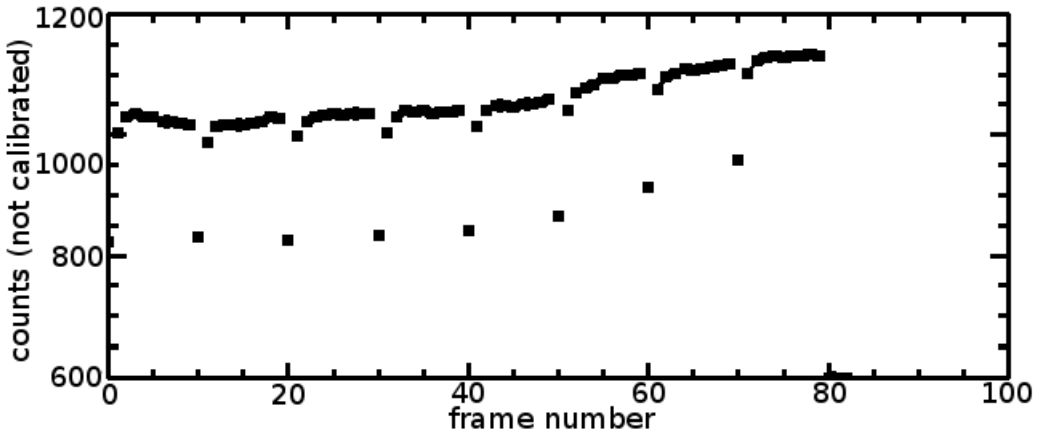

Figure 2.3: The background level of individual frames taken with Subaru/CISCO is plotted in counts. After each shift of the telescope a discontinuity of $\sim 66\%$ was present in the background level of the frames. By scaling images to their background level the trend was removed.

common mode before co-adding them. All the sky and science images were divided by the normalized masterflat. Each time we combined a stack of dark frames or flat frames to create a master calibration image, a bad pixel mask was created which contains pixels rejected as outliers. These masks were later applied in final science frames combination.

2.2.1.2 Sky subtraction

Comparing the background level of the sky frames revealed an obvious trend with discontinuities present in the background level. In the first, second, and the third frames of the series of twelve exposures taken at each position, the background level was lower than in later frames. The continuous part of the bias level was increasing with time (Fig. 2.3). The trend was the result of moving and resetting the telescope to capture dithered images which resulted in bias level variations. The background level was 66% lower in the first image after each shift compared to the mean background of images 2-12 [2]. The same pattern was present in the science frames which were taken using the dither mode of the telescope. The first sky image after each dither with a significant bias level difference was discarded to ensure a homogeneous background correction. The remaining images were divided into three groups according to their background levels. Science frames were also categorized according to their background level. Each sky image was scaled to the mean background count of its group using the `imarith` routine of the IRAF. The best result was achieved when the sky frames of each group were separately combined to a mastersky and subtracted from the corresponding group of science frames. This sky reduction procedure was hence used for all science frames.

[2]This instrumental issue is known as "reset anomaly" and is well known for many HAWAII arrays (see e.g. http://www.ast.cam.ac.uk/~optics/cirsi/documents/resetanomaly.html).

2.2.1.3 Coadding science frames

In order to coadd the images, they must be previously aligned. We used the cross-correlation technique provided by the IRAF/drizzle package (Fruchter & Hook, 2002) to precisely estimate the offsets between the images. Prior to cross-correlation, the cosmic rays, background and hot pixels were removed using the task `precor` of IRAF. Using the `precor` routine we examined the images through 3×3 pixel boxes. The boxes which contain at least 9 pixels above 50 counts are considered astrophysical objects and remain. In the output images, the astrophysically real objects are maintained and other regions are set to zero. Separating cosmic rays and hot pixels from astronomical objects is essential at this point as they can produce false correlation peaks, which can lead to wrong cross correlation of the images. The cleaned images produced by `precor` are only used for measuring shifts, and will not process further in later reduction steps. For each image and a chosen reference image we constructed a cross-correlation image using the task `crossdriz` of the `dither` package in IRAF (Fruchter & Hook, 2002). The `crossdriz` produced cross-correlation images with a strong peak in the center of the image. In the last step the task `shiftfind` was used on the cross-correlated images to derive the shifts between science frames by comparing the location of the correlation peaks in the cross-correlation images.

The two separate bad pixel masks produced during the combination of dark frames into a masterdark and twilight flat frames into a masterflat were added to construct a final bad pixel mask. Using the created bad pixel mask, the 72 science frames were combined with the drizzle algorithm (Fruchter & Hook, 2002).

2.2.2 VLT/NACO data reduction

2.2.2.1 Darks and flat calibration frames

Dark calibration frames were extracted from the ESO archive facility for each exposure time taken during adjacent observation nights. Due to poor shielding of detectors in NACO, it is important that the dark frames are taken with the same camera and readout mode used for the observations (Marco et al., 2007). Master darks were created by average combining of the three individual dark frames to reduce the noise. Images were dark-subtracted with appropriate dark frames for each exposure time.

To obtain the pixel sensitivity, we used twilight flats which were taken on sky one hour before sunset. NACO flats with constant DIT of 7s and NDIT= 3 were taken for each field. We combined 9–13 twilight flat frames for each field. The fact that the pixel efficiency is robust over the time for NACO, allows us to use flat frames which are not taken at the same night as observation.

Prior to construct a master flat, a masterdark taken with the same DIT, camera and detector setting as the twilight flats was subtracted from each twilight frame. Twilight frames whose median flux exceed the linearity limit of the detector are discarded. To obtain the master flat, for each pixel a curve is plotted of the count value of the pixel against the median flux of all pixels on each flat frame. The resulting curve shows the pixel response from which a robust linear regression provides the pixel response

at different flux levels. The image showing all pixel gains is normalized to have an average value of 1. Images were dark-subtracted with appropriate dark frames for each exposure time and flat fielded using twilight flats.

2.2.2.2 Sky subtraction

At the end of each one hour observing block, ten sky frames were taken for individual fields with a subset of frames and exposures (i.e., DIT×NDIT) similar to the science frames. The sky frames were taken at off-cluster positions with relatively empty fields with the AO system in open-loop (i.e., without AO correction). Since it is not possible to find sky regions devoid of stars in the crowded area of the GC, the sky frames usually contained residual star flux. During the combination of the individual sky and science frames to construct a master sky, the residual star flux was cut out by discarding the bright pixels. The number of $n_{high} = number\,of\,sky\,frames - five\,brightest\,pixels$ were rejected. The sky frames were dark-subtracted and flat fielded similar to the science frames. The individual sky frames were combined using the IRAF task `imcombine` into a median average master sky. In the case of fields 2 and 5, the master sky frames were created using only sky frames, while we acquired the smoothest master sky frame for fields 3 and 4 by combining both science and sky frames.

2.2.2.3 Bad pixels and cosmic rays

During the combination of the master dark and flat-field images bad pixels were identified. The first bad pixel mask is created via an iterative 3 σ-clipping on each dark frame and deviating pixels are stored in a bad pixel mask. Hot pixels which are detected only once in the pile of three dark frames are assumed to originate from cosmic rays. For these pixels the final value of the masterdark is the mean of the remaining unaffected frames at the corresponding pixel.

A secondary bad pixel mask was created from the pixels whose sensitivity deviated significantly from the mean sensitivity of a masterflat image. In this process, bad pixels were revealed as pixels whose response after normalizing is less than 0.5 or more than 2. These bad pixels combined with hot and dead pixels detected during the combination of dark frames were written into a bad pixel mask.

In addition to the bad pixel masks made during creation of masterdark and masterflat images, individual bad pixel masks were created for each individual science frame. For this reason, we used the IRAF task `cosmicray` to reject individual pixels with fluxes eight times above the background standard deviation as cosmic rays. We added each cosmic-ray masks to the bad pixel mask to obtain individual masks for each science frame.

2.2.2.4 Coadding science frames

As in the case of the J-band SISCO images (see Sect. 2.2.1), we applied the task `precor` on all science image to prepare images for cross-correlations. Again, the task `crossdriz` was used on the cleaned NACO images to create a set of cross-correlation

frames. Then the shifts between images were determined using the cross-correlation frames, and images were combined with the drizzle algorithm (Fruchter & Hook, 2002) using a bad pixel mask created earlier. The corresponding shifts were used to align the individual science frames during the combination into a deep frame.

Before co-adding the reduced images we calculated the FWHM of a reference source in each field. The FWHM of a star is determined by a two-dimensional Gaussian fit to its flux. Combining images with low FWHM provides a higher resolution in the final image while adding a fewer number of images might cause a loss in sensitivity. To avoid degrading the spatial resolution in the combined images, we selected images with an FWHM of less than 0.0813"-0.1355" in dependence on the quality in each field. The numbers of combined images for each field are listed in Table 2.1.

In order to increase the spatial resolution of the combined image, reduced science frames were weighted by their quality criterion. Therefore, science frames were linearly weighted by the inverse of the FWHM of the brightest non saturated star in the field. We combined the weighted science images using the IRAF task `drizzle` (Fruchter & Hook, 2002). Drizzle applies each individual bad pixel mask to discard hot pixels and other image defects during image combination.

2.2.3 Photometry

The photometry was extracted using Starfinder, an IDL PSF-fitting package specifically developed to analyze AO data (Diolaiti et al., 2000). Starfinder's PSF-fitting algorithm extracts the empirical PSF from an image by a median combination of suitable stars. For this purpose we selected 10 to 15 reference stars in each field of VLT/NACO data, chosen to be relatively isolated, bright, and equally distributed across the field. However, since it is not easy to find such stars in crowded fields, secondary sources close to selected stars were first removed. A circular mask of 80 pixel diameter was used as the PSF size. The final PSF was extracted after two cleaning iterations. When deriving the flux of all stars in the image by fitting this PSF, starfinder performs a cross-correlation check to determine the similarity of potential stars with the PSF. For the source extraction we set the correlation threshold to ≥ 0.7 to accept sources as potential stars. Three iterations were performed to detect stars with a count level of 3σ above the average background in the image. The fluxes of all stars are derived by fitting the extracted PSF to each individual flux peak.

Starfinder assumes a constant PSF across the image, which is not exactly the case in wide-field AO imaging. The fact that the AO performance is highly dependent on the distance from the guide star (anisoplanatism) can lead to a spatial trend in the amplitude and shape of the photometric residual in the PSF subtracted frames. We used 10-15 stars in each field to extract the average PSF for PSF-fitting. To account for the variation in the residual flux, F_{res}, the ratio of the flux in the PSF-fitting residual to the stellar flux, $\frac{F_{res}}{F_{star}}$, was plotted against position. We detected a systematic linear trend with position, which could affect our photometry by 0.2 mag in fields 2, 3, and 5. The observed trend was fitted with a linear function, $\mathcal{C}_{\rm fit}(x)$, which is used to correct

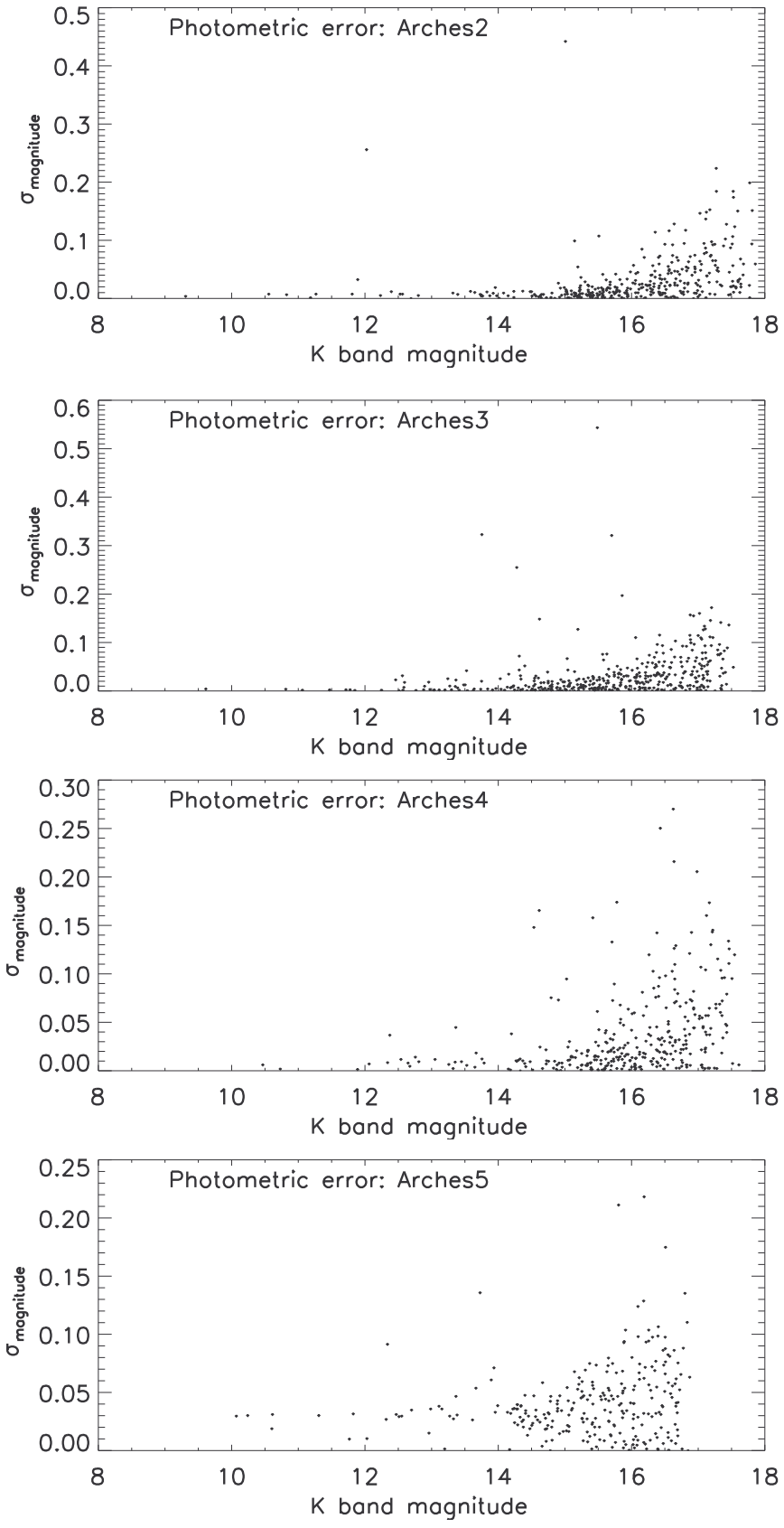

Figure 2.4: Standard deviations of the individual K_s-band magnitudes in the three auxiliary frames. As expected, the brighter sources have smaller photometric uncertainties. The value of $\sigma_{magnitude}$ for the majority of the sources is less than 0.1 mag.

the stellar fluxes, F_{star}:

$$F_{\mathrm{corr},star}(i) = F_{star}(i) + (\mathcal{C}_{\mathrm{fit}}(x) \times F_{star}(i)) \tag{2.2}$$

where x is the position of the ith star. This flux correction allows a uniform zeropoint correction to be applied across each field (see Sect. 2.2.5).

We performed the photometry on the reduced Subaru/CISCO frame similar to the VLT/Naco data using the Starfinder PSF-fitting package. For the wide CISCO field we extracted the PSF based on 15 reference stars, with the 9 secondary sources close to selected stars marked to be removed first. We set the PSF size by applying a 60 pixel circular mask.

2.2.4 Matching the data sets

To align and match the VLT/NACO and Subaru/CISCO data sets we transformed the CISCO coordinate system to coordinate system of NACO, which has lower pixel scale and is more precise. To obtain the transformation, about 25 identical reference stars with a high probability of being cluster members were identified by eye. The stars were chosen to be bright, non-saturated and uniformly distributed across the images. We used the `geomap` routine of IRAF to derive geometric transformations based on the x, y positions of the two lists. The best result is achieved when the transformations were derived using only the linear term, and the polynomial fit to the residuals was not used. The geometric linear transformation includes an x and y shift, an x and y scale factor, and a rotation. The root mean square (RMS) between the translated NACO coordinates and the positions of the corresponding stars in the Subaru/CISCO coordinate system is ~ 0.25 NACO pixel= 0.00675" which is enough to obtain unique individual matches between sources detected by NACO and CISCO. The computed transformations were applied on different fields using the IRAF task `geoxytran`. A similar procedure, using ~ 15 reference stars was applied to transform the coordinates of different VLT/NACO fields to each other, for the calibration purposes.

2.2.4.1 Photometric uncertainties

The photometric uncertainty of each star was derived from independent measurements of its photometry. We created three sublists of images for each frame stack. The images in the three lists were drizzled into three auxiliary frames for each field. Since we aim at a comparable photometric sensitivity for the three auxiliary frames, the number of combined images in the three lists are exactly equal and the worst one or two images are discarded in case the number of the images is not a multiple of three. It is also important that the quality of the three auxiliary frames is comparable to each other and also to the deep image. Therefore, images with similar performance should be distributed equally into the three lists. For the AO data, Strehl ratio of each star usually asses the performance of the AO system. The Strehl ratio is frequently defined as the ratio of the actual intensity of a point source compared to the intensity which would be reached by an ideal diffraction-limited telescope (Strehl, 1902). To derive the

Table 2.2: Calibration information

Field	Filter	Calib. Ref.	$N_{matched}$	Err.[a]	residual rms.[b]
		science frames			
wide field	J	Espinoza et al. 2009	36	0.011	0.066
1	H	Espinoza et al. 2009	117	0.007	0.078
1	Ks	Espinoza et al. 2009	125	0.005	0.056
2	Ks	Lucas et al. 2008 (UKIDSS/GPS)	4	0.049	0.024
3	Ks	calib3-5	111	0.017	0.184
4	Ks	calib4-5	59	0.011	0.086
5	Ks	calib3-5	98	0.012	0.120
		calibration frames			
calib3-5	Ks	Espinoza et al. 2009	86	0.097	0.010
calib4-5	Ks	calibrated F1	45	0.019	0.129

a) Zeropoint error = standard deviation $/\sqrt{N}$.

b) Residual rms = standard deviation of the sources used for zeropointing.

Strehl ratio, the peak flux of a two dimensional Gaussian fit of the normalized flux of the reference star or the brightest non-saturated source is measured. The Gaussian fit of the star is normalized to the total flux of the star within an aperture of 10 FWHM. The diffraction limited PSF for the specific properties of the VLT/NACO and its cameras, is theoretically calculated by the NACO pipeline team (Devillard, 2001). In our pipeline, the ratio of the normalized flux peak of the reference star is divided by the normalized diffraction limited PSF to calculate the Strehl ratio.

The subset lists of images are constructed so that they contained similar numbers of images from a full range of Strehl ratios. The selected frames in each list were combined to obtain an auxiliary image. We then applied the Starfinder source extraction with the same PSF fitting parameters as in the deep science image on each auxiliary frame. The resulting photometry provides three independent measurements for each star detected in all three images. We estimated the photometric error of each star by measuring the standard deviation of the independent magnitude measurements in the three auxiliary images. Some faint stars were only detected in two of the auxiliary frames. Moreover, few sources located at the boundaries of the images, which are not covered by every dithered frame, were not present in the three auxiliary frames. In these cases the photometric error is calculated as the deviation of the deep photometry from the mean of the two auxiliary measurements. Fig. 2.4 illustrates the resulting photometric lists uncertainties, $\sigma_{magnitude}$, for the stars which were detected in all three auxiliary frames. The value of $\sigma_{magnitude}$ for the majority of the sources is less than 0.1 mag.

2.2.5 Calibration

Since there are no red standard stars available, we use local standards in our fields for zeropoint calibration employing the NACO ground-based photometry of Espinoza, Selman & Melnick (2009). Espinoza, Selman & Melnick (2009) work in the natural photometric system of NACO in order to avoid large color terms from unreddened reference stars and use NACO standard stars observed in the same night for their absolute calibration.

We used their calibrated sources in the JHK_s photomotry list (their Table 3) located in the inner 0.4 pc from the cluster center for zeropointing. The wide J-band frame was calibrated based on 38 local standards in the central 0.4 pc of the Arches cluster. The H-band data only available in the central field (Fig. 2.2) was calibrated utilizing 117 stars in the central region (Field 1). The K_s calibration for the central field was performed by the direct comparison of 125 stars in Field 1 (table 2.2).

To calibrate the outer fields, we used two K_s calibration frames obtained during our visitor mode observations in June 2012. These two short exposure calibration fields (see Table 2.1) centered on the boundaries of our original fields allowed us to determine the zeropoints with respect to Espinoza, Selman & Melnick (2009) and our calibrated central field (see Fig. 2.2). Fields 3, 4, and 5 were thereafter independently calibrated with respect to the calibration fields based on 59-111 stars (see Table 2.2).

Since we were not able to obtain a calibration reference for Field 2, and this field also has no overlap region with the remaining data set, the zeropoint for Field 2 was determined using the UKIDSS database (Lawrence et al., 2007). This survey is re-sampled to a uniform spatial resolution of 1", which is improved by a factor of two compared to 2MASS. UKIDSS also probes three magnitudes deeper than 2MASS in the Galactic plane. We use the UKIDSS Galactic plane survey (GPS) which provides more accurate zeropointing, especially in crowded cluster fields (Lucas et al., 2008). The low resolution allowed for only four calibration stars, such that we consider the K_s-band calibration of Field 2 more uncertain than the zeropoints of the remaining fields.

2.3 Distortion

2.3.1 Introduction

Employing AO systems has improved the scientific potential for astrometry with ground-based telescopes by reducing the effect of wavefront distortions introduced by the Earth's atmosphere. However, the remaining part of the distortion caused by the atmosphere which is not corrected by AO (mostly the anisoplanatic effect), and also geometrical distortions from an infrared camera limit the precision of position measurements of stars. These limits not only affect the astrometry but the photometry as well, since they lead to a seeming variation in flux distribution of astronomical objects on the detector. Such variations of flux cause a variation in the PSF residuals and affect the photometry. Although in this thesis we perform no astrometric analysis of the data, as

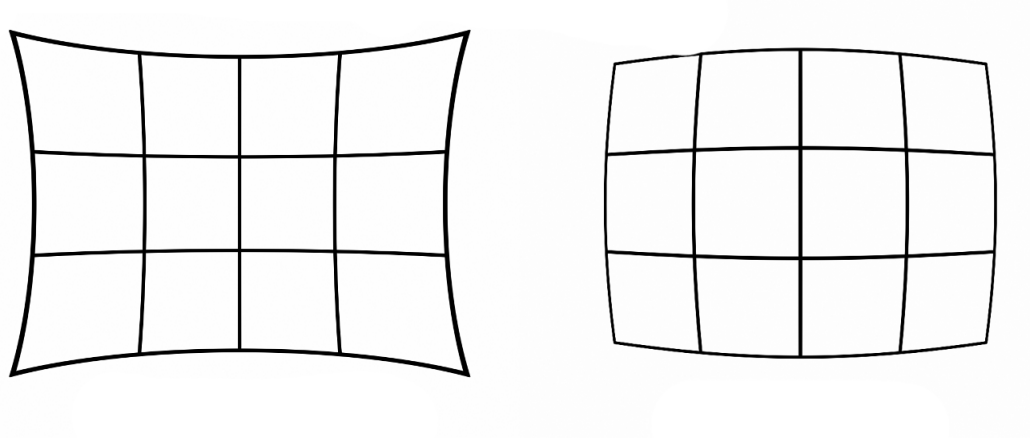

Figure 2.5: Two exaggerated forms of distortion. Left) The pincushion distortion which is produced if the image scale is larger at the edges of the field compared to its center. Right) The barrel distortion which is produced when the scale of the image decreases toward the edges.

part of our calibration effort as a team, where we also work on proper motion studies, we investigated the geometrical distortions of the NAOS/CONICA instrument. Understanding and modeling these geometrical distortions increases the precision of our position measurements. This helps us to diminish field contamination and obtain more precise relative astrometry in our proper motion membership studies.

The geometric distortions are produced by the telescope optics and camera. For example, misalignment of the optical instruments or imperfections of lenses and the detector contribute to the geometrical distortions. Such irregularities cause minor scale differences in the image across the field of view. In an exaggerated geometrically distorted image, if the scale is larger at the edges of the field compared to the center, the boundaries of the image turn out to bend inward (Fig. 2.5, left). If the scale of the image decreases close to the edges, the image boundaries appear to bend outward like a barrel (See Fig. 2.5, right).

2.3.2 Distortion measurements

One way to measure the geometrical distortion through the entire light path within the telescope, the AO system, and the camera is to observe a set of stellar positions on different parts of the detector. If there is no geometrical distortion, the absolute position of the star should be independent of its pixel position on the detector. In the case there are geometrical distortions, however, the remaining displacement of a star can be measured to quantify the distortion caused by the instrument. The main codes used for our on-sky measurements of the distortion are provided by Sebastian Egner [3].

Our data sets are taken with a range of shifts which allow us to subtract the sky background better and also help us to study the distortion. We performed the

[3]The codes are publicly available at: http://www.naoj.org/staff/egner/distortion/distortion.html

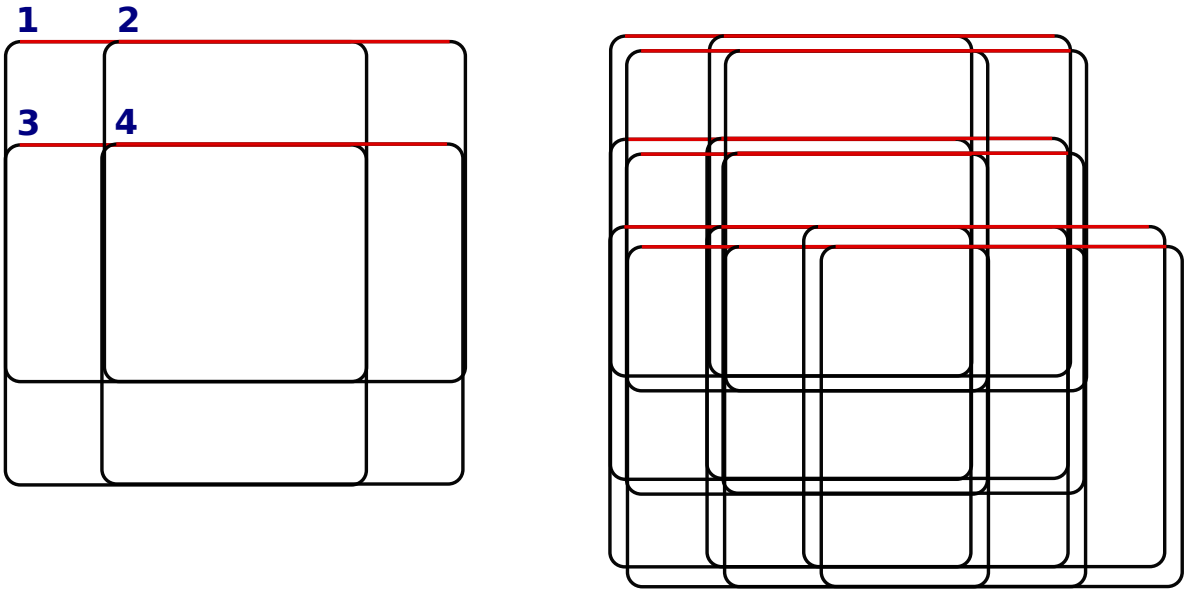

Figure 2.6: The red side of each box denotes the top of the NACO field of view. A set of four frames is used for measuring distortion for each pointing of the telescope(left). Series of such four images with illustrated shifts are taken (right), so that the average measured distortion is more robust.

geometrical distortion studies for two sets of the data taken from the Arches and Quintuplet cluster. However, since the shifts in the Arches data were too small and not distributed over the field for such studies, in this section we only show sample results from the observations of the Quintuplet cluster to explain the procedure and its main limitations.

Figure 2.6 illustrates the shifts which were used to observe the Quintuplet cluster. For the distortion calculation, we divide the shifts in two groups of dithers along the x-axis (for example $1 \rightarrow 2$ and $3 \rightarrow 4$ in Fig.2.6) and dithers along the y-axis ($1 \rightarrow 3$ and $2 \rightarrow 4$ in Fig. 2.6). Before measuring the distortion, we performed the photometry on individual images and measured the magnitude and position of all the stars in all the dithered images. We employed the shifts derived by the `shiftfind` routine during the calibration steps, to cross-match the extracted stars into a master list. The master list contains four pairs of (x,y) coordinates for each source (Fig. 2.6, left). The four pairs of coordinates which are taken from different sets of four images (Fig. 2.6, right) were all compiled to one master-list. For each pair of coordinates, the apparent displacement of the star on the detector is measured.

The shifts derived by the `shiftfind` routine are used only for cross-matching stars in different dithered frames. In order to measure geometrical distortions, first the commanded shift to the telescope according to the dither plan, was taken out from the measured displacements by subtracting the mean value of distortion of all the stars from each measured distortion value. The remaining displacement is interpreted as the geometrical distortion of the instrument. The displacement of each star, (x, y), relative

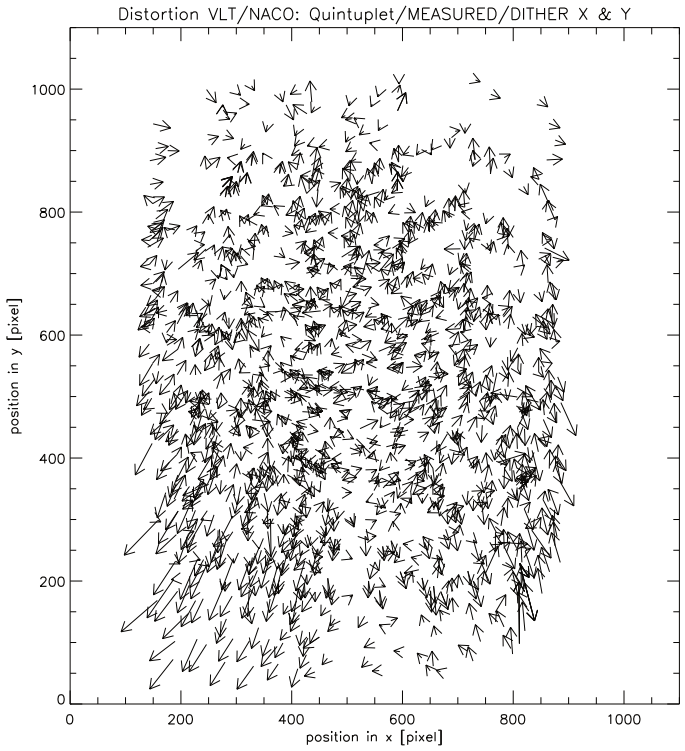

Figure 2.7: The average measured geometrical distortions in the VLT/NACO observations of the Quintuplet cluster by VLT/NACO. The average distortions are measured as relative displacement of stars compared to the their cross-matched counterparts in the dithered frames along both the x and y axis. The derived distortion value for each star is referred to a middle position of the four dithered coordinates of the star. Measured distortions follow flow patterns especially in the lower left corner. The measured distortions are exaggerated by a factor of 20000 for illustration.

to its cross-matched counterpart, (x', y'), is measured, $\delta x = x - x'$, $\delta y = y - y'$, to determine the geometrical displacement at a position on the detector which is located in the middle of the location of the two stars, $X = \frac{x+x'}{2}$, $Y = \frac{y+y'}{2}$. Figure 2.7 shows the average measured distortion for all the dithers (see Fig. 2.6) shown for the detected stars. In various segments of Fig. 2.7, specially in lower left corner, a flow structure in the measured displacements is present. Such prominent deviations from random orientations are only expected if systematic distortions are present.

The geometric distortions caused by the infrared camera are expected to be static. However, the anisoplanatic effect and the distortion introduced by the AO system change with time and therefore are different for each data set. If the measured distortions illustrated in Fig. 2.7 are stable they can be modeled. The goal is to derive a single set of distortion corrections that can be applied to all the images to minimize the systematic non-linear residuals after coordinate transformation, i.e the geometrical distortion. The geometric distortion models can generally characterize the measured distortion $(dist_x, dist_y)$ as a function of the pixel position on the detector (x, y), usually

as a polynomial correction function. We modeled the geometrical distortion with a 3rd order 2-d polynomial with cross terms which are of the order of three for both x and y[4] (see equation 2.3).

$$\begin{aligned} dist_x &= a_{00} + a_{10}x + a_{01}y + a_{20}x^2 + a_{02}y^2 + a_{11}xy + a_{21}x^2y + a_{12}xy^2 \\ &+ a_{22}x^2y^2 + a_{30}x^3 + a_{03}y^3 + a_{31}x^3y + a_{32}x^3y^2 + a_{13}xy^3 + a_{23}x^2y^3. \\ dist_y &= b_{00} + b_{10}x + b_{01}y + b_{20}x^2 + b_{02}y^2 + b_{11}xy + b_{21}x^2y + b_{12}xy^2 \\ &+ b_{22}x^2y^2 + b_{30}x^3 + b_{03}y^3 + b_{31}x^3y + b_{32}x^3y^2 + b_{13}xy^3 + b_{23}x^2y^3. \end{aligned} \quad (2.3)$$

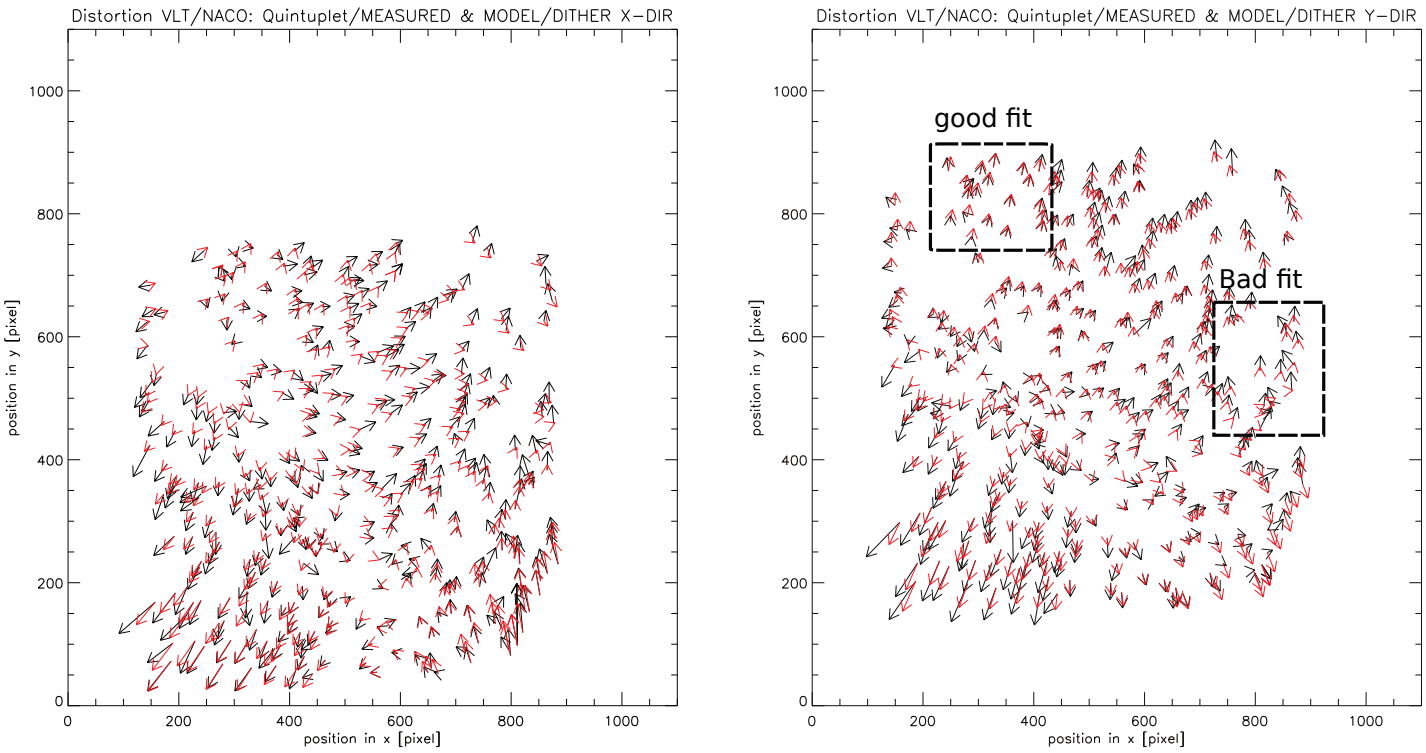

Figure 2.8: The average measured distortions present in the observations of the Quintuplet cluster by VLT/NACO for dithers along the x-axis (left) and y-axis (right). The measured distortion values, which are shown as black arrows, are fitted with a two-variable (x,y) polynomial of the order of 5. The modeled distortion value for each star is illustrated by a red arrow. The modeled arrows mostly match the observed distortions, however in some regions it deviates significantly. Two example regions with good and bad model fits are shown in the right figure. The measured and fitted distortions are exaggerated by a factor of 20000 for illustration.

[4]We repeated the whole experiment using the IRAF `geomap` routine to derive the distortions by choosing a 3rd order 2-d function with cross terms which are of the order of one for both x and y. However, the fitted distortions derived with our self-developed IDL codes appeared to match better with the measured values.

2.3.3 The modeled distortion map and inconsistencies

Figure 2.8 shows the average measured distortions for individual stars together with their fitted distortion, separately for dithers along the x and y axis. Measured distortions, shown in Fig. 2.8, do not present a smooth profile. Since the expected geometrical distortions are not caused only by a single lens, but by a series of optical instruments and the detector, we do not expect the final distortion map to look like a perfect pincushion or barrel. However, we expect a more homogeneous flow pattern which varies more regularly with position compared to what we observe. If the distortion is a result of a tilt of the camera plate or misalignment of the optical instruments, we expect the geometrical distortions to be small over the inner portions of the field of view and grow near the edges of the detector. Fig. 2.8 illustrates an increasing distortion toward the lower edge of the detector. However, the heterogeneity of the measured distortions do not match the expectation from pure geometrical distortions.

Although the modeled distortions mostly match the measured values, in some parts the fitted polynomial models deviate from the observations. In the Fig. 2.8 (right) two sample regions with good and bad modeled distortion fits are shown. The sample box with a deviating model fit illustrates the case that the modeled distortion has a different orientation as compared to the measured arrows. In some other regions, for example the lower left corner in Fig. 2.8 (right), the orientations match, however, the magnitudes of the measured and modeled distortions are not consistent.

Another important inconsistency is that the measured and therefore the modeled distortions which are calculated from dithers along the x and y axis are not completely similar. The measured distortions from different data sets, i.e. the Arches and Quintuplet clusters observations, were even more inconsistent. The geometrical distortion is an internal feature of the telescope and the instruments, therefore, it should be only a function of position on the detector and be independent of time or the shift directions. Deriving inconsistent distortion solutions implies that the geometrical distortion measurements are affected by the strong anisoplanatic effects in our observations. Due to mentioned inconsistencies we did not consider the obtained modeled distortion as a self-consistent distortion map to apply to all data sets. The variable nature of the anisoplanatic effect makes it hard to distinguish the uncorrected atmospheric distortion from the geometrical distortion of the instrument.

Chapter 3

The Arches cluster: dynamical mass segregation and the effect of the extinction law on the stellar mass function.

This chapter, excluding sections 3.2.2 and 3.2.3, is published in Astronomy & Astrophysics: "The Arches cluster out to its tidal radius: dynamical mass segregation and the effect of the extinction law on the stellar mass function.", Habibi, M., Stolte, A., Brandner, W., Hußmann, B., & Motohara, K. 2013, A&A, 556, A26.

Contents

3.1 Introduction

The center of our galaxy hosts many massive molecular clouds, active sites of massive star formation, and a remarkable number of high-mass stars (Yusef-Zadeh et al. 2009). It contains three of the most massive and young star clusters in our Galaxy, namely: the Arches, Quintuplet and the young nuclear cluster. The Arches cluster, located at a projected distance of ~ 26 pc from the Galactic center (GC), is the youngest among the three (~ 2.5 Myr, Najarro et al. 2004; Martins et al. 2008b). This cluster contains many massive stars including 160 O-stars and 13 WN stars (Figer 2004 ; Martins et al.

2008b). With its collection of high-mass stars and its very dense core ($\rho_{core} \sim 10^5$ $M_\odot/\mathrm{pc}^3$; Espinoza, Selman & Melnick 2009), the Arches cluster is an excellent site for addressing questions about massive star formation, the stellar mass function, and the dynamical evolution of young, massive clusters in the GC environment.

The high extinction toward this cluster nevertheless causes this investigation to be challenging. Previous studies of the Arches cluster were aware of the high extinction toward this cluster but have chosen different methods of addressing this problem. It is therefore not surprising that different studies resulted in deviating mass functions in the center of the Arches cluster. Figer et al. (1999) adopted a single extinction value of $A_K = 3.0$ mag and found a flat mass function for the Arches cluster compared to the standard Salpeter (1955) initial mass function. This finding opened a series of debates and further studies with the aim of distinguishing between primordial or dynamical mass segregation. Stolte et al. (2002) and Stolte et al. (2005) utilized deep adaptive optics (AO) observations to derive the present-day mass function (PDMF) within the cluster's half-mass radius. They treated the variable extinction of the cluster by correcting for a radial reddening gradient based on the extinction law of Rieke & Lebofsky (1985). A study by Kim et al. (2006) applied the extinction law of Rieke, Rieke & Paul (1989) and chose to correct for a single, mean extinction value for each of the observed cluster annuli and each control field. These studies confirmed the flattening of the mass function in the center of the cluster and also achieved to study the less massive sources in the cluster. Finally, Espinoza, Selman & Melnick (2009) used the general Galactic extinction law by Fitzpatrick (2004) to derive the mass function. They acquired extinction parameters for the VLT/NACO natural photometric system and corrected the individual extinction toward each star. As discussed in Sect. 3.3, these studies result in central slopes of $-1.26 < \alpha < -1.88$, and could not come to a common conclusion in regard to the central Arches mass function.

In this chapter, we study the effects of the new regime of steeper near-infrared extinction laws on the derivation of individual stellar parameters toward the Arches cluster. The K_s and H-band AO images taken with VLT/NACO as well as J-band images obtained with Subaru/CISCO are analyzed to cover the outskirts of the Arches cluster for the first time. in Sect. 2.1, we describe the data and observational setting. The data reduction steps, photometry, and calibration processes are explained in Sect. 2.2. This Chapter is organized as follows: We determine the individual extinction values and construct the extinction map of the cluster in Sect. 3.2. In the last section of Sect. 3.2, the individual stellar parameters derived assuming the two regimes of extinction laws are compared. We investigate the effect of the assumed slope of the extinction law on the determination of the mass of the most massive star in the Arches cluster, which had been used in previous studies to establish an upper mass limit for the star formation process in the Milky Way. In Sect. 3.3, the PDMF of the Arches cluster [1] is constructed for an area that reaches closer to the tidal radius of the cluster

[1] Some of the previous studies have used the initial masses corresponding to the observed stellar luminosities to construct a presumably initial mass function. The rapid dynamical evolution of massive star clusters such as the Arches (e.g., Kim et al. 2006, Harfst, Portegies Zwart & Stolte 2010) implies that the observed stellar mass function can be influenced by stellar evolution, as well as by the

for the first time. We probe the radial variation in the slope of the mass function in order to distinguish between primordial or dynamical mass segregation in the Arches cluster. A summary of our findings is presented in Sect. 4.5.

3.2 Extinction derivation

The extinction of each star can be derived by individual dereddening in the color-magnitude plane. In this section, a sample of cluster members is selected from the color-magnitude diagram (CMD) of each field to determine the individual extinction for each cluster star candidate.

The CMD for the central field is shown in Fig. 3.1. A population of blue foreground sources with lower extinction and mostly associated with the spiral arms, as well as intrinsically red objects such as red giants or red clump stars, can be distinguished in Fig. 3.1. We applied a color selection (Fig. 3.1) in order to reject contaminating sources and obtain a representative sample of cluster members. The color selection is based on the prominent main sequence cluster members in the CMD of the central part of the Arches cluster. The bright part of the observed sequence in the central field, $11 < K_s < 15$ mag, has a mean color of $A_H - A_{K_s} \sim H - K_s = 1.87$ mag (Fig. 3.1), where we have assumed the intrinsic $H - K_s$ color of young, high-mass main sequence stars to be close to zero ($-0.03 < H - K_s < -0.04$, Lejeune & Schaerer 2001). This color can be converted to an approximate color of $J - K_s \sim 5.1$ mag (using Rieke & Lebofsky 1985). Brighter sources with $K_s < 11$ are likely to belong to the known WR population in the Arches cluster. Using the expected main sequence color of cluster stars from Field 1 to identify the cluster main sequence in each outer field, we determine appropriate color selections for likely cluster members (Fig. 3.2). The mean extinction in each outer field varies slightly with respect to Field 1. In Fig. 3.2, we show the expected $J - K_s$ main sequence color derived from the mean $H - K_s$ color in Field 1. The higher extinction in Field 2, which has the largest radial distance from the cluster center, is particularly pronounced. An increase in extinction with increasing radius is consistent with the previously detected radial extinction variation (Stolte et al. 2002; Espinoza, Selman & Melnick 2009).

The age of the Arches cluster is estimated to be 2.5 Myr (Blum et al. 2001; Najarro et al. 2004; Martins et al. 2008b, for a detailed discussion of the previous studies on the age and the metallicity of the cluster see Sect. 3.3.2). We adopted a Geneva isochrone (Lejeune & Schaerer 2001) with solar metallicity located at the GC distance of 8 kpc (Ghez et al. 2008).

To derive the individual extinction values we use two extinction laws (EL): Rieke & Lebofsky (1985) and Nishiyama et al. (2009). As mentioned in the introduction, the extinction law derived toward the GC by Rieke & Lebofsky (1985) ($A_\lambda \propto \lambda^{-1.61}$ which

dynamical evolution of the cluster, so it does not represent the initial mass function even at the current young cluster age. All the mass functions in this study are constructed based on the current spatial distribution of the derived present-day masses derived from stellar evolution models. For the sake of comparison with other studies, we have included the mass function slopes constructed from the initial individual masses, i.e. only corrected for stellar evolution, in Table 3.2.

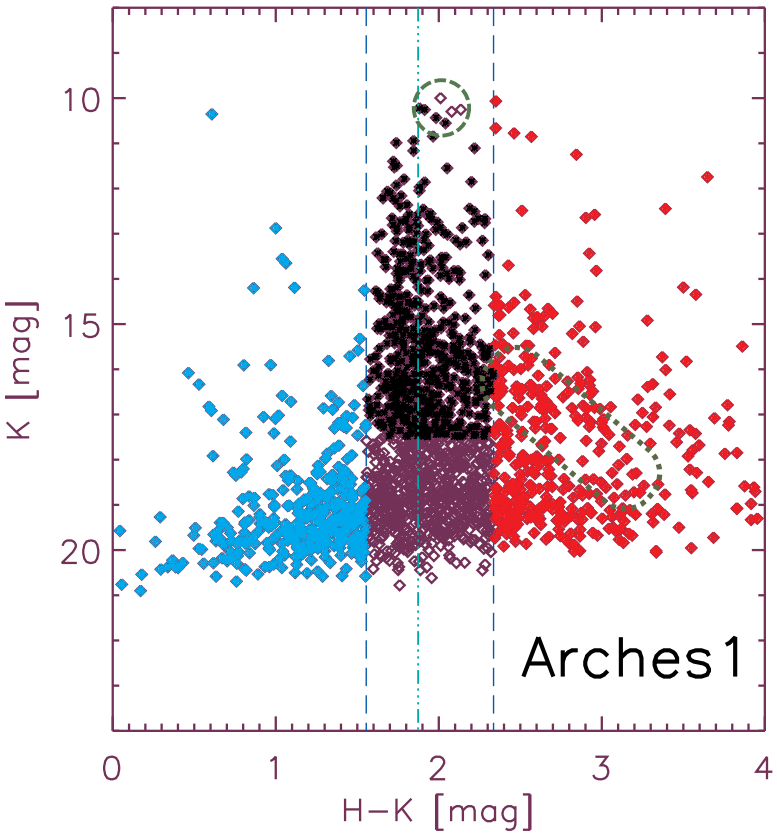

Figure 3.1: Color-magnitude diagram of the center of the Arches cluster. Vertical dashed lines show the color selection used to discard contaminating background and foreground sources. Less extincted foreground sources, mostly associated with the spiral arms, are shown by blue diamonds, whereas intrinsically red objects, such as red giants or red clump stars are marked in red. The location of red clump stars is indicated with an enclosed dotted line. The black diamonds represent likely cluster members. The mean H-K_s color of the bright cluster members, $11 < K_s < 15$ mag, in the center of the Arches cluster is shown by a green dot-dashed line. Brighter sources, $K_s < 11$ mag, belong to the known WR population in the Arches cluster (denoted by the enclosed dashed circle).

implies $\frac{A_J}{A_K} = 2.51$, $\frac{A_H}{A_K} = 1.56$) has been used in most stellar population studies in the GC until recently. Nishiyama et al. (2009) derived the extinction law again toward the GC and obtained a power law of steeper decrease with wavelength ($A_\lambda \propto \lambda^{-2.0}$ which implies $\frac{A_J}{A_{K_s}} = 3.02$, $\frac{A_H}{A_{K_s}} = 1.73$), which is also consistent with the recent determination of the near-infrared extinction law by Schödel et al. (2010) and Stead & Hoare (2009) along the GC line of sight.

Using two ELs translates into two extinction path slopes in the CMD (Fig. 3.3). We slide back the cluster members along each extinction path toward the nonextincted theoretical isochrone. The brightness, color and mass of a star at the intersection point of the unreddened isochrone with the extinction vector are assumed to be the intrinsic

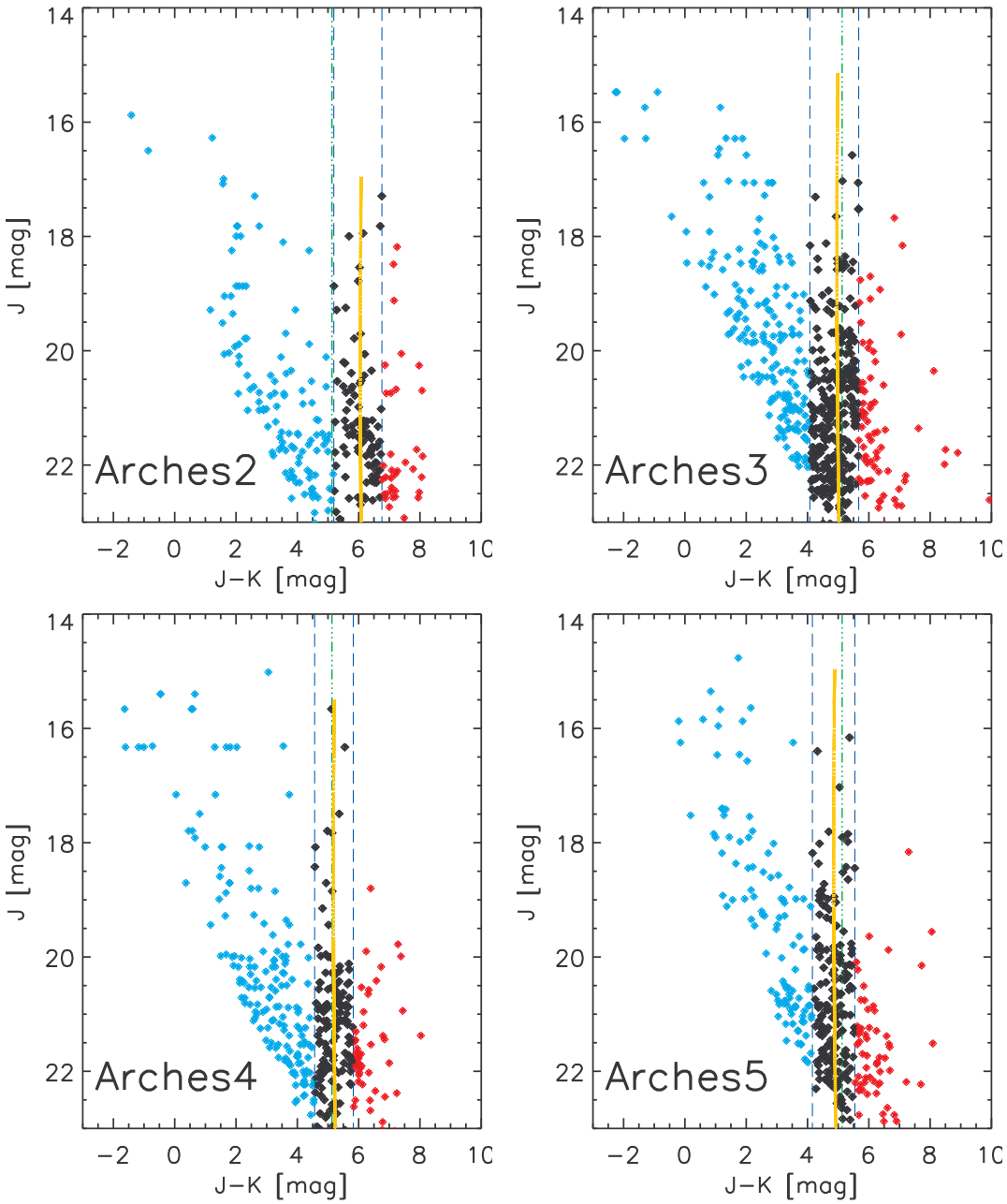

Figure 3.2: Color-magnitude diagrams of the outskirts of the Arches cluster. Blue dashed lines show the color selection used to choose the cluster members and discard background (blue diamonds) and foreground (red diamonds) sources. The Geneva isochrone with the mean extinction value of the cluster members in each field is shown in yellow. The green dot-dashed line represents the approximate mean color of the cluster members in the center of the cluster where the mean extinction is slightly lower.

brightness, color, and mass of this star (Fig. 3.3). Three of the brightest sources in Field 1 are formally located above the maximum initial isochrone mass of $120 M_{\odot}$ after dereddening. These sources are discarded since we are not able to derive their intrinsic properties. In this work we do not consider binarity or rotation of the detected sources, which can also partly contribute to the observed color of each star.

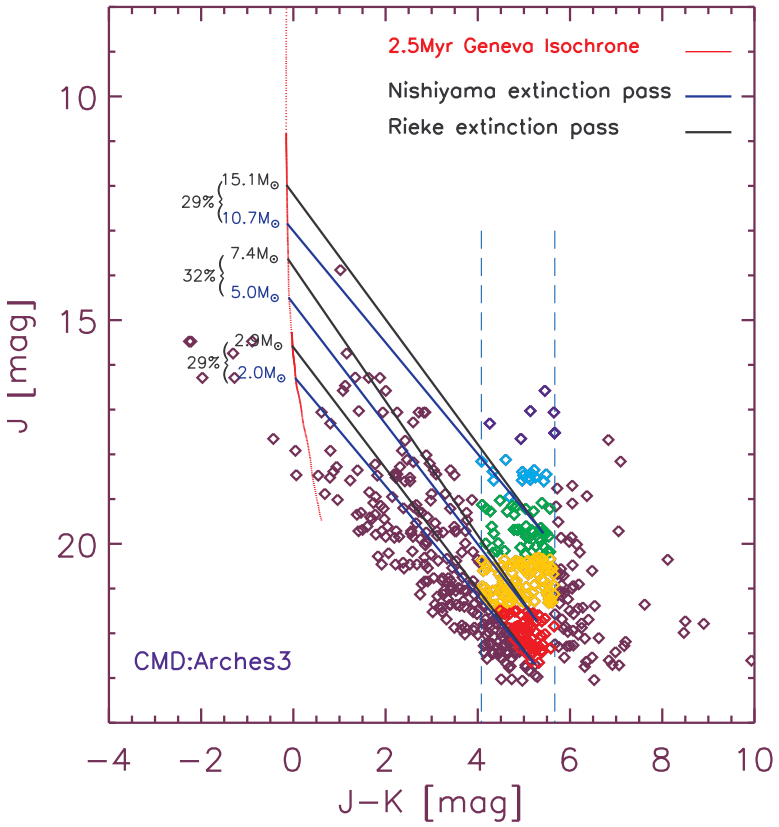

Figure 3.3: The color-magnitude diagram of Field 3 in the outskirts of the Arches cluster. Cluster members are selected between the two dashed lines and are color coded according to their J-band magnitude. A Geneva isochrone of solar metallicity with an age of 2.5 Myr is also shown. Black lines represent the extinction path assuming the Rieke & Lebofsky (1985) extinction law, while blue lines are extinction paths based on the Nishiyama et al. (2009) extinction law. The difference in derived masses using the two laws are written for sample sources close to the isochrone in percentage.

3.2.1 Comparison of the parameters derived from the two extinction laws

Extinction causes stars to be reddened with respect to their intrinsic color. Assuming different extinction laws will change the derived extinction and consequently the intrinsic properties of the stars. Figure 3.4 (up) strikingly illustrates the K_s-band extinction difference, ΔA_{K_s}, for each star in Field 3 using the Rieke & Lebofsky (1985)

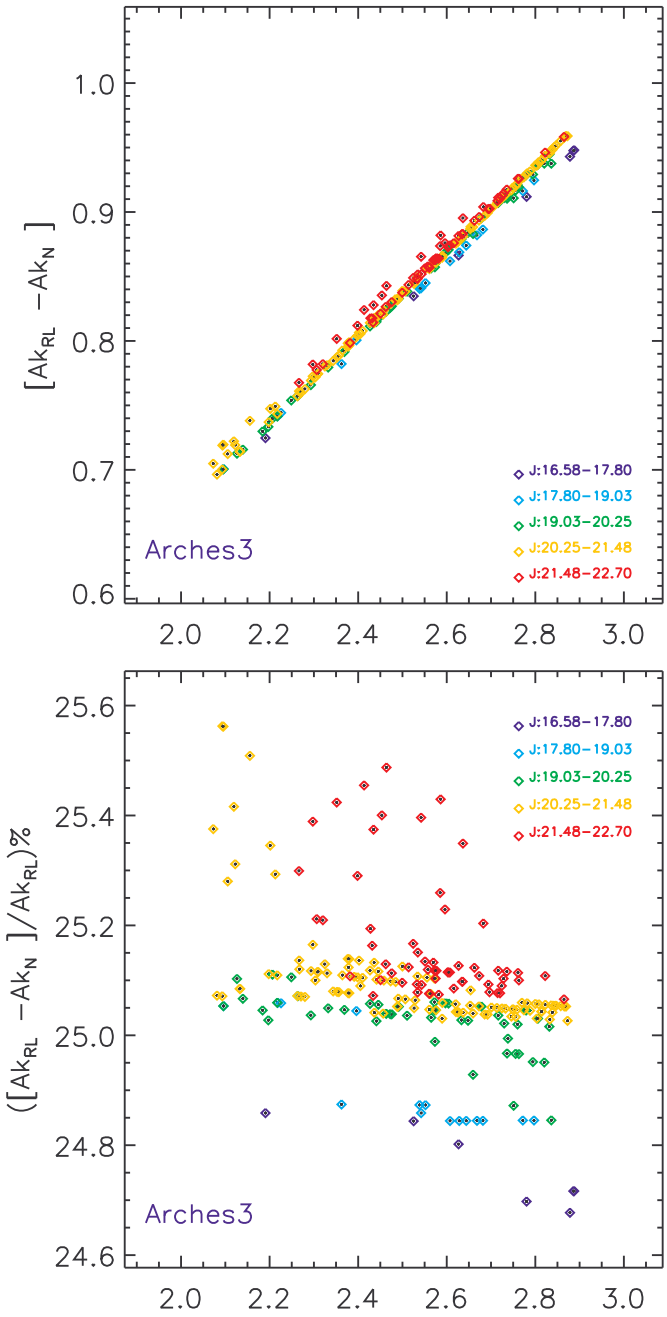

Figure 3.4: *Up:* The extinction difference in Field 3 (outskirts of the cluster) derived using the Nishiyama et al. (2009) and the Rieke & Lebofsky (1985) extinction laws is shown as a function of the K_s-band extinction derived assuming the Nishiyama et al. extinction law. The difference depends linearly on the extinction and increases with increasing extinction. *Down:* The extinction difference in percentage. The average A_{K_s} difference is $\sim 25\%$ in Field 3 and $\sim 24\%$ across the whole cluster.

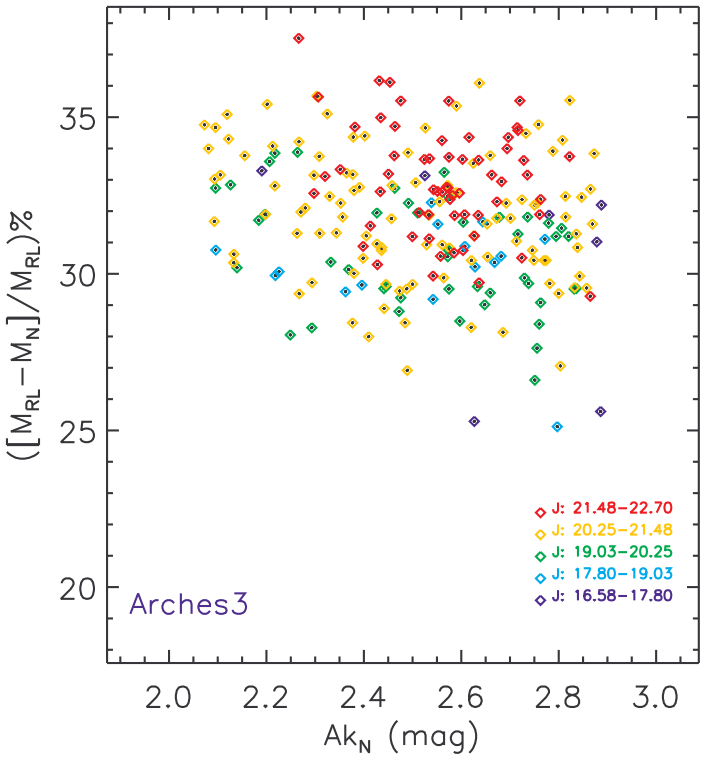

Figure 3.5: The derived mass difference assuming the Nishiyama et al. (2009) and Rieke & Lebofsky (1985) extinction laws is shown as a function of A_{K_s} for each source in Field 3. Derived masses using the Rieke & Lebofsky (1985) extinction law are on average 30% higher than derived masses when using the Nishiyama et al. extinction law.

EL (RL-EL) and the Nishiyama et al. (2009) EL (N-EL). The A_{K_s} difference across the whole cluster is more than 0.6 mag, and it can reach up to 1.1 mag which is equivalent to roughly ten magnitudes of visual extinction. The difference increases linearly with increasing extinction and is highest for the sources with the highest A_{Ks} values. The average A_{K_s} difference in the cluster is $\sim 24\%$. The A_{K_s} difference in percentage (down) and absolute value (up) for Field 3 is shown in Figure 3.4. In Field 3, most of the sources have an A_{K_s} difference of $\sim 25\%$ while some fainter sources appear in a small upward spread in this plot. The less certain photometry of fainter sources, together with a small curvature at the low-mass end of the isochrone, causes this spread: since the length of the connecting path from a star to the isochrone is the measure of the stars' extinction, slightly different slopes of the connecting path result in a bigger difference in the length of the line in areas where the ischrone has a small bend.

Figure 3.5 sows the difference in the derived initial mass for each star using the two different ELs for Field 3. Derived masses using the RL-EL are $\sim 30\%$ higher than derived masses assuming the N-EL for the full sample of Arches cluster members.

While the most massive initial mass in our sample is $104 M_{\odot}$ when dereddening with an RL-EL, the highest initial mass is only $80 M_{\odot}$ when the N-EL is used. In Fig. 3.5, the less certain photometry of faint sources and a small bend in the faint end of the isochrone act against the more rapid increase in masses at the bright end of the isochrone. Therefore in Fig. 3.5 there is a vertical spread of a few percent among both faint and bright sources. In their study, Kim et al. (2006) briefly report that the 50% completeness limit of $1.3 M_{\odot}$ derived from the Rieke, Rieke & Paul (1989) extinction law decreases to $1 M_{\odot}$ when applying Nishiyama et al. (2006) instead. This comment is consistent with our finding that the individual stellar mass decreases by $\sim 30\%$ when the Nishiyama extinction law is employed.

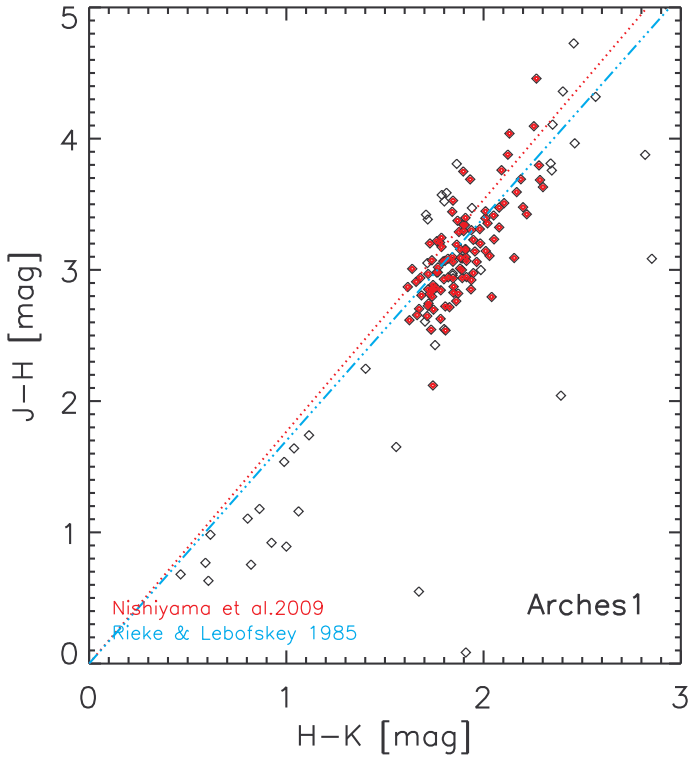

Figure 3.6: Color-color digram for the central field (Field 1), using the Subaru J-band magnitudes, together with VLT/NACO high-resolution H and K_s magnitudes, to test whether conclusions on the best-fitting extinction law can be drawn from these data sets.

Figure 3.6 illustrates the color-color digram (CCD) for the central field (Field 1). Our J-band data for the central region, the only field where we have additional VLT/NACO H-band observations, is not employed to derive stellar properties since seeing-limited J-band data will perform less efficiently in the crowded central region. Nevertheless, we used the Subaru J-band magnitudes to test whether any conclusions on the best-fitting extinction law can be drawn from these data sets. The present spread in Fig. 3.6 shows that both extinction law slopes are consistent with our data

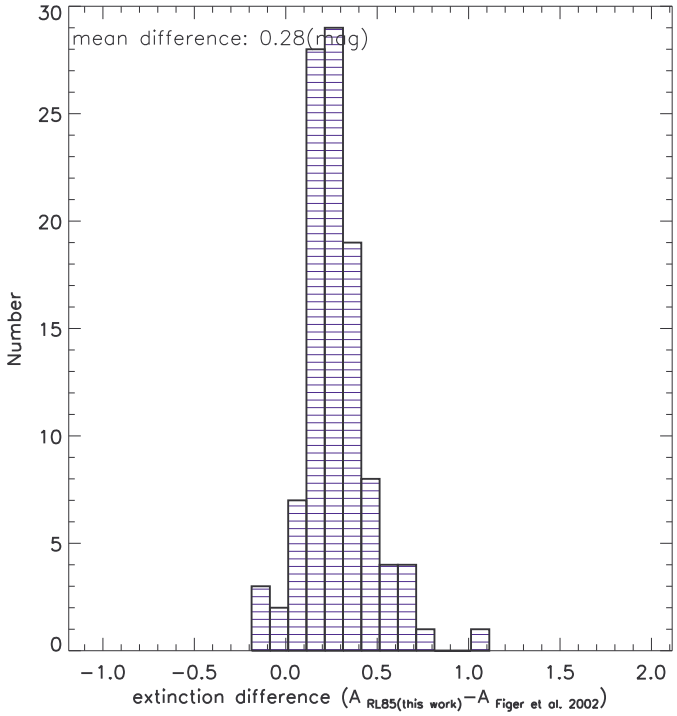

Figure 3.7: The comparison between the individual extinction values of this study using RL-EL and Figer et al. (2002) individual extinction values computed as $A_k = 1.95 \times E(H-K)$.

within the photometric uncertainties. We repeated the same experiment with the data from (Espinoza, Selman & Melnick, 2009) since their work benefits from the J-band AO images acquired by the VLT/NACO AO system on the VLT. However, scatter in their data also does not allow us to distinguish between the two extinction paths.

3.2.2 Comparison with other data sets

In this section we compare the individual extinction values and photometries derived in this work with two other studies on the extinction and mass function of the Arches cluster. Figer et al. (2002) utilized HST/NICMOS narrowband and broadband imaging to extract photometry of the Arches cluster. Fig. 3.7 shows the comparison between our individual extinction values using RL-EL and individual extinction values computed with the suggested equation by Figer et al. (2002):

$$A_k = 1.95 \times E(H-K),^{2} \tag{3.1}$$

Figer et al. (2002) made a simplifying assumption that main sequence colors can be assumed for the cluster members, with $H-K = -0.05$ mag, and $m_{F160W} -$

[2] see Figer et al. (2002). their Table 3, footnote d.

$m_{F205W} = H - K$, where m_{F160W} and m_{F250W} are the measured magnitudes using the HST/NICMOS broadband filters at 1.10 and 2.05 μm, respectively. Accordingly, they could assume

$$E(H-K) = m_{F160W} - m_{F205W} + 0.05mag \tag{3.2}$$

Therefore, individual extinction values are computed as in equation 3.1. This equation is equivalent to the assumption of an extinction law with $\frac{A_k}{(A_H - A_K)} = 1.95$, while for the Rieke & Lebofsky (1985) extinction law, this coefficient is $\frac{A_k}{(A_H - A_K)} = 1.78$. This discrepancy causes $\Delta A_k = 0.17 \times E(H-K)$ which for the mean color $E(H-K) = 1.87$ is equal to $\Delta A_k = 0.31$ mag. Considering such a different assumption on the extinction

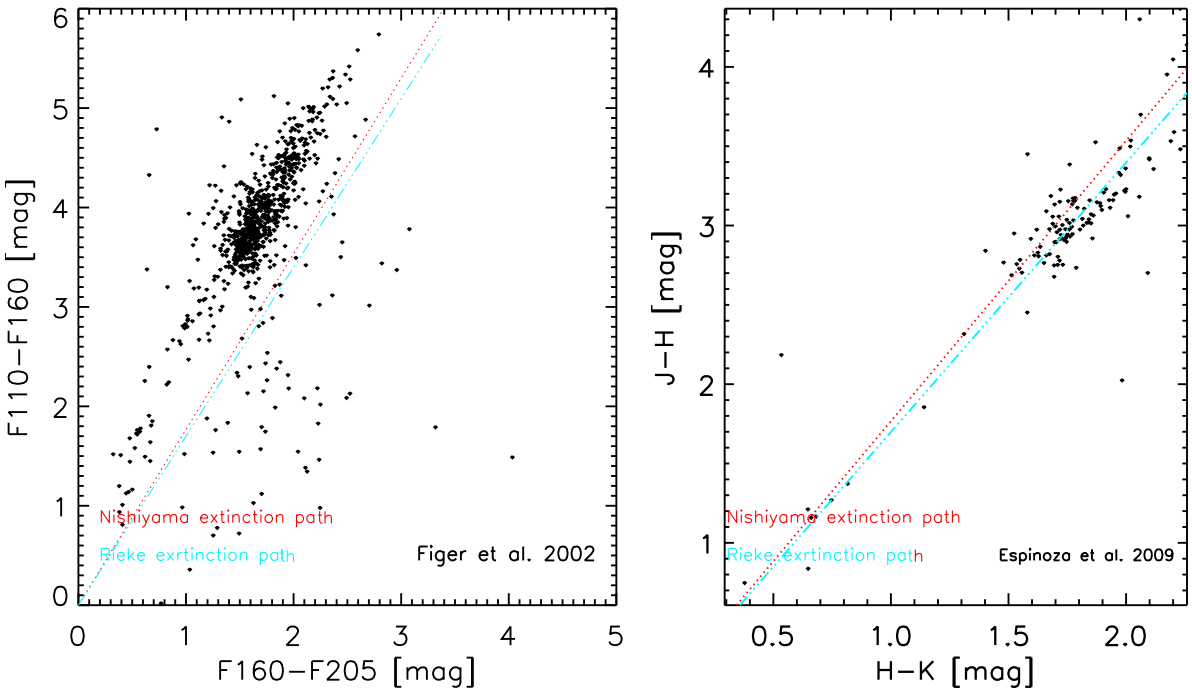

Figure 3.8: *Left:* Color-color diagram of the central field of the Arches cluster observed by Figer et al. (2002). The shift from the extinction paths suggests that there is a calibration zeropoint offset left in their data. Nevertheless, the spread in the distribution of the sources in the direction perpendicular to the extinction paths illustrates that it is not possible to find the best extinction law based on their photometry. *Right:* Color-color diagram of the central field of the Arches cluster ($r < 0.4$ pc) studied by Espinoza, Selman & Melnick (2009). The spread of the sources in the direction perpendicular to the extinction paths prevents choosing the best extinction law.

law and the fact that the filter systems of HST/NICMOS and VLT/NACO are substantially different, the mean difference of 0.28 mag shown in Fig. 3.7 is very consistent with these expectations. Kim, Figer & Lee (2006) also suggest in their Fig. 12 that a discrepancy of 0.2 mag for extinctions of $2 < A_{Ks} < 3$ can be expected due to the non-linear nature of the HST/NICMOS filters as compared to the ground-based filter system.

As shown in Fig. 3.6, the present spread in the CCD constructed based on our photometry is consistent with both extinction law slopes within the photometric uncertainties. To test whether we can draw any conclusion about the best-fitting extinction law from other data sets, we construct the CCDs using the HST/NICMOS photometry from Figer et al. (2002) as well as the VLT/NACO photometry analyzed by Espinoza, Selman & Melnick (2009). The resulting CCDs are illustrated in Fig. 3.8. The HST/NICMOS data taken from Figer et al. (2002) display an unexplained offset in the two-color plane (Fig. 3.8, left). Irrespective of this apparent calibration problem, the scatter in the HST/NICMOS data does not allow us to distinguish between the two extinction vectors. A similar spread is present in the illustrated CCD based on the photometry by Espinoza, Selman & Melnick (2009) (Fig. 3.8, right). Therefore, none of the available observations of the Arches cluster allows for a final conclusion on the best-fitting extinction law toward the Arches line of sight.

3.2.3 The color-based cluster membership check

Different intrinsic colors of early-type and late-type stars cause them to lie along different sequences in the CCD when extincted by an arbitrary amount. Comerón & Pasquali (2005) suggest a reddening-free quantity to separate early-type stars from background red giants:

$$Q = (J - H) - E_{j-h}/E_{h-k} \times (H - K), \tag{3.3}$$

Early-type stars should have $Q \sim 0$, whereas red giants are expected to be characterized by $Q \sim 0.5$. We use the reddening-free parameter, Q, to check if the applied color selection in our study has discarded the giant branch contamination. The full cluster-member check based on the Q parameter requires observations in three filters ($J, H,$ and$K$) for all the fields. As described in Sect. 2.1, H-band observations with VLT/NACO are only available for the central field of the Arches cluster (field 1). In Fig. 3.9, non-member sources, with $Q > 0.5$, are marked on the constructed CCD of field 1. The selected cluster sample of this study within field 1, contains one source with $Q_{Nishi} > 0.5$ (shown as a blue diamond) while there is no source with $Q_{Rieke} > 0.5$. We conclude that, therefore, the applied color-selection in field 1 does not suffer from significant giant contamination.

In principle, we could compare different samples of cluster members derived using different extinction laws to the corresponding value of Q_{Rieke}/ Q_{Nishi} to test the extinction law assumption. However, as Fig. 3.9 illustrates using the Q_{Rieke} or Q_{Nishi} parameter does not result in a considerably different cluster sample.

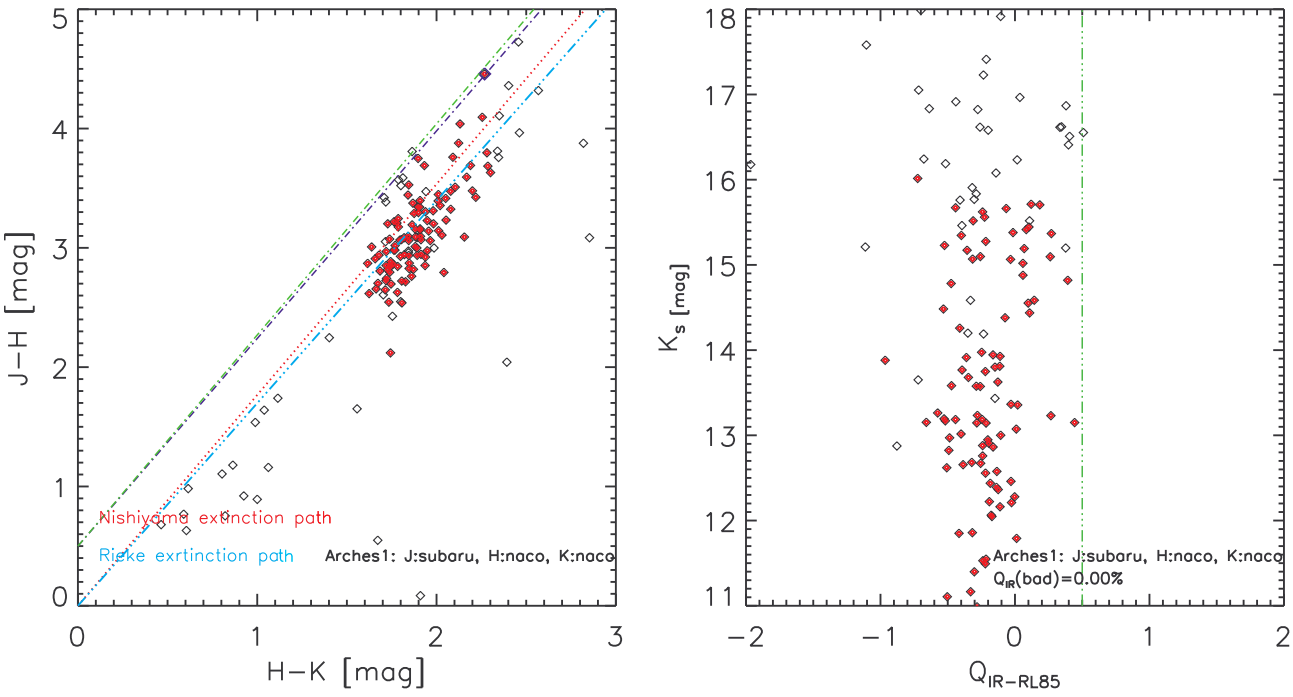

Figure 3.9: *Left:* Color-color diagram for the central field of the Arches cluster, field 1, using H and Ks-band observations acquired with VLT/NACO matched with crowding limited J-band obtained with Subaru/CISCO. Filled red diamonds represent the color-based cluster member selection. The source marked with a blue diamond at $H-K = 2.3$ mag and $J-H = 4.5$ mag has $Q_{Nishi} > 0.5$ while there is no source with $Q_{Rieke} > 0.5$. *Right:* The K_s band magnitude is plotted over Q assuming the Rieke & Lebofsky (1985) extinction law. The green dashed line represents the expected Q for red giants.

To construct CCDs and check their giant contaminations in the outer fields, where H-band observations with VLT/NACO are not available, we used the H-band data obtained with HST/WFC3 [3]. Since the WFC3 Pixel scale (0.13") is larger than that of the VLT/NACO (0.027"), few cluster member stars are discarded due to unsuccessful matching between the HST/WFC3 and VLT/NACO data. Fig. 3.10 shows the constructed CCD for one of the outskirt fields, i.e., field 5 (see Fig. 2.2). Within the matched sample with the HST/WFC3 data, at most 5% of the sources are likely to be giant contamination (Fig. 3.10, right). The residual giant contamination in the outskirts, therefore, is expected to be on the order of a few percent.

[3]These data were taken in August, 2010 under program ID 11671 (PI: Ghez). The data reduction steps and details of the observations are explained in Stolte et al. (2014b).

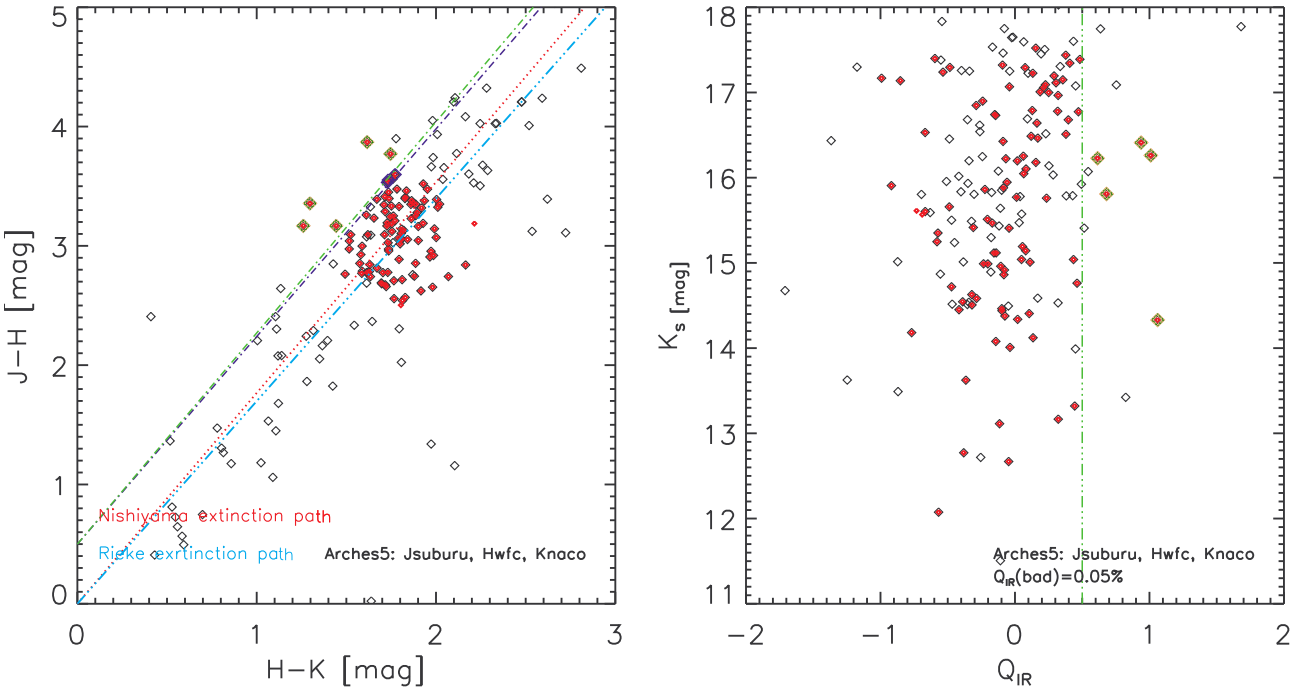

Figure 3.10: *Left:* Color-color diagram for one of the outskirt fields of the Arches cluster, field 5, using the K-band observation acquired with VLT/NACO, J-band data obtained with Subaru/CISCO and H-band data taken with HST/WFC3. Marked sources with green diamonds have $Q_{Rieke} > 0.5$. The three sources marked with blue diamonds add to the potential giant sample if we use the criterion $Q_{Nishi} > 0.5$. *Right:* The K_s magnitude is plotted over Q obtained based on the Rieke & Lebofsky (1985) extinction law. The green dashed line represents the expected Q for red giants. Within the matched sample with the HST/WFC3 data, at most 5% of the sources are likely to be giant stars.

3.2.4 Extinction map

From the individual extinction values we can construct the extinction map. Ideally, we need to have the extinction value for every point in our field. Since the extinction is only known for the places in which we observe stars, creating the extinction map means assigning each star's extinction value to its neighborhood. We use Voronoi diagrams to define the neighborhood of each star on the plane of the sky. Considering a 2-D plane ($\mathbb{R}^2$) with a finite data set of n sites (stars) $S = \{s_1, s_2, ..., s_n\}$, the i-th Voronoi cell consists of all points ($x \in \mathbb{R}^2$) whose distance to its generating site, s_i, is not greater than to any other site in the plane, $V(s_i) = \{x \in \mathbb{R}^2 \mid \forall j \neq i, d(s_i, x) < d(s_j, x)\}$.

The Voronoi diagram results in a polygon partition of the plane. Overdensities are represented as regions of small area and homogeneously spread points are reflected as polygons with comparable area, while a preferred orientation in the distribution of the

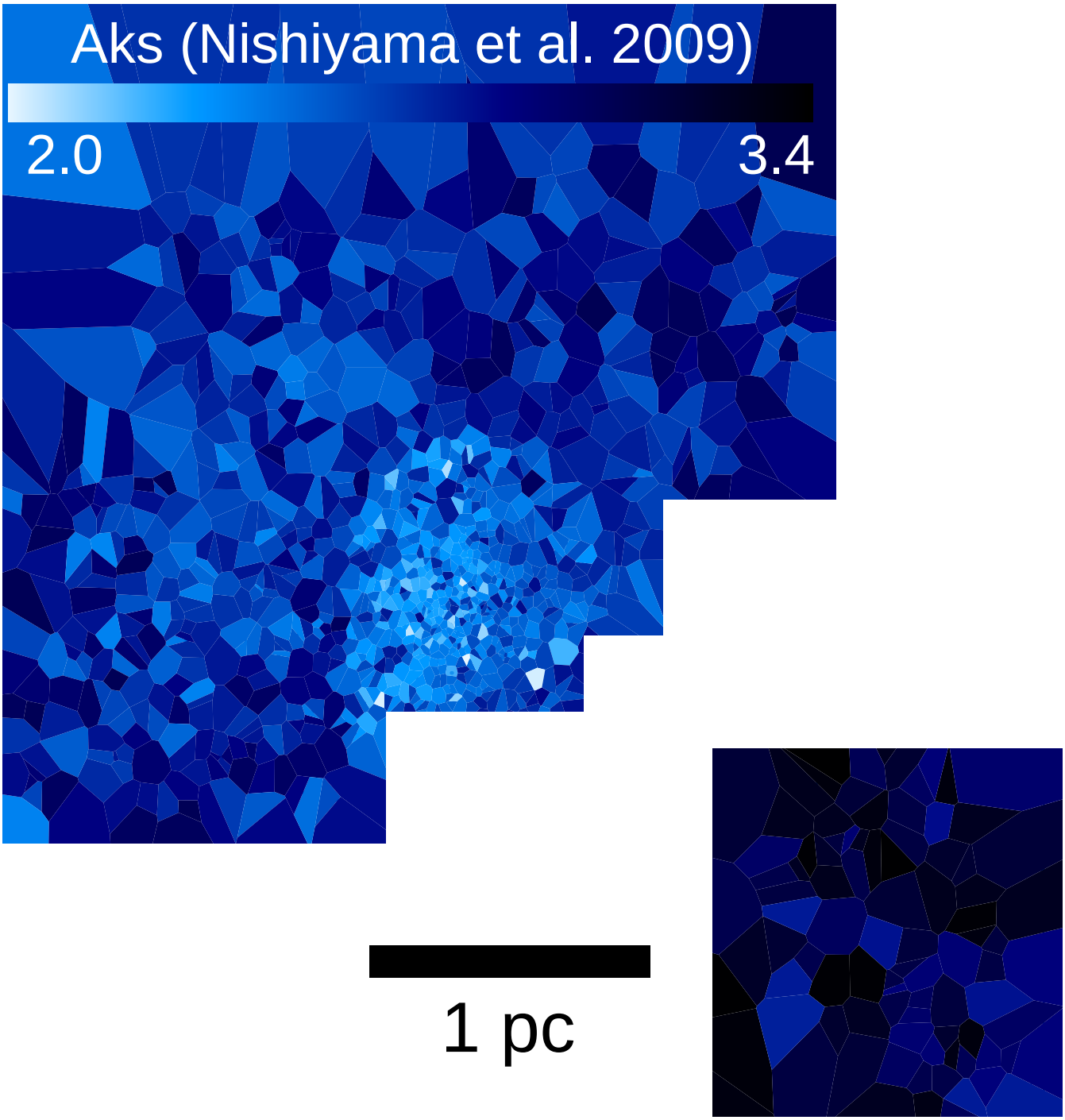

Figure 3.11: The extinction map of the Arches cluster using Voronoi diagrams. Each star is associated with one and only one cell, the color of which is determined by the measured extinction value at the location of the star. A region of lower extinction is present in the center of the cluster, while stripes of higher extinction are present in the southwest and partly northwest of the cluster. The extinction is high and varies by up to ~ 2 mag across the cluster. The extinction values derived based on the Nishiyama et al. (2009) extinction law vary between $2 < A_{K_s} < 3.4$ mag, while utilizing the Rieke & Lebofsky (1985) extinction law yields an extinction range of $2.7 < A_{K_s} < 4.5$ mag (not shown). The structure of the two extinction maps based on the two different extinction laws is only marginally different. North is up and east to the left.

points is exhibited as oriented shapes (Aurenhammer & Klein 2000). The resulting extinction map derived assuming the N-EL is shown in Fig. 3.11. Bright colors correspond to regions of low extinction while dark patches represent high-extinction areas. The inverse of the area of each Voronoi cell shows the precession of the extrapolation of the star's extinction to its region. As discussed in Sect. 3.2.1, using different extinction laws would alter the individual extinction value between 0.6 and 1.1 mag (see Fig. 3.4). However, the structure of the extinction map remains very similar when applying different extinction laws since differences in the spatial extinction distribution are small.

The K_s-band extinction derived employing the RL-EL varies between $2.7 < A_{K_s} < 4.5$ mag. In the inner core of the cluster, we see an average of $\langle A_{K_s}(r < 0.2 \text{ pc})\rangle = 3.3 \pm 0.3$ mag, as compared to a mean extinction of $\langle A_{K_s}(0.2 < r < 0.4 \text{ pc})\rangle = 3.4 \pm 0.3$ mag in the intermediate annulus and $\langle A_{K_s}(r > 0.4 \text{ pc})\rangle = 3.5 \pm 0.4$ mag in the cluster outskirts. The highest extinction is found in the southwest of the cluster (Field 2) while the least extinction is detected toward the center (Field 1). The acquired extinction values applying the N-EL are on average 0.8 mag lower than values derived based on the RL-EL. The extinction derived from the N-EL varies within the range of $2 < A_{K_s} < 3.4$ mag. The mean extinction values across the inner region of $r < 0.2$ pc, the annulus with $0.2 < r < 0.4$ pc, and the region of $< 0.4 < r < 1.5$ pc are, respectively, 2.5 ± 0.2, 2.6 ± 0.2, and 2.6 ± 0.3 mag. Reported errors on the mean extinction values are standard deviations present among individual extinction measurements in each region.

The derived values of A_{K_s} using the Rieke & Lebofsky (1985) EL are consistent with the only previous study with individual extinction correction for the Arches cluster by (Espinoza, Selman & Melnick, 2009). This study used the Fitzpatrick (2004) EL and either a Bayesian or CMD sliding method to derive extinction values that depends on the brightness and availability of JHK_s photometry for each star. They find a K_s extinction range of $2.13 < A_{K_s} < 4.14$ mag across a field of view which extends only ~ 0.5 pc from the cluster center. They also find a mean extinction value of $\langle A_{K_s}\rangle = 2.97$ in the inner core ($r < 0.2$ pc) followed by a mean extinction value of $\langle A_{K_s}\rangle = 3.18$ in the region $0.2 < r < 0.4$ pc. Espinoza, Selman & Melnick (2009) cover the cluster beyond the distance of 0.5 pc partly toward the north and west, where they report a mean extinction of $\langle A_{K_s}\rangle = 3.24$ for this area (see Espinoza, Selman & Melnick 2009, Fig. 12). These results are consistent with our findings of 3.3 ± 0.3, 3.4 ± 0.3, and 3.5 ± 0.4 mag for similar regions based on the Rieke & Lebofsky (1985) EL, which is comparable to Fitzpatrick (2004).

In a recent study, Dong, Wang & Morris (2012) also calculate individual extinction values for a number of massive stars in the GC, including 19 sources within a radius of one parsec of the Arches cluster (see Table 2 in Dong, Wang & Morris 2012). The extinction values are derived using the broadband filters J, H and K_s of SIRIUS (Nagayama et al. 2003) and by employing the extinction law of Nishiyama et al. (2006). The mean value of the derived individual A_{K_s} extinctions for these 19 sources is 2.53, which is consistent within 0.14 mag with our Nishiyama based mean extinction of $\langle A_{K_s}(r < 1\ pc)\rangle = 2.67 \pm 0.3$.

The region of low extinction in the center of the cluster is probably due to the pres-

ence of massive stars. Massive stars provide strong UV radiation and stellar winds that can disrupt the residual gas and dust (see Stolte et al. 2002). Identified X-ray sources that coincide with radio emission in the Arches cluster confirm there are powerful ionized winds from late-type Of/Wolf-Rayet stars in the center of the cluster (Lang, Goss & Rodriguez 2001; Law & Yusef-Zadeh 2003). Regions of higher extinction in the southwest and northwest of the cluster coincide with dark lanes visible in the JHK composite from the UKIDSS GPS survey (Lucas et al. 2008). Espinoza, Selman & Melnick (2009) also found an area of higher extinction toward the southwest of the cluster, that lies in the gap between Fields 1 and 2 in our work. The presence of relatively low-extinction areas in the eastern part of the outer cluster region is consistent with identified diffuse X-ray emission of the cluster which is elongated towards this area (Law & Yusef-Zadeh 2003).

Apart from the overall trend of having lower extinction values toward the center of the cluster, we find that the extinction is spatially variable both in the center and at larger radii. The extinction varies by ~ 2 mag in A_{K_s} across the cluster ($\Delta A_{K_s,RL-EL} = 1.8$, $\Delta A_{K_s,N-EL} = 1.4$), which is equivalent to roughly 15-20 mag of visual extinction. Such a high and variable extinction (as shown earlier for the center of the cluster by Espinoza, Selman & Melnick 2009) implies that using global extinction trends or even single extinction values derived by averaging individual measurements would alter the results for the Arches cluster systematically.

3.3 Mass function

To derive the PDMF of the cluster, we applied a more conservative low-mass selection in addition to the criteria imposed by sensitivity (explained in Sect. 2.1). We discarded all sources whose masses are less than the mass of the reddest source with a luminosity close to the sensitivity limit. This criterion ensures that the mass function is complete in the faintest mass bin and corresponds to an extinction-limited sample. The lowest mass included in the PDMF is 10-17$M_\odot$ depending on the field and the extinction law that is applied (see Table 3.1). The low-mass truncation is slightly different in the center since the observational set-up and completeness limit is different for the center (see Sect. 2.1). Truncating the low-mass end of the mass distribution helps to avoid the field contamination, which is dominated by K and M giants in the Galactic bulge for stars fainter than $J \sim 21$ mag. This is crucial for the outskirts of the cluster where we expect to have more contamination by field stars relative to the decreasing number of cluster members.

To avoid the bias resulting from the number of stars per bin and its assigned weight in the deriviation of the PDMF slope, we utilize the binning method described by Maíz Apellániz & Úbeda (2005). Following this method, we allow for dynamic bin sizes such that each bin contains approximately the same number of stars, hence the same statistical weight (for details about the implementation of this method see Hußmann et al. 2012).

Figure 3.12 shows the derived PDMFs of the Arches cluster on logarithmic scale

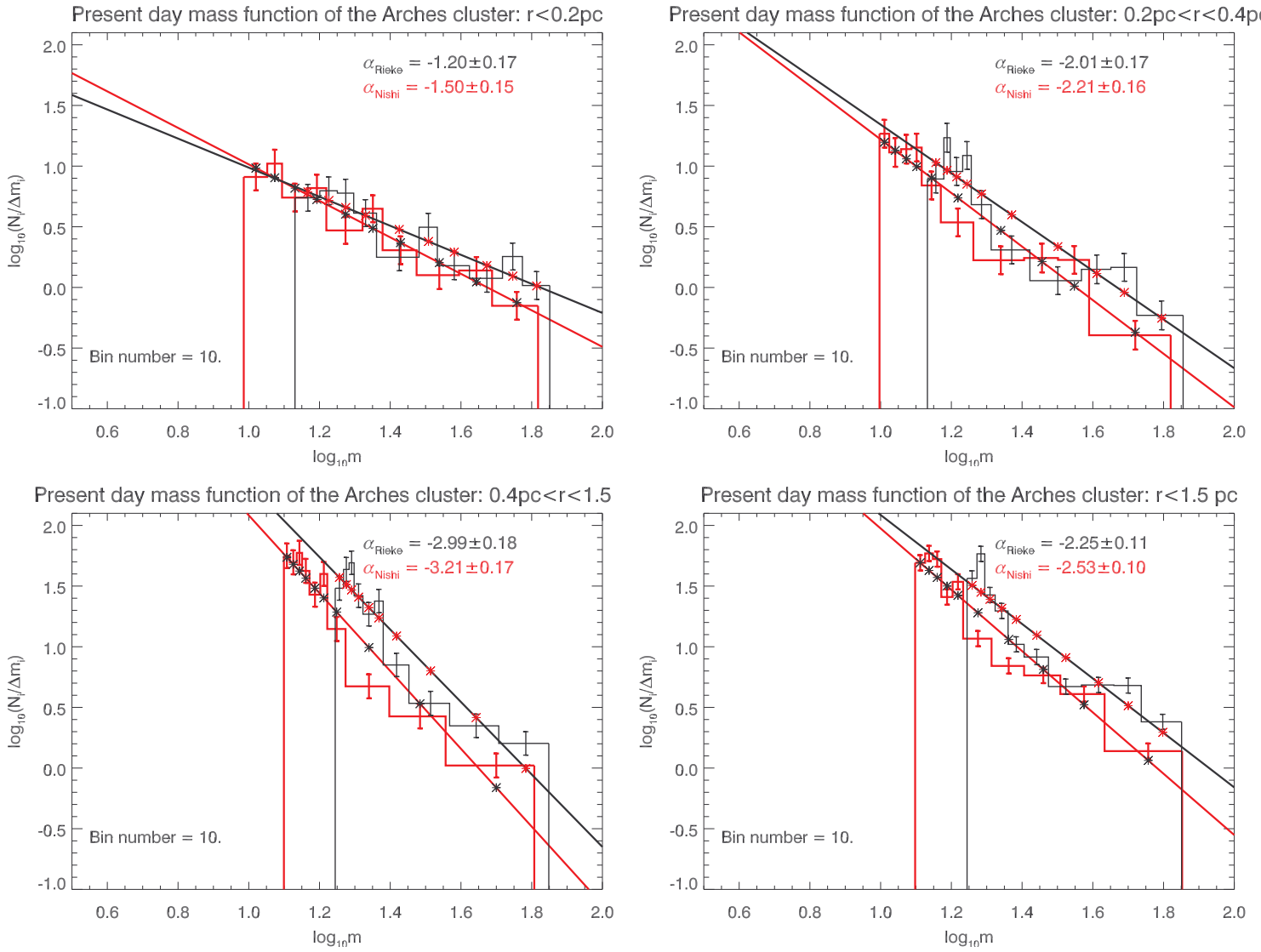

Figure 3.12: The present-day mass function of the Arches cluster. Red lines correspond to the mass distribution derived based on the N-EL, while black lines represent the mass function assuming the RL-EL. Both mass functions are fitted with a power-law like function with reported slopes of α shown in the respective color. The mass functions are plotted in three regions: (a) the inner core of $r < 0.2$ pc, (b) the intermediate annulus of $0.2 < r < 0.4$ pc and, (c) the cluster outskirts of $0.4 < r < 1.5$ pc. The mass function steepens as we move outward from the cluster center. The complete mass distribution of the cluster within $r < 1.5$ pc (d) is consistent within the uncertainties with a Salpeter IMF. The illustrated error for the slopes only represents the numerical fitting uncertainties (see Table 3.2, and Sect. 5.2 for a discussion).

Table 3.1: The minimum mass of a star that is included in the mass function sample.

Field	N-EL	RL-EL
min mass: center (F1)	$12.5M_{\odot}$	$17.5M_{\odot}$
min mass: outskirts (F2-F5)	$9.7M_{\odot}$	$13.6M_{\odot}$

Table 3.2: Acquired slopes for the mass function derived from the initial and the current masses of the Arches cluster applying the Nishiyama et al. (2009) (N-EL) and Rieke & Lebofsky (1985) (RL-EL) extinction laws. The slopes are calculated for the three different regions distinguished by the distance from the cluster center. The last row contains the same slopes for the whole cluster up to a radius of 1.5 pc.

	Nishiyama et al. (2009) EL		Rieke & Lebofsky (1985) EL	
region (pc)	PDMF, init	PDMF, P-D	PDMF, init	PDMF, P-D
$r < 0.2$	-1.63±0.17	-1.50±0.35	-1.60±0.17	-1.20±0.18
$0.2 < r < 0.4$	-2.25±0.27	-2.21±0.27	-2.20±0.27	-2.01±0.19
$0.4 < r < 1.5$	-3.16±0.24	-3.21±0.30	-3.01±0.19	-2.99±0.20
$r < 1.5$	-2.55±0.18	-2.53±0.31	-2.43±0.13	-2.25±0.14

such that a standard Salpeter mass function Salpeter (1955) is a line with a slope of $\alpha = -2.35$. The PDMFs are represented well by a single slope power-law function ($\frac{dN}{dm} \propto m^{-\alpha}$) at all radii. The PDMF of the cluster as plotted in three different regions: the inner core with $r < 0.2$ pc, the intermediate annulus of $0.2 < r < 0.4$ pc, and the outskirts which cover partly the outer annulus with $0.4 < r < 1.5$ pc. Since our fields (see Fig. 2.2) do not cover the whole area of the outer annulus, $0.4 < r < 1.5$ pc, the number of sources in each mass-bin is scaled to the observed ratio of the outer annulus area. The projected distances of 0.2 pc and 0.4 pc from the cluster center are the estimated core and half mass radius of the cluster, respectively (Figer, McLean & Morris 1999; Stolte et al. 2002; Harfst, Portegies Zwart & Stolte 2010). Most of the previous studies have used these annuli to report the mass function slopes. The radius of 1.5 pc is chosen to cover the cluster out to its tidal radius. For a detailed discussion about the tidal radius of the Arches cluster see Sect. 3.3.1.

The derived slopes using the two extinction laws (Fig. 3.12) show that changes in the slope of the fitted power-law function due to the extinction law are similar to the fitting uncertainty (for the detailed description of the systematic and the random errors of the derived slopes see Sect. 3.3.2). Kim et al. (2006) report almost no change in the slope of the mass function using the two extinction laws of Nishiyama et al. (2006) and of Rieke, Rieke & Paul (1989) for a mass range that starts at lower masses, $1.3M_{\odot} < M < 50M_{\odot}$. Since they convert K_s magnitudes into stellar masses using an average extinction value for the ensemble of stars with the justified argument that their

radial coverage is limited to $\sim 0.2-0.35$ pc (compare to our coverage of up to 1.5 pc), the effect from the extinction law slope is not expected to be large.

The choice of the extinction law applied for the individual dereddening of each star alters the shape, particularly the lower and the upper mass limits of the resulting MF. Changing the boundaries of the mass function translates to shifting the highest observed mass to lower values. This is crucial because the Arches cluster is not expected to have any supernova at its present age. Since the cluster is believed to cover the full mass range, it was used to derive a possible upper mass limit of $M = 150 M_{\odot}$ for the star formation process in the Milky Way (Figer 2005). Such an upper mass limit has severe implications for our understanding of the stellar evolution and the formation of the highest mass stars. While the most massive initial mass in our sample is $104 M_{\odot}$ when dereddening with a RL-EL, the highest initial mass is only $80 M_{\odot}$ when the N-EL is used. This suggests that the claimed upper mass strongly depends on the choice of the extinction law and should be revisited with the steeper extinction laws found toward the GC in the past few years. Such an investigation is beyond the scope of this study.

We obtain a PDMF slope of $\alpha_{Nishi} = -1.50 \pm 0.35$ in the cluster core ($r < 0.2$ pc) (see Fig. 3.12, upper left). In the intermediate annulus with $0.2 < r < 0.4$ pc, the slope of the PDMF reaches $\alpha_{Nishi} = -2.21 \pm 0.27$, which is in the range of the standard Salpeter mass function Salpeter (1955) with $\alpha = -2.35$, (Fig. 3.12, upper right). The number of massive stars compared to low-mass stars continues to decrease on the outskirts of the cluster. The PDMF for the outer annulus of the cluster, $0.4 < r < 1.5$ pc, is depleted of high-mass stars with a slope of $\alpha_{Nishi} = -3.21 \pm 0.30$ (Fig. 3.12, lower left).

A flattening of the Arches mass function toward the center has been shown in previous studies. Stolte et al. (2005) find a slope of -1.26 for the mass range of $10 M_{\odot} < M < 63 M_{\odot}$ in the inner core. This study corrected for a systematic radial extinction variation. Individual extinction corrections by Espinoza, Selman & Melnick (2009) resulted in a slope of -1.88 in the cluster core [4].

Our finding, $\alpha_{Nishi} = -2.21 \pm 0.27$, in the intermediate annulus is consistent with the slope of $\alpha = -2.28$ found by Espinoza, Selman & Melnick (2009) in the same region for stars above $10 M_{\odot}$. Kim et al. (2006) corrected for a single extinction value and found a flatter slope of -1.71 in this annulus ($0.2 < r < 0.35$ pc) only for the stars in their high-mass range ($5 M_{\odot} < M < 50 M_{\odot}$).

Since is no reported slope for the outskirts of the cluster in these previous studies, we compare our result with simulations. Harfst, Portegies Zwart & Stolte (2010) performed a series of N-body simulations to find the best model and initial conditions to reproduce the observed data of the Arches cluster. They constructed the mass function for the best fitting models, which have a King model concentration parameter of $W_0 = 3$. They consist of one model with a flat initial mass function (IMF) and three with a Salpeter IMF (see Fig. 3.13). While the models with the Salpeter IMF are more consistent

[4] Espinoza, Selman & Melnick (2009) used initial instead of present-day stellar masses to derive the mass function. The comparable slopes to Espinoza, Selman & Melnick (2009) (derived from initial masses) are shown for comparison in Table 3.2.

with the observed slopes, all the models exhibit a flattening toward the center. The three Salpeter and the one flat IMF model deviate primarily at larger radii ($r > 0.4$ pc) where the predicted slope difference is ~ 0.5 dex. The derived slope from a Salpeter IMF model by Harfst, Portegies Zwart & Stolte (2010) at the radius of 1 pc is $\alpha \sim -3$, which is in very good agreement with our finding of $\alpha_{Nishi} \sim -3.21 \pm 0.30$ on the outskirts of the cluster (Fig. 3.13). This picture is consistent with the dynamical evolution of the Arches cluster as the origin of its observed mass segregation, which implies that primordial mass segregation is not required to explain the spatial variation in the mass function slope of the Arches cluster. Obtaining the combined PDMF including all the sources within our fields up to ~ 1.5 pc yields a slope of $\alpha_{Nishi} = -2.53 \pm 0.31$, similar to the Salpeter IMF within the uncertainties (see Fig. 3.12).

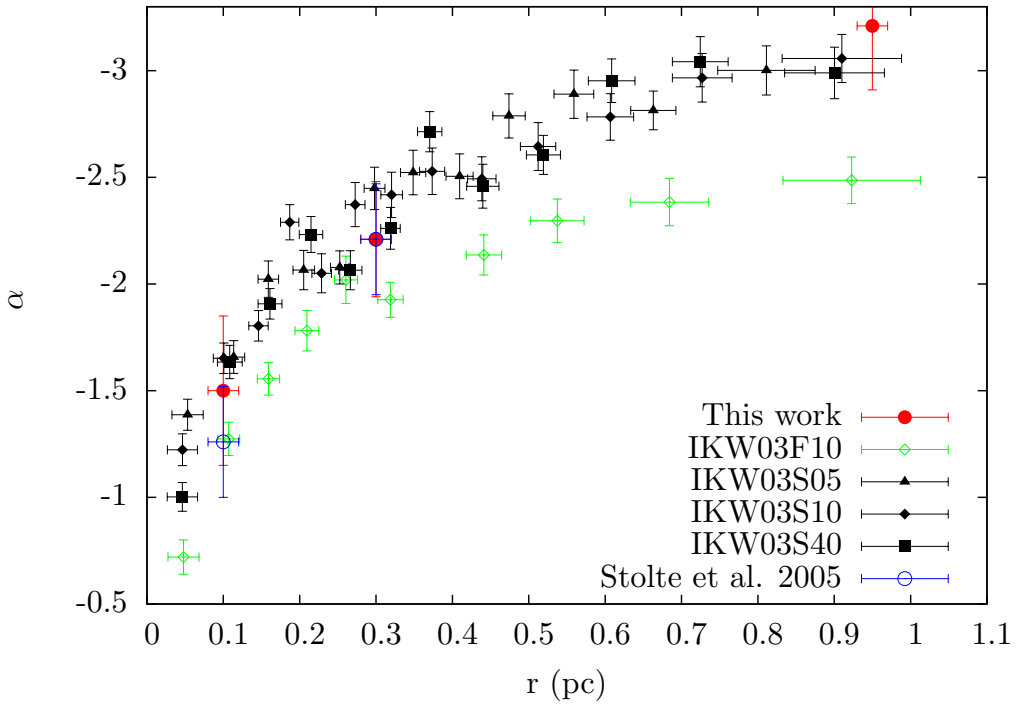

Figure 3.13: The figure is adopted from Harfst, Portegies Zwart & Stolte (2010) in their Fig. 13, and compares the mass function slopes from the best-fitting models of N-body simulations of the Arches cluster to the observed values of this work and also from Stolte et al. (2005). The black filled symbols represent the models with a Salpeter IMF with different lower mass limits, while green open symbols correspond to a model with a flat IMF. The models deviate primarily at larger radii ($r > 0.4$ pc). The derived slope from a model starting with a Salpeter IMF at birth in the radius of 1 pc is $\alpha \sim -3$, which is in good agreement with our finding of $\alpha_{Nishi} \sim -3.21 \pm 0.30$ in the outskirts of the Arches cluster.

Integrating the PDMF across the desired mass range yields the total mass of the cluster. The complete PDMF ($r < 1.5$ pc) of the cluster with a slope of $\alpha_{Nishi} =$

-2.53 ± 0.31 was integrated over the mass range of 1 - 66 $M_{\odot}$, yielding a total mass of $M_{cl} = (1.9^{+0.3}_{-0.3}) \times 10^4 M_{\odot}$ for the Arches cluster. This value is comparable within the uncertainty to the dynamical mass estimate of the cluster. Clarkson et al. (2012) measured the dynamical mass from the cluster's velocity dispersion to be $M_{cl}(r < 1.0pc) = 1.5^{+0.74}_{-0.6} \times 10^4 M_{\odot}$ for the Arches cluster. The dynamical mass of the cluster is derived from the velocity dispersion of high- to intermediate-mass stars in the cluster core ($r < 0.2$ pc), which might underestimate the total cluster mass due to the lower velocity dispersion as a consequence of mass segregation. Previous studies estimated about two times higher photometric masses for the cluster. However, their results are not directly comparable to our numbers since they were calculated over a narrower annulus (eg. Espinoza, Selman & Melnick 2009). The discrepancy can be due to an extrapolation that is based on the slopes derived from the center of the cluster ($r < 0.4$ pc) and might have resulted in overestimating the number of higher mass sources in the outskirts.

3.3.1 Tidal radius of the cluster

The projected distance of the Arches cluster is ~ 26 pc from the GC. However, since the Galactic mass distribution and the location of the cluster along the line of sight has not been determined, it is not easy to estimate the true tidal radius of the cluster. Kim et al. (2000) estimated the tidal radius of the cluster based on a power-law approximation of Galactic mass inside a Galactocentric radius, r_g. Their comparison between the simulated projected number density and the observed mass functions at the time did not rule out a Galactic distance, r_g, of 20 and 50 pc for the Arches cluster, but favored $r_g = 30$ pc, which results in a tidal radius of ~ 1 pc. A similar study by Portegies Zwart et al. (2002) concludes that to reproduce the observed density within the half-mass radius, the Arches cluster should lie at the distance of 50-90 pc from the Galactic center, which results in a tidal radius of 1.6-2.5 pc (see Portegies Zwart et al. (2002), their Table 4).

A more recent study by Launhardt, Zylka & Mezger (2002b) estimates the enclosed mass in the inner 500 pc of the Milky way. This observational study shows that the potential in the inner Galaxy cannot be modeled with a single power law and takes the mass contribution of the nuclear stellar cluster, the nuclear stellar disc, the central black hole, the Galactic bulge, and the interstellar mass in the nuclear bulge into account (see Launhardt, Zylka & Mezger 2002b, Fig. 14). Applying the enclosed mass from the Launhardt, Zylka & Mezger (2002b) model, M_g, for the Galactocentric range of r_g =30-100 pc and a cluster mass of $M_{cl} \sim 19000 M_{\odot}$ yields a tidal radius, r_t, of $1.6 - 2.5$ pc:

$r_t = (\frac{M_{cl}}{2 \times M_g})^{1/3} \times r_g \simeq 1.6 - 2.5$ pc.

We observed the Arches cluster out to 1.5 pc, which is close to the range of the derived tidal radii.

Table 3.3: Source list. From left to right the columns are: Sequential ID for stars, R.A. offset from the reference star which is the source with ID 1 (R.A.=17:45:50.046 , Dec. = -28:49:23.62), DEC. offset from the reference star, measured J-band, H-band, and K_s-band brightness, along with the photometric uncertainty in K_s (columns 4-7), estimated K_s-band extinction by applying the RL-EL (column 8) and the N-EL (column 9), present-day mass applying the RL-EL (column 10) and the N-EL (column 11), initial mass applying the N-EL (column 12), and the cluster field in which the detected source is located (column 13). When one of the above values is not available for a source it is denoted as -9999 in the table.

ID	$\triangle R.A.$ (sec)	$\triangle Dec.$ (sec)	J (mag)	H (mag)	K_s (mag)	σ_{K_s}	$A_{K_s(RL-EL)}$ (mag)	$A_{K_s(N-EL)}$ (mag)	PDM_{RL-EL} $M_\odot$	PDM_{N-EL} $M_\odot$	IM_{N-EL} $M_\odot$	field
1	0	0	16.79	13.59	11.54	0.007	3.47	2.67	61	52	54	1
2	10.261	-2.708	-9999	12.38	10.25	0.005	3.58	2.76	71	65	78	1
3	6.817	6.062	14.89	12.16	10.25	0.008	3.68	2.84	71	65	77	1
4	2.071	1.391	15.63	12.37	10.29	0.013	3.55	2.74	68	62	71	1
5	4.487	2.395	15.39	12.41	10.43	0.007	3.34	2.58	65	61	67	1

The complete table of the sources will be published in the electronic edition of the A& A journal.

3.3.2 Uncertainties of the mass function slopes

The uncertainties of the PDMF slopes illustrated in Fig. 3.12 represent the numerical fitting uncertainties ($\sigma_{fit} \sim 0.15$). There are also systematic errors that contribute to the final estimated Uncertainties. One source of systematic uncertainty originates from the cluster age, metallicity, and the corresponding choice of the isochrone. Studies determining the age of the Arches cluster are based on spectroscopy of nitrogen-rich (WN) Wolf-Rayet stars (WRs) and O super-giants, along with the absence of carbon-rich WR stars that establish an upper limit for the age of the cluster. Although studies agree on a narrow evolutionary spread and subsequently a narrow age spread among the cluster stars, it is still hard to confine the absolute age of the Arches cluster. Blum et al. (2001) studied 2 μm narrow-band images and derived an age of 2-4 Myr assuming the stars are of WR type. Najarro et al. (2004) analysed spectra of five massive stars (classified as 3 WNLs and 2 O stars) and obtained an age of 2-2.5 Myr. They derived solar metallicity for all the five sources based on measuring their N abundances. More recent work by Martins et al. (2008b) used K-band spectra of 28 bright stars in the cluster. An age of 2-3 Myr was obtained for WN7-9 stars while some O super-giants could have ages up to 4 Myr. They suggested that lighter elements are probably slightly super-solar though iron peak elements show solar metallicity. Espinoza, Selman & Melnick (2009) built mass functions using different ages (2-3.2 Myr) and show that the uncertainty from the choice of age or metallicity will add an uncertainty of $\sigma_{iso} \sim 0.1$ dex. This result agrees with Hußmann et al. (2012), who applied different isochrones (3-5 Myr) to construct the PDMF of the Quintuplet cluster.

The second significant source of uncertainty stems from the choice of the extinction law (see Sect. 3.2). We conclude that if none of the extinction laws can be disregarded based on the scientific discussion (see Sect. 3.2.1 and Fig. 3.6), an uncertainty of 0.17 dex should be considered as a result of the choice of the extinction law (see Fig. 3.12 and Table 3.2). Applying the steeper extinction laws (Nishiyama et al. 2009; Schödel et al. 2010; Stead & Hoare 2009) steepens the slope of the PDMF by $0.03 - 0.30$ dex (see Fig 3.12). It is important to notice that this steepening is a systematic uncertainty. Although all the sources of random and systematic errors are detached and reported above, for the sake of comparison with previous studies with different assumptions about the extinction law and the age of the cluster, we approximate the mean overall uncertainty in the PDMF slope as a quadratic sum of random and systematic errors of ~ 0.24 dex as a result of all the uncertainties discussed above ($\sigma_{fit}, \sigma_{iso}, \sigma_{EL}$). The individual overall uncertainties are shown in Table 3.2.

3.4 Conclusions

We derive the present-day mass function of the outskirts of the Arches cluster for the first time to obtain a full understanding of the cluster mass distribution up to its tidal radius. The K_s and H-band AO images taken with the VLT as well as J-band images obtained with Subaru are analyzed for this investigation. We also present a quantitative study on the effect of the applied extinction law on the derivation of the mass function

in young massive star clusters using the Arches cluster as a template. We show how the choice of the near-infrared extinction law influences the absolute values of the patchy extinction toward the star clusters in the Galactic center, and how it affects the slope of the mass function. The main findings of this chapter are as following:

1. The extinction law derived by Rieke & Lebofsky (1985), $A_\lambda \propto \lambda^{-1.61}$, was used commonly in previous studies toward the Arches cluster. We compare the results obtained from Rieke & Lebofsky (1985) to the results acquired assuming the extinction law derived by Nishiyama et al. (2009), as several recent studies toward the GC suggest a steeper wavelength dependence of $A_\lambda \propto \lambda^{-2}$ for the near-infrared extinction law. Applying these different extinction laws results in an average systematic extinction difference of $\Delta A_{K_s} = 0.8$ mag ($\sim 24\%$), which can reach up to 1.1 mag. The obtained average extinction values applying the Nishiyama et al. EL are 2.5 ± 0.2, 2.6 ± 0.2, and 2.6 ± 0.3 mag for the three investigated cluster annuli of $r < 0.2$ pc, $0.2 < r < 0.4$ pc, and $0.4 < r <\sim 1.5$ pc, respectively. Applying the Rieke & Lebofsky EL increases the average extinction values to 3.3 ± 0.3, 3.4 ± 0.3, and 3.5 ± 0.4 mag using the same sample of cluster stars.

2. The extinction map derived by individual dereddening of the cluster member candidates shows a high and variable extinction across the cluster. The derived extinction values applying the Nishiyama et al. (2009) extinction law and Rieke & Lebofsky (1985) vary within the range of $2 < A_{K_s} < 3.4$ mag and $2.7 < A_{K_s} < 4.5$ mag, respectively. The patchiness of the extinction is high and hardly follows any trend; nevertheless, a region of relatively low extinction is present toward the center of the cluster. An area of high extinction is located in the southwest and partly northwest of the cluster.

3. Obtained stellar masses assuming the Nishiyama et al. (2009) extinction law are $\sim 30\%$ less massive than derived masses assuming the formerly used extinction law by Rieke & Lebofsky (1985). Considering that the Arches cluster hosts a collection of high-mass stars, a mass difference of $\sim 30\%$ can change the estimated individual initial masses substantially. In this work, the initial mass of the most massive star in our sample decreases from 104 $M_\odot$ to 80 $M_\odot$ when using the steeper extinction law, which has severe implications for discussion of the possible maximum stellar mass forming in the Milky Way (see Sect. 3.3 for a detailed discussion).

4. We derive the present-day mass function of the Arches cluster for an area that reaches out to the tidal radius. Our mass functions cover the high-mass part of the mass spectrum (see Table 3.1) and are obtained in three different annuli of $r < 0.2$ pc (core), $0.2 < r < 0.4$ pc (intermediate annulus), and $0.4 < r < 1.5$ pc (outer annulus). The slopes derived by assuming the Nishiyama et al. (2009) extinction law increase from a flat slope of $\alpha_{Nishi} = -1.50 \pm 0.35$ in the core to $\alpha_{Nishi} = -2.21 \pm 0.27$ in the intermediate annulus, which steepens

to $\alpha_{Nishi} = -3.21 \pm 0.30$ in the outer annulus. It is important to notice that uncertainties from the assumption of the extinction law and the age of the cluster are systematic. The slope derived by applying the Rieke & Lebofsky (1985) EL are on average flatter by 0.17 dex. Our mass functions show that, while in the core of the cluster the number of massive stars is greater than lower mass ones when comparing to the normal Salpeter mass function ($\alpha = -2.35$, Salpeter 1955), the intermediate annulus has a Salpeter-like distribution, and the outskirts are depleted of high-mass stars. Comparing the mass function slopes of the cluster with the N-body simulations performed by Harfst, Portegies Zwart & Stolte (2010), we conclude that the radial variation observed in the present-day mass function slopes is consistent with dynamical evolution of a cluster that formed with a normal Salpeter IMF.

5. The extrapolation of the complete PDMF for the area of $r < 1.5$ pc, derived for a present-day mass range of 1-66 $M_{\odot}$ and a slope of $\alpha_{Nishi} = -2.53 \pm 0.31$, results in a total mass of $M_{cl} = (1.9^{+0.3}_{-0.3}) \times 10^4 M_{\odot}$ for the Arches cluster.

It was argued before that the IMF might be top-heavy in the GC because of increased cloud temperatures and magnetic fields (Morris 1993, Dib, Kim & Shadmehri 2007, see also Klessen, Spaans & Jappsen 2007 and Stolte et al. 2005 for discussions). The slopes derived in our analysis are consistent with the expectations of the dynamical evolution of the cluster starting with a Salpeter IMF at birth. We therefore do not need to invoke a primordially deviating mass function to explain the spatial distribution of stars in the Arches cluster.

Chapter 4

Isolated massive stars in the Galactic center: The dynamic contribution from the Arches and Quintuplet star clusters

This chapter is published in Astronomy & Astrophysics: "Isolated massive stars in the Galactic center: The dynamic contribution from the Arches and Quintuplet star clusters", Habibi, M., Stolte, A., Harfst, S., 2014, A&A, 566, A6.

Contents

4.1 Introduction

Galactic nuclei are ideal laboratories to investigate star formation in extreme conditions, such as in a strong tidal field, high UV radiation, and a strong magnetic field. The only galactic nucleus where we can resolve the stellar population into individual stars is the center of our Galaxy at a distance of $\sim 8.0\,\mathrm{kpc}$ (Ghez et al. 2008, Gillessen et al. 2009). However, the conditions for star formation and the dynamics of this region have

yet to be understood as it harbors dense molecular clouds, a high star formation rate per unit volume, and the largest concentration of massive stars and star clusters in the Milky Way (e.g., Morris & Serabyn 1996b; Figer & Morris 2002; Ferrière, Gillard & Jean 2007).

The Galactic center (GC) region hosts three starburst clusters with masses in excess of $\sim 10^4\,M_\odot$ and core radii of $\sim 0.15 - 1\,\mathrm{pc}$ (Eckart et al. 1993; Figer et al. 2002; Espinoza, Selman & Melnick 2009). These three compact and massive clusters are the young nuclear cluster surrounding the supermassive black hole, the Quintuplet cluster, and the Arches cluster. Recent observations of isolated sources in the GC region revealed that the field stars in this area, similar to these three clusters, encompass many massive sources (Dong et al. 2011a; Mauerhan et al. 2010a; Mauerhan et al. 2010b; Wang et al. 2010). A population of distributed, very massive Wolf-Rayet (WR) stars with initial masses in excess of $20-40\,M_\odot$ were detected within a few dozen of pc from the super-massive black hole, Sgr A*, by X-ray observations, which are accompanied by spectroscopic studies and Paschen-α (Paα) narrow-band imaging with Hubble Space Telescope (HST) (Wang et al. 2010; Dong et al. 2011a). Up to now, more than 100 WR stars and O supergiants have been spectroscopically identified in the Galactic center region (Mauerhan et al., 2010a), including the known cluster members.

As about a third of these sources are located outside of the three massive starburst clusters, it has been suggested that they provide evidence for *isolated* high-mass star formation in the GC (Dong et al. 2011b, Oskinova et al. 2013). Observations of massive stars in the solar neighborhood show that generally massive stars form in groups and associations (Lada & Lada 2003; Zinnecker & Yorke 2007; Gvaramadze & Bomans 2008), but it is not clear if we can generalize these findings to different galactic environments. On the other hand, dynamical evolution of stellar populations in the GC region can become dramatic under the strong effect of the GC tidal field. If so, dense and massive clusters like the Arches and Quintuplet can shape the distribution of the field stars in the region.

The Arches and Quintuplet clusters have been observed to be already mass segregated at ages of $2-6\,\mathrm{Myr}$. A recent study by Hußmann et al. (2012) showed that the Quintuplet cluster at an age of 3-5 Myr exhibits a flat mass function slope of -1.68 ± 0.1 in the cluster center compared to the standard Salpeter (1955) initial mass function (IMF) of -2.3. A similarly flat mass function was found in the central region of the Arches cluster, but the slope increases substantially toward larger radii (Figer et al. 1999, Stolte et al. 2005, Espinoza, Selman & Melnick 2009, Habibi et al. 2013). A study by Harfst, Portegies Zwart & Stolte (2010) implemented N-body simulations of the Arches cluster to investigate the internal dynamical evolution of the cluster. By comparing their models to the observational data from the central 0.4 pc of the Arches cluster, they could constrain the initial conditions and construct a dynamical model of the Arches cluster that best represented the central stellar mass distribution, hereafter the best-fitting model of the Arches cluster. From this model, a steep increase of the stellar mass function slope as a function of the cluster center distance was predicted. The Arches cluster was later studied by Habibi et al. (2013) to a larger radius of $\sim 1.5\,\mathrm{pc}$. Observations of the high-mass part of the mass spectrum in this study

($M >\sim 10 M_{\odot}$) revealed a depletion of massive stars in the cluster outskirts. In this previous study, we compared the measured slope of the mass function to the slopes predicted by the N-body simulations in different annuli out to the tidal radius of the Arches cluster. This comparison showed that the Arches cluster exhibits characteristics of a normal, which is defined as a cluster with a normal initial mass function, but dynamically evolved cluster. The dynamical evolution of the Arches and Quintuplet clusters, however, not only changes the distribution of stars inside the cluster, but also changes the distribution of field stars in the GC region. Through gravitational interactions between stars in dense, compact clusters, stars can accelerate to become runaways (e.g., Poveda, Ruiz & Allen 1967; Gies & Bolton 1986). Moreover, the dynamical evolution of clusters under the influence of the Galactic tidal field leads to the formation of tidal arms. These tidal structures are mostly observed for globular clusters, which evolve for many Gyrs (e.g., Odenkirchen et al. 2001). As massive clusters in the GC dissolve within a few Myrs (Kim et al. 2000; Portegies Zwart et al. 2001a), dynamical evolution under the effects of the strong tidal field of the GC leads to the formation of extended tidal structures during shorter timescales. These tidal structures, in turn, can significantly contribute to the field stars in the GC region.

In this study, we analyze the best-fitting Arches model presented by Harfst, Portegies Zwart & Stolte (2010), which is extended to incorporate the effect of the Galactic center tidal field, to investigate the contribution of the Arches and Quintuplet clusters to the observed population of isolated massive stars detected by Mauerhan et al. (2010a). This paper is organized as follows: In Sect. 4.2, a summary of observational studies to detect massive stars in the GC region with our criteria to construct an observational reference sample is presented. In Sect. 4.3, we describe the computational methods, a grid of different models based on distinct physical assumptions, and a method to find the best-matching model to reproduce the observations. In Sect. 4.4, we analyze this best-matching model to derive the spatial distribution of the massive drifted sources compared to the observed population. The velocity distribution of the drifted sources from the modeled clusters and their expected spatial and mass distributions are also predicted in this section. A summary of our findings is presented in Sect.4.5.

4.2 The observed population of Wolf-Rayet stars and O supergiants

A recent HST/NICMOS Paα survey of the Galactic center was carried out by Wang et al. (2010) to study the distribution of young massive stars in the GC region. The survey covered the central region of the Galaxy, $\approx 0.65^{\circ} \times 0.25^{\circ}(l, b)$. At the distance of the GC from the Sun (8 Kpc; Ghez et al. 2008, Gillessen et al. 2009), an angular distance of 1° corresponds to a projected distance of ≈ 140 pc, such that the survey covers an area of $91 \times 35\,\mathrm{pc}^2$. Wang et al. (2010) employed two narrow band filters, F187 (1.87 μm) and F190 (1.90 μm), to detect sources with Paα excess. The Paα emission line (1.87 μm) is the strongest line in the infrared band, which mainly originates in warm

and hot ionized gas. Accordingly, Paα point sources are chiefly produced by evolved massive stars (Mauerhan et al., 2010a). Later, Mauerhan et al. (2010a) performed a follow-up near-infrared spectroscopic survey targeting the strongest Paα sources with bright K_s-band counterparts ($K_s < 12.7$ mag). For this reason, Mauerhan et al. (2010a) employed the JHK_s photometry down to 15.6 mag, which is taken from the 2MASS and SIRIUS catalogs (2MASS: Two Micron All Sky Survey; Cutri et al. 2003, SIRIUS: Simultaneous three-color InfraRed Imager for Unbiased Surveys; Nagayama et al. 2003). These magnitude ranges cover the predicted magnitude for WR stars in the GC region, which is dominated by WNL (late nitrogen-rich WR) stars ($K < 12$; Figer 1995). Fainter WNE (early nitrogen-rich WR) stars are still detectable due to their strong Paα emission. Therefore, their sample of WN (nitrogen-rich WR) stars in the Paα survey area is nearly complete, whereas the provided sample of WC (carbon-rich WR) stars is presumably not as complete (see Sec 6.1 of Mauerhan et al. (2010a) for a detailed discussion).

In this study, we use the catalog of isolated massive sources in the GC that is provided by Mauerhan et al. (2010a) to perform a statistical analysis. Mauerhan et al. (2010a) present a catalog of all the identified evolved massive stars in the GC, including their newly discovered sources. This includes those previously identified in the Arches, Quintuplet and the Nuclear star clusters, as well as those found outside the Paα survey coverage. In the presented catalog by Mauerhan et al. (2010a), sources that lie outside the Paα survey area (located at galactic longitudes of $0.2° \lesssim l \lesssim 0.6°$) are taken from the study by Mauerhan et al. (2010b).

Mauerhan et al. (2010b) performed a spectroscopic study on a pre-compiled list of potential near-infrared counterparts to hard X-ray sources. They derived the candidate list by matching the Chandra catalog of X-ray sources in the central $2° \times 0.8°(l, b)$ of the galaxy (Muno et al., 2009) to the available near-infrared surveys in the region. However, the studied sample by Mauerhan et al. (2010b) in the region outside the Paα survey area suffers from selection bias. For the spectroscopic follow-up, Mauerhan et al. (2010b) give precedence to the sources close to previously observed diffuse mid-infrared structures. Diffuse infrared emission is the characteristic of young star-forming regions in the GC. Mauerhan et al. (2010b) mostly studied these regions which may harbor ongoing star formation with the hope to enhance the detection rate of massive stars. To avoid the selection bias, we limit our sample to the region that is covered by the Paα survey by selecting sources at longitudes $l < 0.23°$ and latitudes $b > -0.1°$ from their catalog (see Fig. 4.3). We utilize this truncated list of observed isolated massive sources as our observational reference sample[1]. The final employed list of 35 observed isolated massive stars in the GC region is presented with positions and spectral types in Table 4.2, along with their reference studies. This table contains 13 WN stars, 11 WC stars, 1 LBV star, and 10 OB supergiants outside the three clusters in the Paα

[1] A more recent study by Dong, Wang & Morris (2012) includes fainter massive field stars in the GC ($Ks \gtrsim 13$ mag). Their catalog is not employed in our study, as most of these stars still do not have available spectroscopic identifications. Moreover, as they have not performed a spectroscopic survey, the spatial distribution of sources with previous spectroscopic identifications is probably biased to the target area of earlier studies.

survey region (see Fig. 4.3).

4.3 Dynamical cluster model

4.3.1 N-body simulations

The dynamical cluster models presented here are based on the work by Harfst, Portegies Zwart & Stolte (2010), who compared the results of numerical simulations with the observational data from the central 0.4 pc of the Arches cluster in detail (Stolte et al., 2005). They constrained the initial conditions and found a best-fitting Arches model. This best-fitting Arches model is used here as a starting point for the simulations.

The setup of the dynamical models of the Arches cluster, as described in the following, is similar to the models presented by Olczak et al. (2012). For our simulations, the age of the Arches cluster is set to $t_{\rm age} = 2.5\,{\rm Myr}$ (Blum et al. 2001; Najarro et al. 2004; Martins et al. 2008b), and we assume that the cluster is initially (at $t = 0\,{\rm Myr}$) gas-free and in virial equilibrium and that its mass is distributed by following a King profile (King, 1966). A single-aged stellar population is used, and no initial mass segregation is taken into account.

According to the best-fit model of Harfst, Portegies Zwart & Stolte (2010), the observed present-day mass function of the Arches cluster is the result of a dynamically evolved Salpeter IMF (Salpeter 1955) at the given age of the cluster. The total mass of the cluster is then given by the total number of massive stars (stars with $m > 10\,M_\odot$ which are complete in the observational data) and the lower mass limit of the IMF. For the latter, we adopt $m_{\rm low} = 0.5\,M_\odot$. As a result, the total mass of the cluster model is $M = 4.8 \times 10^4\,M_\odot$, which corresponds to an initial number of massive stars of $N_{m>10M_\odot} \approx 500$.

The King profile concentration parameter was set to $W_0 = 3$. The initial size of the cluster is given by the initial virial radius, which was set to 0.77 pc (see Harfst, Portegies Zwart & Stolte 2010). The corresponding core radius is about 0.4 pc initially, and shrinks down to the observed 0.2 pc due to the dynamical evolution of the cluster (Espinoza, Selman & Melnick, 2009).

Stellar evolution and the orbit of the Arches cluster in the Galactic center potential have been neglected in the best-fit model of Harfst, Portegies Zwart & Stolte (2010). Here, we extend that model, as described below, to include these two effects. The simulations were carried out with the direct N-body code `kira` from the *starlab*-package (McMillan 1996; Portegies Zwart et al. 2001b; Hut 2003), which includes modules for stellar evolution and an external potential. The stellar evolution module includes mass loss by stellar winds and binary evolution (Eggleton, Fitchett & Tout 1989; Portegies Zwart & Verbunt 1996; Tout et al. 1997; Langer 1998). The external potential that was used in our simulations is that of a power-law mass distribution with $M_{\rm gal}(r) = 4.25 \times 10^6 (r/{\rm pc})^{1.2}\,M_\odot$ and is based on Mezger et al. (1999).

The cluster orbit in the potential is given by the six phase space coordinates composed of the 3D position and velocity of the cluster at any given time. For the present day ($t = 2.5$ Myr), we know the line-of-sight velocity ($95\,{\rm km\,s^{-1}}$, Figer et al. 2002)

and the projected position (26 pc from the Galactic center). Additionally, Stolte et al. (2008a) determined the proper motion of the Arches cluster and found a 2D velocity of $212\,\mathrm{km\,s^{-1}}$ (anti-)parallel to the Galactic plane. The proper motion of the cluster was later revised to a slightly lower value of $172 \pm 15\,\mathrm{kms^{-1}}$ (see Clarkson et al. (2012) for details). We have therefore adopted the mean present-day 2D velocity of 190 $\mathrm{kms^{-1}}$ for our cluster simulations. As the difference in the 3D space motion is small, we do not expect the orbit to change substantially. If we define a coordinate system in which the x-axis is along the Galactic plane, the y-axis along the line-of-sight, and the z-axis toward the Galactic north pole, we obtain the following vectors for the position, $\boldsymbol{r}_{\mathrm{cluster}}$, and velocity, $\boldsymbol{v}_{\mathrm{cluster}}$, of the cluster at the present epoch:

$$\begin{aligned} \boldsymbol{r}_{\mathrm{cluster}} &= (-24,\ R_{\mathrm{GC}} + d_{\mathrm{los}}, 10)\,\mathrm{pc} \\ \boldsymbol{v}_{\mathrm{cluster}} &= (-190, 95, 0)\,\mathrm{km\,s^{-1}}, \end{aligned} \tag{4.1}$$

where the not well-known d_{los} determines the distance of the cluster to the Galactic center along the line of sight. Stolte et al. (2008b) discussed the formation of the Arches cluster inside the central 200 pc of the Galaxy as one of the most likely formation scenarios. Furthermore, considering its orbital properties and the measured foreground extinction of the cluster, which is lower than the extinction found toward the central parsec, Stolte et al. (2008b) concluded that the cluster is likely in front of the GC today. For the simulations, we therefore assume a line-of-sight location of $d_{\mathrm{los}} = -100\,\mathrm{pc}$ in front of the GC at its present age of 2.5 Myr.

The present-day position and velocity can be used to numerically integerate the orbit backwards in time to find the initial position and velocity at $t = 0$ Myr. From there, the full cluster was integrated in `kira` until $t = 6\,\mathrm{Myr}$, which includes the effects of stellar evolution and the GC tidal field. A total of ten random realizations of this model were integrated to allow for statistical analysis. A full snapshot of the cluster (mass, position, and velocity for every star) was stored every $\sim 0.5\,\mathrm{Myr}$. From these snapshots, the projection on the plane of the sky is easily obtained.

4.3.2 Model grid

The Arches and Quintuplet clusters share similar characteristics. Other than their proximity, observations yield similar estimates of the present-day mass of the clusters (Hußmann (2014), Habibi et al. (2013), Clarkson et al. (2012)). Additionally, preliminary results on the proper motion study of the Quintuplet cluster suggests that the motion of the Quintuplet cluster is similar to the orbital motion of the Arches cluster (Stolte et al., 2014a). However, the Quintuplet is slightly older than the Arches (2-3 Myr vs 3-5 Myr, Najarro et al. (2004) and Figer, McLean & Morris (1999), respectively) and appears to be more dispersed than the Arches cluster. Quintuplet is more than 100 times less dense than the Arches cluster (Figer, 2008). These properties are suggestive to consider the Quintuplet cluster as an older representation of the Arches cluster.

To model the observed population of massive field stars in the GC region, we need to consider the contribution of both the Arches and the Quintuplet clusters. Our simulated cluster provides the contribution from the Arches cluster. We assume the Quintuplet cluster is a snapshot of the Arches cluster at older ages as it evolves in the GC region. To construct a single model that contains both the Arches and Quintuplet clusters, the data from the two simulated clusters are combined, so that their projected distance on the plane of the sky matches the observations. Assuming the GC distance of 8 kpc, the observed separation of the clusters along the Galactic plane and the Galactic north pole is ~ 6 pc and ~ 11 pc, respectively.

Our models do not include the Nuclear cluster, since we do not expect that ejected sources from the Nuclear cluster linger in the GC region. Schödel, Merritt & Eckart (2009) observed the proper motions of stars within a distance of 1.0 pc from Sgr A*. They found few stars with proper motion velocities, which exceed 400 $\mathrm{km\,s^{-1}}$ in both the radial and tangential axes. Out of these candidates only one source has a velocity uncertainty below 1σ. It is noteworthy that the black hole governs the dynamics close to the center of the Nuclear cluster. However, as first pointed out by Hills (1988), mechanisms like interaction of a massive binary with the black hole produce ejectors with hyper-velocities of $\gtrsim 1000\,\mathrm{km\,s^{-1}}$. These hyper-velocity ejecta traverse our target region of 50 pc around the GC in $\sim 10^4$ yrs. Comparing this value to the maximum predicted ejection rate of $10^{-4}\mathrm{yr}^{-1}$ (Yu & Tremaine (2003); Perets, Hopman & Alexander (2007)), we expect ~ 1 hyper-velocity star originated in the Nuclear cluster to contribute to the observed sample of massive stars in the GC at any given time.

To obtain an estimate of the number of drifted sources[2], which are expected to originate in the Quintuplet, we evolve the model for a longer time. The age of the Arches cluster is estimated to be 2.5 Myr. The age of the Quintuplet cluster, however, is less constrained. Figer, McLean & Morris (1999) conducted a photometric and spectroscopic study on massive stars in the cluster and derived an age of 3 to 5 Myr based on the types of the stars they found. A more recent spectral analysis of WN stars by Liermann et al. (2010) favors a younger age of 3 million years, while OB stars in the cluster populate a 4 Myr isochrone on the HR diagram (Liermann, Hamann & Oskinova, 2012). To account for the age uncertainty of the Quintuplet cluster, we use three different snapshots of our model at 4, 4.5, and 5 Myr to represent the current extended population originating from the Quintuplet. Each of the three snapshots are combined with the Arches model at 2.5 Myr to estimate the total number of isolated massive stars originating from both clusters in the GC today.

Another parameter, which has a significant effect on the predicted number of WR stars in the region, is the minimum initial mass of a WR progenitor star. A WR star represents a massive star at its late evolutionary stage. Eldridge & Tout (2004) concluded that the minimum initial mass of a WR progenitor is $\sim 25\,M_\odot$ at solar metallicity. However, modeling WR stars is still a topic of active research. Recent Geneva stellar evolution tracks (Ekström et al., 2012) determine a minimum initial

[2]We consider sources outside the tidal radius (~ 1.6 pc; Habibi et al. 2013) of the Arches and Quintuplet clusters (Hußmann 2014) that are part of the tidal arms as drifted sources.

mass of $32\,M_\odot$ for a He-burning star with an age of 5.26 Myr. In these models, the minimum initial mass of a 4.97 Myr star, which is at its core He-exhaustion phase, is $40\,M_\odot$. For rotating models, these numbers are higher and are close to $60\,M_\odot$. Since observed WRs are defined by their prominent broad emission lines, the spectral analysis of WR stars is only possible through detailed model atmospheres. Hamann, Gräfener & Liermann (2006) performed a spectral analysis on a large sample of Galactic WN stars using the Potsdam Wolf-Rayet (PoWR) model atmosphere code. Based on the rough qualitative agreement of their analysis and available non-rotating Geneva tracks at the time (Meynet & Maeder, 2003), they found a minimum initial mass of $37\,M_\odot$ for a star to reach any WR phase. Later, Sander & Hamann (2012) studied Galactic WC stars using the same model atmosphere code. They conclude that these stars are evolved from progenitors of 20 to $45\,M_\odot$. On the basis of current knowledge of evolved massive stars, we consider three different minimum initial masses of 20, 40, and $60\,M_\odot$ for a star to eventually evolve into a WR star.

Based on these different assumptions about the age of the Quintuplet cluster and the initial mass of the WR progenitors, we construct nine models of massive stars in the Arches and Quintuplet clusters. We compare the population of drifted massive stars of the nine models with the observed isolated massive sources (see Table 4.1).

4.3.3 Comparison of the observed distribution of isolated high-mass stars with the model grids

4.3.3.1 The concept of the histogram difference

By constructing a grid of different models (see Sect. 4.3.2), we are interested in finding the most similar model to the observed population. To measure the deviation of the models from the observed data, histograms of the data and each model are constructed by calculating spatial distances of all the stars, including the Quintuplet members, to the center of the Arches cluster as a reference point. One way to quantify histogram differences is to use the number count difference in each bin, which is equivalent to calculating the classic Euclidean distance between the feature vectors[3] of two distributions. The square of the classic Euclidean distance of two N-dimensional vectors $\mathbf{P}$ and $\mathbf{Q}$ is defined as follows:

$$D^2_{euclid}(\mathbf{P},\mathbf{Q}) = (\mathbf{P}-\mathbf{Q})\cdot(\mathbf{P}-\mathbf{Q})^T = \sum_{i=1}^{N}(p_i - q_i)^2.$$

Consider the three different sample spatial distributions illustrated in Fig.4.1, which are comparable representations of a background distribution with two toy-clusters with different cluster distances. The histograms of their distributions along the x-axis show peaks with similar height. Intuitively, we appraise the first two distributions to be more similar compared to the third. However, comparing the Euclidean distance between the feature vectors of each pair shows the same level of similarity with just one of the

[3] A feature vector is a vector for which the components of the vector represent properties of some data set. Here, constructed histograms represent the feature vectors of each distribution.

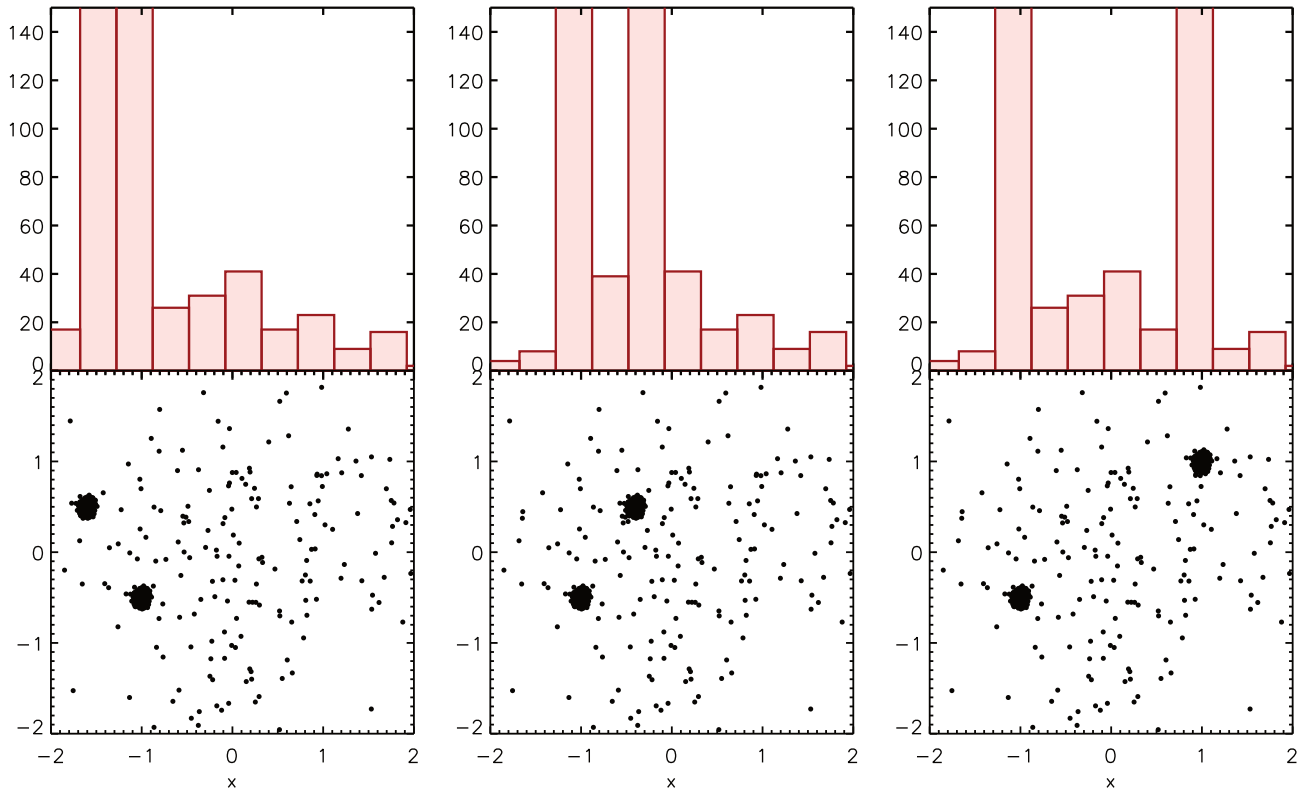

Figure 4.1: Three different artificial distributions are shown as examples, accompanied by the histograms of their distributions along the x-axis. The background population along with one of the over-densities are similar in the three plots. Comparing the difference in the number count of each bin alone is not indicative of the analogy, which is reflected in the similarity of adjacent bins.

major peaks shifted to another radial bin. The Euclidean distance assumes there is no relationship between individual components (number counts in each bin here) and does not reflect the similarity of the ith bin of the feature vector $\mathbf{P}$ to the $(i+1)$-th neighboring bin of the compared feature vector $\mathbf{Q}$. Therefore, the simple Euclidean distance, which is the difference of the count in each bin, is not appropriate for distributions, which exhibit correlations of the feature vector components. For example, more fully occupied bins might compensate less populated neighboring bins.

To overcome such a problem, Hafner et al. (1995) suggested a method for retrieval of images based on their color histograms using a quadratic distance measure. Assuming the N-dimensional distributions $\mathbf{P}$ and $\mathbf{Q}$, if $\mathbf{F} = \mathbf{P} - \mathbf{Q}$, the quadratic distance can be presented as: $D_Q^2(\mathbf{P}, \mathbf{Q}) = \mathbf{F^T A F}$. The matrix $A = [a_{ij}]$ is a weighting matrix, which allows for individual weighting of the cross-correlation between the bins i and j. Therefore, we can calculate the histogram difference, H_d, by cross-matching between different components:

$$H_d = D^2_{hist}(\mathbf{P}, \mathbf{Q}) = \mathbf{F^T A F} = \sum_{i,j}^{N} (p_i - q_i)(p_j - q_j) a_{ij}.$$

The histogram difference as a form of quadratic distance is successfully applied to compare color histograms of different multimedia databases (e.g., Ankerst, Kriegel & Seidl, 1998). Here, we adopt the idea presented by Hafner et al. (1995) to calculate the histogram difference, H_d, between various models and the observed data. Our applied weighting matrix is constructed as:

$$a_{ij} = exp(-\sigma d^2_{ij}),$$

where d_{ij} is the Euclidean distance between bins i and j and σ is a constant which, determines the shape of the weighting matrix (see Hafner et al. (1995) for details). This method allows us to consider the influence of neighboring bins on each other. Hence, the weighting matrix should increase the effect of cross-correlations between bins i and j as a function of distance between the two bins. This objective is fulfilled by choosing lower σ values to increase the non-diagonal entries of the weighting matrix, A. On the other hand, the weighting matrix $A = [a_{ij}]$ should generate a quadratic distance, H_d, which is nonnegative. This requirement demands for higher σ values. In our analysis, the positive semidefinite weighting matrix with relatively large non-diagonal entries is achieved with a σ value of 12.

The defined histogram difference, H_d, varies between 0 and ∞. Analogous to the Euclidean distance, the H_d value cannot be used to define the absolute "closeness" or in particular "similarity" in this context. Nevertheless, we can use it to compare distinct models and to find the most similar model to our observed reference data set by determining the relative "similarity".

4.3.3.2 Selection of the best-matching model

We compute the histogram difference, H_d, between the observed population of isolated massive stars in the GC and different models (see Sect. 4.3.2) with the aim of selecting the best-matching model. Table 4.1 lists models with different assumptions on the age of the Quintuplet cluster and on the initial masses of stars that are currently observed as WN, WC, or OB stars. The final feature vector of the spatial distribution for massive stars in each constructed model of both the Arches and Quintuplet clusters is compared to the observed data in the GC. Feature vectors of the models are constructed as histograms for the spatial distances of all the stars in the two clusters with reference to the center of the Arches cluster and the average of ten random realizations for each model. The feature vector of the observed population is likewise constructed as the histogram that contains the number of observed high-mass stars with respect to the center of the Arches cluster. To estimate the uncertainty in the histogram distance between the average model and the observations, the ten random realizations are also individually compared to the observed distribution. The calculated standard deviation of the resulting H_d values are reported for each model in Table 4.1. Since we are only

interested in the population of drifted or ejected stars, sources that lie inside the tidal radius ($\sim$ 1.6 pc; Habibi et al. 2013) of the Arches, Quintuplet, and Nuclear clusters are excluded from the data and the models. The bin size is chosen to be 3 pc to avoid random fluctuations. Our experiment shows that the final calculated H_d value is not very sensitive to the bin size, since our method accounts for the impact of neighboring bins on each particular bin. The model with an age of 5 Myr for the Quintuplet cluster and an initial mass of $40\,M_{\odot}$ for massive stars is found to have the lowest H_d value and is the most similar model to the observed distribution. We use this best-matching model for the comparison to the observations and further analysis.

4.4 Results

The Arches cluster moves rapidly through the high-density environment in the GC (e.g., Stolte et al. (2008a)). As the cluster moves along its orbit, two-body relaxation in the cluster accelerates some stars to exceed the escape velocity, which is variable and determined by the tidal force. These stars either take over the cluster center or fall behind depending on their differential velocities. This known phenomenon populates the two extended tidal arms. In this section, we present the comparison of the massive stars outside the Arches and Quintuplet clusters in the best-matching model, which mostly belongs to the tidal arms, with the observed massive sources in isolation (Mauerhan et al., 2010a). In Sect. 4.4.1, simulations are compared to the data in terms of the number of isolated sources and their spatial distribution. In Sect. 4.4.4, the velocity variation along the tidal structures are analyzed to obtain a general picture of dynamical evolution of the cluster as it moves along its orbit.

4.4.1 The spatial distribution of drifted and observed high-mass stars

The best-matching model of massive sources outside the Arches and Quintuplet clusters assumes an age of $5Myr$ for the Quintuplet cluster and $M > 40\,M_{\odot}$ for WR progenitors. Figure 4.2 demonstrates the projection of one of the realizations of the best-matching model on the plane of the sky. In this model, each tidal arm of the Arches cluster extends out to 20 pc along the Galactic plane, whereas tidal arms of the Quintuplet cluster stretch out to 65 pc. Massive stars in both clusters, $M > 40M\odot$, are mostly concentrated around the cluster center. Mass segregation of the Arches cluster has been observationally confirmed, since the observed slope of the mass function increases with radius (Espinoza, Selman & Melnick 2009, Habibi et al. 2013). Observations of the high-mass part of the mass spectrum of the Arches cluster ($M >\sim 10M_{\odot}$) out to its tidal radius revealed a depletion of massive stars in the cluster outskirts (Habibi et al., 2013). In our previous study, we derived a present-day mass function slope of -3.21 ± 0.30 in the outer annulus ($0.4 < r < 1.5$ pc) as compared to a flat slope of -1.50 ± 0.35 in the core ($r < 0.2$ pc), where the Salpeter slope is -2.3. The Quintuplet cluster exhibits a density that is about 100 times lower in the core compared to the Arches cluster (Figer 2008). The present-day mass function of the Quintuplet cluster is also characterized by a flat slope, -1.68 ± 0.1 (Hußmann et al., 2012). Apart from

Table 4.1: Calculated histogram difference, H_d, between the observed isolated massive sources by Mauerhan et al. (2010a) and different models. Compared models assume an age of 4, 4.5, and 5 Myr for the Quintuplet cluster and 2.5 Myr for the Arches. The initial mass for the massive stars is considered to be 20, 40, and 60 $M_\odot$ in these models. The model, which assumes an age of 5 Myr for the Quintuplet cluster and an initial mass of 40 $M_\odot$ for WR progenitors, is found to have the lowest H_d and is the most similar model to the observed distribution. The standard deviations for the H_d values are derived by individual comparison of the ten random realizations of each model.

	H_d					
	WR-L=20$M_\odot$	StdDev	WR-L=40 $M_\odot$	StdDev	WR-L=60 $M_\odot$	StdDev
Q_{age}=4 Myr	17.4	$\sigma_{4,20} = 4.38$	4.48	$\sigma_{4,40} = 1.43$	6.38	$\sigma_{4,60} = 1.03$
Q_{age}=4.5 Myr	26.55	$\sigma_{4.5,20} = 6.93$	5.96	$\sigma_{4.5,40} = 1.15$	5.63	$\sigma_{4.5,60} = 0.88$
Q_{age}=5.0 Myr	11.69	$\sigma_{5,20} = 1.79$	**3.784**	$\sigma_{5,40} = 0.75$	7.25	$\sigma_{5,60} = 0.81$

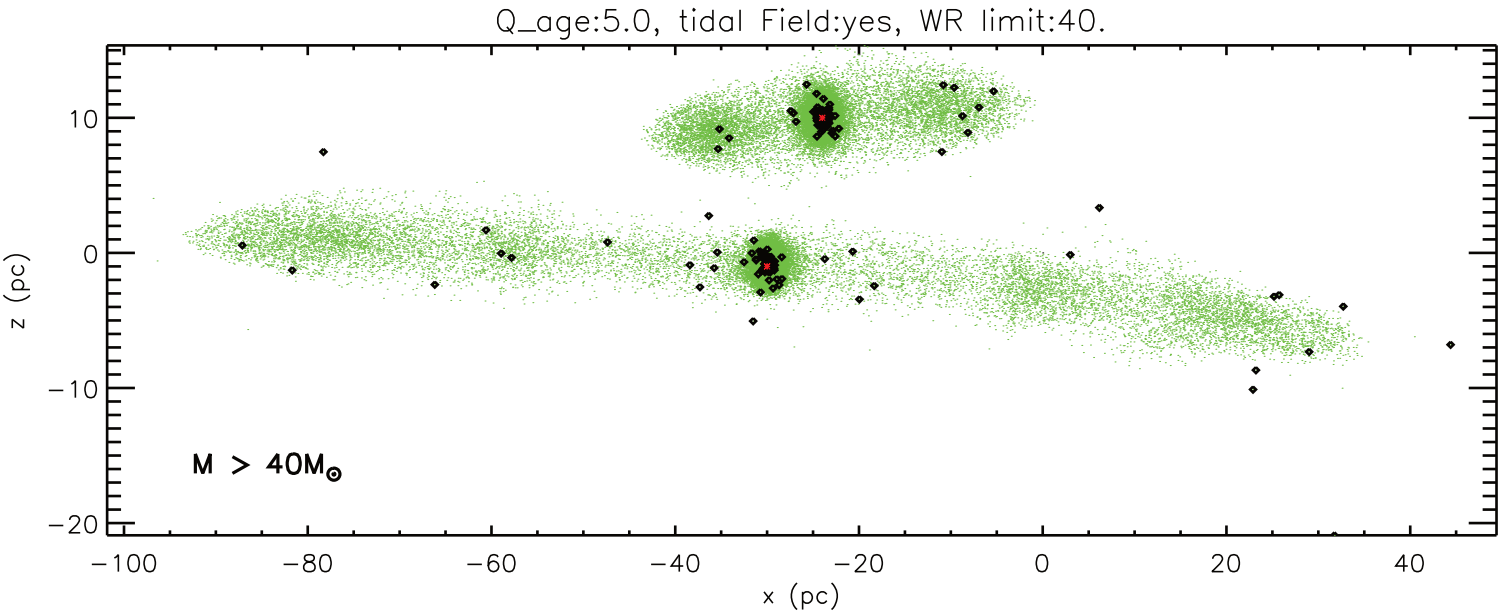

Figure 4.2: One realization of the best-matching model is projected on the plane of the sky. Green dots represent the cluster members. Sources with initial masses exceeding $40\,M_{\odot}$ are illustrated by filled diamonds. The x-axis is along the Galactic plane, and the z-axis is toward the Galactic north pole.

the high-mass stars in the cluster centers, Fig. 4.2 illustrates that in the models the majority of massive sources outside the cluster centers are also located along the tidal arms while the tidal arms are mostly constructed from low and intermediate mass stars.

A contour density map , which is built from the same realization of the best-matching model, is shown in Figure 4.3 along with the population of observed isolated massive stars. These sources fill two stripes along the Galactic plane with a distinct gap in the separation space between the two clusters along the direction of the galactic poles. The observed configuration is closely reproduced in the model by the location of the tidal arms of the two clusters. In Fig.4.3, the Nuclear cluster is located at the origin, (0,0). As the minor contribution of the Nuclear cluster was justified in Sect. 4.3.2, our models do not include the Nuclear cluster.

A group of observed isolated massive stars is located outside the Paα survey area around $x \sim -80\,$pc in Figure 4.3. These stars along with more X-ray emitting sources, are thought to be associated with the Sagittarius B molecular cloud complex (Mauerhan et al., 2010b). Figure 4.3 illustrates that the tidal arms of the Quintuplet cluster might extend out to the Sagittarius B region and therefore the observed evolved massive stars in this region might originate from the tidally drifted structures of the Quintuplet cluster.

The predicted number of massive stars based on the full set of ten different random realizations of each model is presented in Table 4.3. The models with an initial mass of $20\,M_{\odot}$ for WR progenitors overpredict the expected number of WR stars, which should

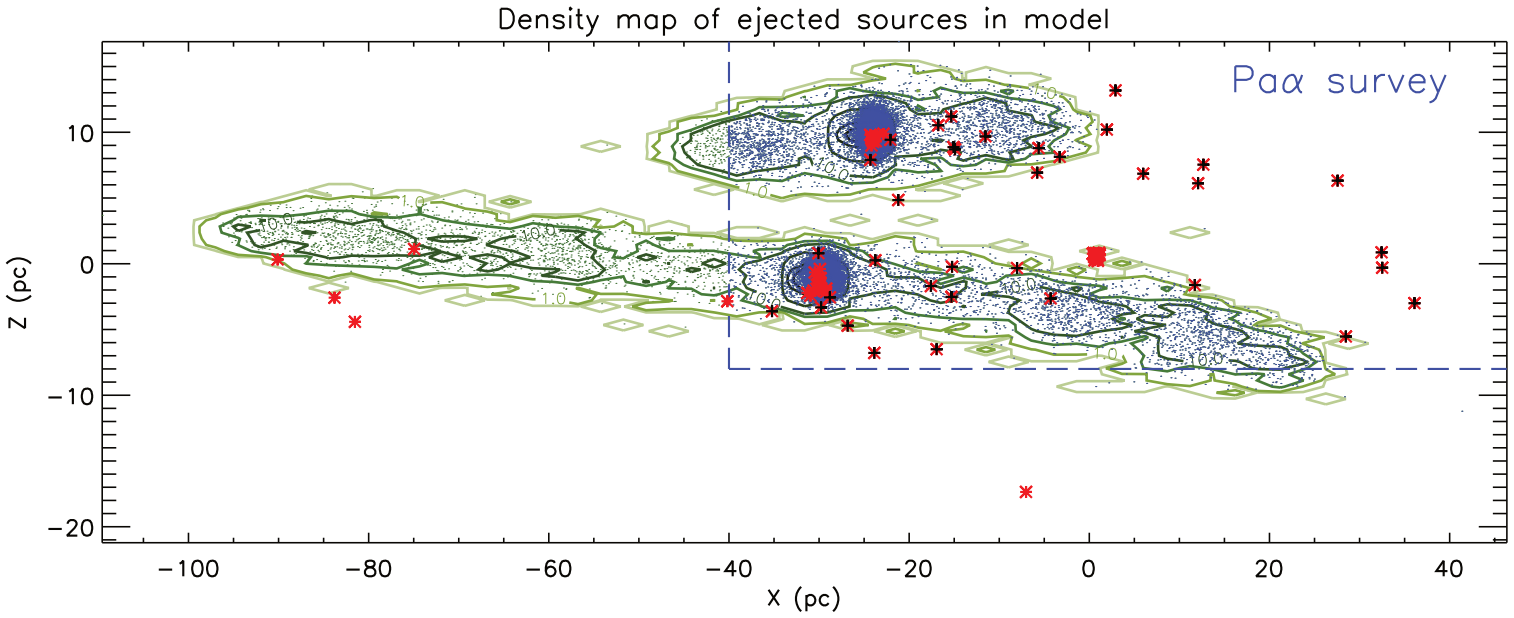

Figure 4.3: The contour density map for one of the realizations of the best-matching model with an age of 2.5 and 5 Myr for the Arches and Quintuplet clusters, respectively, and an initial mass of 40 $M_\odot$ for massive stars is presented with different shades of green lines. Darker colors indicate higher densities. The isolated massive stars observed by Mauerhan et al. (2010a) are marked with red asterisks. The dashed lines approximately represent the border of the Paα survey. This line separates the region where we perform our comparison between the model and the data. We include some of the observed sources outside the Paα survey area for illustration. Only the observed sources, as shown by red asterisks, which are marked with black crosses are used to compare observations to the models. Blue (green) dots represent the simulated cluster members, which are included (excluded) for the comparison analysis. The x-axis is along the Galactic plane, and the z-axis is toward the Galactic north pole.

have been detected in the GC region, while $M > 60\,M_\odot$ provides too few sources to represent the observed population. As Table 4.3 shows, $M > 40\,M_\odot$ is likely the most realistic initial mass of the progenitor sources that evolve to the observed isolated high-mass population today. These models predict 22-30 isolated high-mass stars which cover a significant fraction of the 35 observed massive stars in the Paα survey region outside the three clusters (outside their approximate tidal radius) in the GC region.

4.4.2 Comparing the spatial distributions

Table 4.3 allows us to perform a comparison between the number of massive stars outside the clusters in the models and the observations, which are independent of their spatial distribution. To compare the spatial distribution of drifted sources in the models with the data, we use two different methods. In Sect. 4.4.2.1, we present the predicted

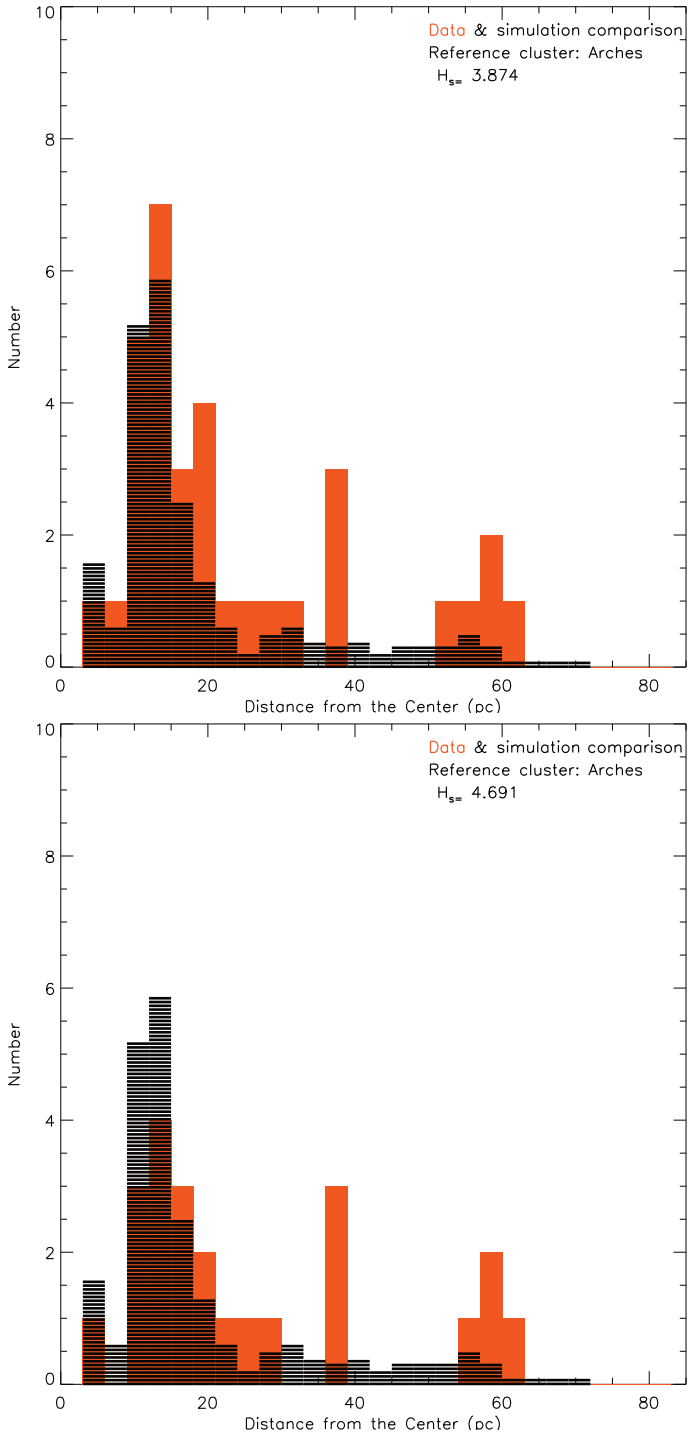

Figure 4.4: Line-filled histograms depict the average distribution of the massive sources, $M > 40\,M_{\odot}$, in the ten random realizations of the best-matching model. Stars within the central 1.6 pc of the simulated Arches and Quintuplet clusters are excluded. Red filled histograms illustrate the distribution of the observed massive sources. Distances are calculated with reference to the center of the Arches cluster. Observed sources, which lie in the central 1.6 pc of the three clusters, i. e. Arches, Quintuplet, and Nuclear cluster, are excluded from these histograms. The calculated histogram difference, H_d, measures the similarity of the two distributions. Up: The comparison is based on the full list of WR stars and OB supergiants presented by Mauerhan et al. (2010a). Down: OB super giants are excluded from the observed catalog and the comparison is based on the population of WRs in the region.

density map of massive stars based on our best-matching model. In Sect.4.4.2.2, the feature vector of simulated sources is constructed on the full set of ten different random realizations of the best-matching model (see Sect. 4.3.3.2) and is compared with the data.

4.4.2.1 The density map

We create a density map of the observed massive stars using Voronoi diagrams. Voronoi tessellations define a neighborhood for each star, the Voronoi cell, on the plane of the sky. Each cell contains one observed star and the set of points on the plane of the sky which are closest to the generating star of the cell. Employing Voronoi diagrams allows us to see the hidden spatial structure in the spread of the points. For example, a preferred orientation in the distribution of points reflects as oriented polygons (Aurenhammer & Klein, 2000).

Figure 4.5 illustrates the resulting density map. The density map shows two stripes of polygons formed beside the clusters and along the x-axis, which confirm the preferred orientation of the observed massive stars along the clusters' tidal tails. The colors of the cells in Fig. 4.5 are assigned by the calculated probability of observing one or more stars in each particular cell, according to our best-matching model. To calculate the probabilities, we count the average number of predicted modeled massive stars, $M > 40\,M_{\odot}$, in each Voronoi cell, for all the available random realizations of the model. The corresponding probabilities are accordingly calculated by assuming a Poisson distribution, $P(n \geq 1) = \sum_{i=1}^{\infty} P(n)$. The Poisson probability, $P(n) = \lambda^n e^{-\lambda}/n!$, yields the probability of observing n stars where the model predicts the mean value, λ, for the number of stars in each Voronoi cell.

Figure 4.5 illustrates that the area with a high probability of observing one or more stars is located at a distance of ~ 20 pc from the cluster centers. The regions, which contain the cluster central members are discarded from the probability calculations (see white regions in Fig. 4.5). The model predicts relatively high probabilities, $P(n \geq 1)$, along the tidal arms and specifically at the end of the arms. The end of the tidal arms are located at $(x \sim 0, y \sim 10)$ pc for the Arches cluster and $(x \sim 35, y \sim -7)$ pc for the Quintuplet cluster. Figure 4.5 also shows that 62% of the observed isolated massive stars, at least one of the ten random realizations of our model predicts a star that can explain the observed star. This number increases to 72% when we only consider the Voronoi cells within the central 20 pc from the center of the Arches cluster.

The areas of low probabilities are located in the upper right of Fig. 4.5, $10 \lesssim x \lesssim 40$, $0 \lesssim y \lesssim 10$ pc, and also in the region, which lies between the two clusters, $3 < y < 7$ pc. These are the sources which, according to our models, are less probable to originate in the tidal arms of the Arches and Quintuplet clusters. In Sect. 4.4.3, we discuss the possible alternative and parallel scenarios that may explain the origin of these sources. Computed probabilities to observe exactly one star, $P(n = 1)$, and to observe one or more stars, $P(n \geqslant 1)$ are presented in Table 4.2. It is important to notice that the maximum value of the Poisson probability for observing one star, $P(1) = \lambda e^{-\lambda}$, is $\sim 37\%$.

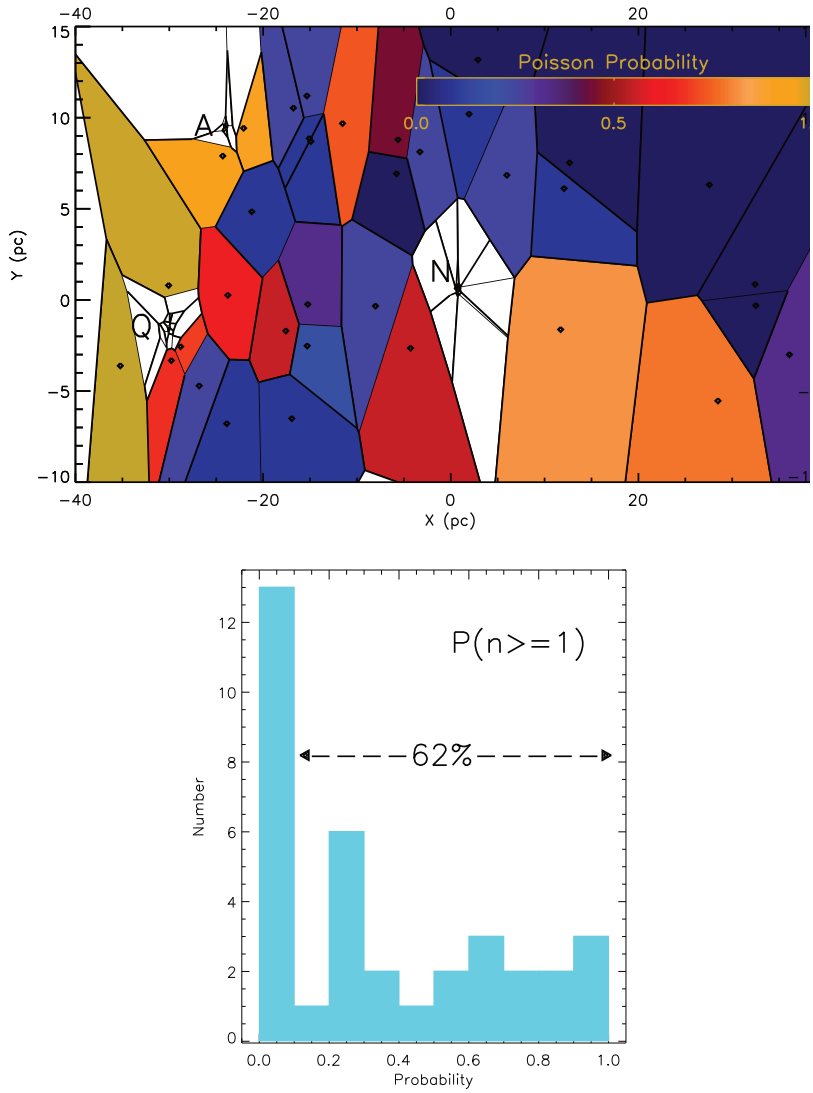

Figure 4.5: Up: The density map of the observed massive stars (Mauerhan et al., 2010a) is derived using Voronoi diagrams. The two stripes of polygons formed beside the clusters and along the x-axis confirm the preferred orientation of the observed massive stars. The Voronoi cells are colored according to their calculated Poisson probability of observing one or more stars in each cell, $P(n \geq 1)$, based on our best model. The color-bar assigns colors to the calculated probabilities. White regions contain the cluster central members and are discarded from the probability calculations. Down: The distribution of calculated Poisson probabilities, $P(n \geq 1)$, is shown. Our model reproduces at least one star in ten random realizations, $P(n \geq 1) > 10\%$, for 62% of the observed isolated massive stars. Please note that the Voronoi cells appear skewed due to different scales for the x and y axis.

4.4.2.2 Comparing feature vectors

Figure 4.4 illustrates histograms of distances of all the massive sources with reference to the center of the Arches cluster. It shows that our models produce drifted massive sources at a distance up to 70 pc from the Arches center. This result implies, that the possibility of being a run-away/drifted star especially from the Quintuplet cluster cannot be excluded for an observed isolated massive star at a distance up to 70 pc from the Arches center. The provided list by Mauerhan et al. (2010a) includes 11 WC and 13 WN stars with 1 LBV and 10 OB supergiants outside the 1.6 pc radius of the three clusters in the Paα survey region. The comparison of their full list in the Paα survey area to the model is shown in Fig. 4.4. The best-matching model reproduces 80% of the known isolated massive stars out to a distance of 21 pc and 67% of the observed population out to 80 pc from the center of the Arches cluster. However, since the population of OB supergiants is not complete in this catalog, we excluded all the OB stars from the original observed list and repeated the comparison. This comparison shows that our model produces 20% more massive sources as compared to the observed population of WN, WC, and LBV stars in the GC region out to a distance of 21 pc from the center of the Arches cluster (see Fig 4.4, right). This over-prediction may occur because we can only choose an initial stellar mass. We have no means to distinguish the spectral types of the stars in our models. Hence, stars, which are in the supergiant phase or even main sequence phase, are always partially included. It can also be due to a missing population of WC stars. The Paα line strength of both WN and WC stars span a similar range of $1.2 < F187/F190N < 2.9$ (Mauerhan et al., 2010a). The bright K_s counterparts of WN stars guarantees a near completeness of the WN sample in the GC. However, due to the faint end of the K_s brightness distribution of observed WC stars, their sample is probably not complete (see Mauerhan et al. (2010a) for details).

4.4.3 Alternative scenarios

In both histograms of Fig. 4.4, the major peak in the observed distribution of isolated massive stars at ~ 15 pc is well reproduced by the best-matching model. Nevertheless, the two minor peaks at distances of ~ 40 pc and ~ 60 pc from the Arches center are absent in the model. Out of the 35 observed massive sources, 27 stars are located close to the modeled tidal arms of either of the two clusters. The remaining eight sources are observed outside the modeled arms. These sources, which are not reproduced with our models can have different origins: Many high mass stars are expected to be in binaries with high-mass companions ($\sim 70\%$ of all O stars of which $\sim 40\%$ are expected to have evolved with strong interactions; Sana et al. 2012). The observed sources outside the tidal structures can originate in tight binary systems in which the primary has already exploded as a supernova (Blaauw (1961); Stone (1991)). Therefore, the secondary has received a kick and is ejected at a random direction and at a high relative velocity compared to the cluster orbital velocity. These ejecta are expected to have a high velocity compared to the velocity of the cluster center and can possibly explain the detected population in between the modeled tidal structures and the single detected

massive star at z=-18 pc (see Fig. 4.3). This process is especially expected from some of the most massive stars in the Quintuplet cluster at the suggested age of 4 to 5 Myr. Another possibility for their origin is that they are formed independently of the current observed clusters.

A possible Orion Nebula cluster (ONC)-type host star cluster, which owns ~ 1 massive source of $\sim 35\,M_{\odot}$ cannot be detected in the GC region with any of the current wide-field surveys. The density of such a star cluster is too low, and intermediate-mass sources ($M < 10\,M_{\odot}$) are too faint to stand out among the dense, crowding-limited GC field. These clusters are expected to dissolve even faster than the young sturburst clusters. The survival lifetime of less than 10 Myr suggests that they could appear too dispersed to be detected as a compact entity, such as in the Arches cluster (For discussion on dissolution time and detectability of the clusters in the GC, see Portegies Zwart et al. 2001a.). The other scenario is that these sources are formed in isolation from the dense molecular clouds observed in the central molecular zone (Longmore et al., 2012). The last two scenarios are currently hard to distinguish.

The discrepancies between the model and the data also can originate in limitations of our models. In the absence of precise 3D velocity measurements for the Quintuplet cluster[4], our models assume that the Quintuplet cluster is an older representation of the Arches cluster. Although this assumption is based on the observed density and age of the Quintuplet cluster, a more accurate measurement of the 3D velocity of the Quintuplet cluster, will eventually help in choosing the best matching orbit for the Quintuplet. Employing different orbits can shift the position of the tidal tails on the plane of the sky. We expect that our experiment that assumes three different ages for the Quintuplet cluster partly covers the effect of uncertain orbit of the Quintuplet cluster. The other limitation of the models is the lack of primordial binaries. Although wide binaries form automatically in the models in the early stages of cluster evolution, the population of tight initial binaries is missing in these simulations. These binaries play an important role in dynamical three or four-body encounters, which produce ejected stars (e.g., Poveda, Ruiz & Allen (1967); Gies & Bolton 1986). Adding primordial binaries to these models produce more massive sources outside the tidal radius of the clusters and strengthen the similarity of the models with the data. These sources are less likely to be spatially confined to the tidal arms of the cluster, yet the effect of the GC tidal field on these high-velocity ejected sources needs a thorough investigation in future studies.

In summary, the dynamical model of the Arches and Quintuplet clusters, which assumes an initial mass of $40\,M_{\odot}$ for the WR star progenitors and a Quintuplet age of 5 Myr, can explain up to 80% of the observed isolated population of massive stars.

[4] The preliminary analysis of the proper motion data of the Quintuplet cluster yields $167 \pm 15, \mathrm{kms}^{-1}$ (Stolte et al., 2014a), which is similar to the measured value of $172 \pm 15\,\mathrm{kms}^{-1}$ for the Arches cluster (Clarkson et al., 2012). Given the close projected distance between the Arches and Quintuplet clusters in the GC region, we hence use the Arches orbit to simulate the Quintuplet cluster.

4.4.4 The velocity distribution of drifted cluster members

Tidal arms form as a result of differential velocities produced by the many body dynamical interactions between stars in the cluster. Since the cluster moves along its orbit, this velocity difference causes stars to either fall behind or take over the cluster center. Figure 4.6 illustrates the velocity variation in the Arches (top panel) and the Quintuplet clusters (bottom panel). The velocity variation of the stars in the tidal arms reaches 50 $\mathrm{km\,s^{-1}}$ for the Arches cluster and 140 $\mathrm{km\,s^{-1}}$ for the Quintuplet cluster. The distribution of the massive stars, $M > 40\,M_{\odot}$, in Fig. 4.7 shows that there are sources with masses of up to $100\,M_{\odot}$ in the furthest extent of the tidal tails, despite that most of the massive stars sink to the cluster core. For example in the illustrated model in Fig. 4.7, a $100\,M_{\odot}$ star is found at the distance of $\sim 15\,\mathrm{pc}$ from the Arches and $\sim 60\,\mathrm{pc}$ from the Quintuplet center. Most of the massive sources, which are outside the central tidal region have velocities similar to the tidally diffused population around them. The few massive sources that lie outside the tidal structure have velocities similar to the extreme velocities of stars in the tidal arms. To study the mechanism allowing the sources to drift out of the cluster in more detail, we analyze the trajectories of the sources in different mass ranges and compare them to the position of the cluster on its orbit around the GC. Stolte et al. (2008b) showed that the Arches cluster evolves along an open eccentric rosetta-like orbit (see Fig. 4.9(a) and 4.10(a)). Figure 4.8(a) demonstrates the variation of Galactocentric distance of the cluster over time. As the cluster moves along its orbit, it encounters a spatially varying tidal field caused by the GC potential and its asymmetric orbit. The corresponding pericenters and the apocenters[5] on each period are indicated in Figures 4.8 and 4.9(a). The projected orbit of the cluster in the xy-plane, which is close to the orbital plane of the modeled cluster, is indicated in Figure 4.9(a); the projected snapshots of the cluster at apsides are illustrated in Fig. 4.9(b), which allow us to follow the spatial spread and the velocity variation of the cluster along its orbit without being biased by the projection of the cluster on the plane of the sky, the xz-plane.

Following the pericenters and the apocenters on the orbit, we can trace the trajectory of the cluster members with respect to the cluster center (see Fig. 4.8). Both groups of massive stars, $M > 40 M\odot$, and stars with intermediate masses, $10 M_{\odot} < M < 20\,M_{\odot}$, follow a similar pattern (Figures 4.8(b) and 4.8(c)). Our finding that velocities of the simulated massive sources are in the range of the velocity variation along the tidal arms shows, that high-mass and intermediate-mass stars outside the tidal radius of the cluster gain energy through similar physical processes. Some of the stars gain energy in the center of the cluster probably through two-body relaxation. Afterward, as these sources recede from the cluster center, they undergo several periods where they slightly fall toward the cluster and are followed by pulling away from the cluster center. During the time that the cluster moves away from the apocenter toward pericenter, its velocity increases, and consequently, individual orbits of stars on the

[5] As the cluster is not on an elliptical eccentric orbit, we use the word pericenter (apocenter) only to refer to the point of closest (furthest) approach to the center of the potential on each orbit. The position of these points are different for each period.

tidal structures diverge spatially. This effect is indicated in Fig. 4.8, as the sources recede from the cluster center after the apocenter passage. The projected snapshots of the cluster on the xy-plane that is close to the orbital plane of the cluster illustrate the expansion of the cluster, including its tidal arms, after passing the apocenter and accelerating toward pericenter (see Fig. 4.9(b); compare the snapshots of the cluster on each pericenter to its snapshot at its previous apocenter). Comparably, when the cluster approaches the apocenter and decelerates, stars on the tidal tails contract toward the cluster center (see Figure 4.8), and the cluster appears less expanded (see Fig. 4.9(a)). A similar behavior is discussed in studies that investigate halo globular clusters and their interaction with the Galactic field through several Gyrs of evolution (e.g., Küpper et al. (2010)). We have calculated the surface mass density inside a cylinder of 0.5 pc at the center of the cluster and perpendicular to the plane of the sky, as it can be investigated by observations. The surface mass density of the central region of the cluster declines as the cluster expands on its orbit (see Fig. 4.8(d)).

Although snapshots of the cluster along the xy-plane and close to the orbital plane of the cluster follow the dynamical evolution of the cluster, the observed cluster is affected by the projection of the cluster on the plane of the sky. In Fig. 4.10, we illustrate the projected orbit of the modeled cluster around the GC on the plane of the sky, the xz-plane. As the cluster moves along the 3D orbit, it passes through apsides. These apsides are marked on the orbit with the projected snapshot of the cluster at the corresponding apside point. Comparing Fig. 4.10(b) with Fig. 4.9(b) shows the strong effect of the projection. For example, the snapshot of the cluster at the age of 3 Myr appears squished on the plane of the sky (see Fig. 4.10(b)), while comparing this snapshot to its projected snapshot on the xy-plane (Fig. 4.10(b)) reveals that the cluster is physically expanded at this location. The same effect is observed for some of our analyzed models. Figure 4.9(a) shows that at the age of 4.5 Myr the cluster is located in the middle of its two apside points; hence, it is physically expanded. However, it appears squished on the plane of the sky. The effect of projection causes the massive stars in the tidal arms of the cluster to spread over a much smaller area on the plane of the sky. Models with $20M_{\odot}$ and $40M_{\odot}$ as an initial mass of a WR progenitor star produce an adequate number of massive stars in the model (see Table 4.3), which gives us better statistics, so that we can see this effect reflects in the H_d values of models. For these models, the calculated H_d values is higher age of 4.5 Myr for the Quintuplet cluster (see Table 4.1).

In summary, the models suggest that high-mass stars drift out of the clusters with the same physical mechanisms as intermediate-mass stars that form the tidal tails. Hence, their velocity is similar to the tail stars, and their location is consistent with the spatial distribution of the "isolated" WR stars close to the simulated location of the tidal tails. Figures 4.8(b) and 4.8(c) show that the drift pattern of high-mass stars over time is very similar to the drift pattern of intermediate mass stars. They follow the same apo/pericenter variation and are not rapid ejectors in these models. The clusters expand rapidly after 3 Myr, so that tidal tails stretch out over 120 pc across the central molecular zone within 5 Myr (see Fig. 4.10(b) and Fig. 4.9(b)), which is close to its entire diameter ($\sim$ 120 pc). According to these models, it is therefore not surprising

anymore to find isolated high-mass stars at large distances from the location of the clusters today as they drift along the tidal arms; that is, they are expected to occupy the entire area where the tidal structures stretch out.

4.5 Conclusions

In this study, we present N-body simulations of the Arches cluster to create combined models of the Arches and Quintuplet clusters. The population of ejected and drifted sources from the two clusters is compared to the HST/NICMOS Paschen-α (Paα) survey of the Galactic center, which detects the distribution of young massive stars in the GC region (Mauerhan et al., 2010a). Our study can be summarized as follows:

1. We construct different combined models of massive sources outside the Arches and Quintuplet clusters by assuming different ages for the Quintuplet cluster and distinct values for the initial mass of a WR progenitor (see Table 4.1). We compare these models to the observed population of massive stars presented by Mauerhan et al. (2010a) by employing a method, which calculates the histogram difference between spatial distributions of stars. Among all the constructed models, the model, which assumes an age of 5 Myr for the Quintuplet and an initial mass of $40 M_{\odot}$ for a WR progenitor, is the most similar to the spatial distribution of the observed isolated high-mass stars.

2. The strong tidal field of the GC potential results in extended tidal arms for both the Arches and Quintuplet clusters at their current age. In the best-matching model, tidal arms of the Arches cluster stretch out to 20 pc in each direction on the plane of the sky and along the Galactic plane, while the tidal arms of the Quintuplet cluster extend out to 65 pc. The observations of massive stars in the GC region (Mauerhan et al., 2010a) reveal two strips along the Galactic plane with a prominent gap along the direction of the galactic poles. The projected positions of the tidal structures of the two clusters closely reproduce this observed distribution (see Fig. 4.3).

3. The observed massive sources outside the three clusters, including the young Nuclear cluster in the Paα survey area, is compared to the models using two different methods. First, comparing histograms of the spatial distributions of observed and simulated stars shows that the best-matching model reproduces 80% of the observed population out to 21 pc and 67% of the observed population out to 80 pc distance with reference to the center of the Arches cluster. Second, we create a density map of observed isolated massive stars using Voronoi diagrams. The constructed density map allows us to probe the probability of observing one or more stars in each Voronoi cell by assuming our best-matching model. For 62% of the observed isolated massive stars, at least one of the ten random realizations of our model predicts a star that can explain the observed star. This number increases to 72% when we only consider the Voronoi cells within the central 20 pc from the center of the Arches cluster. The sources that cannot be explained as

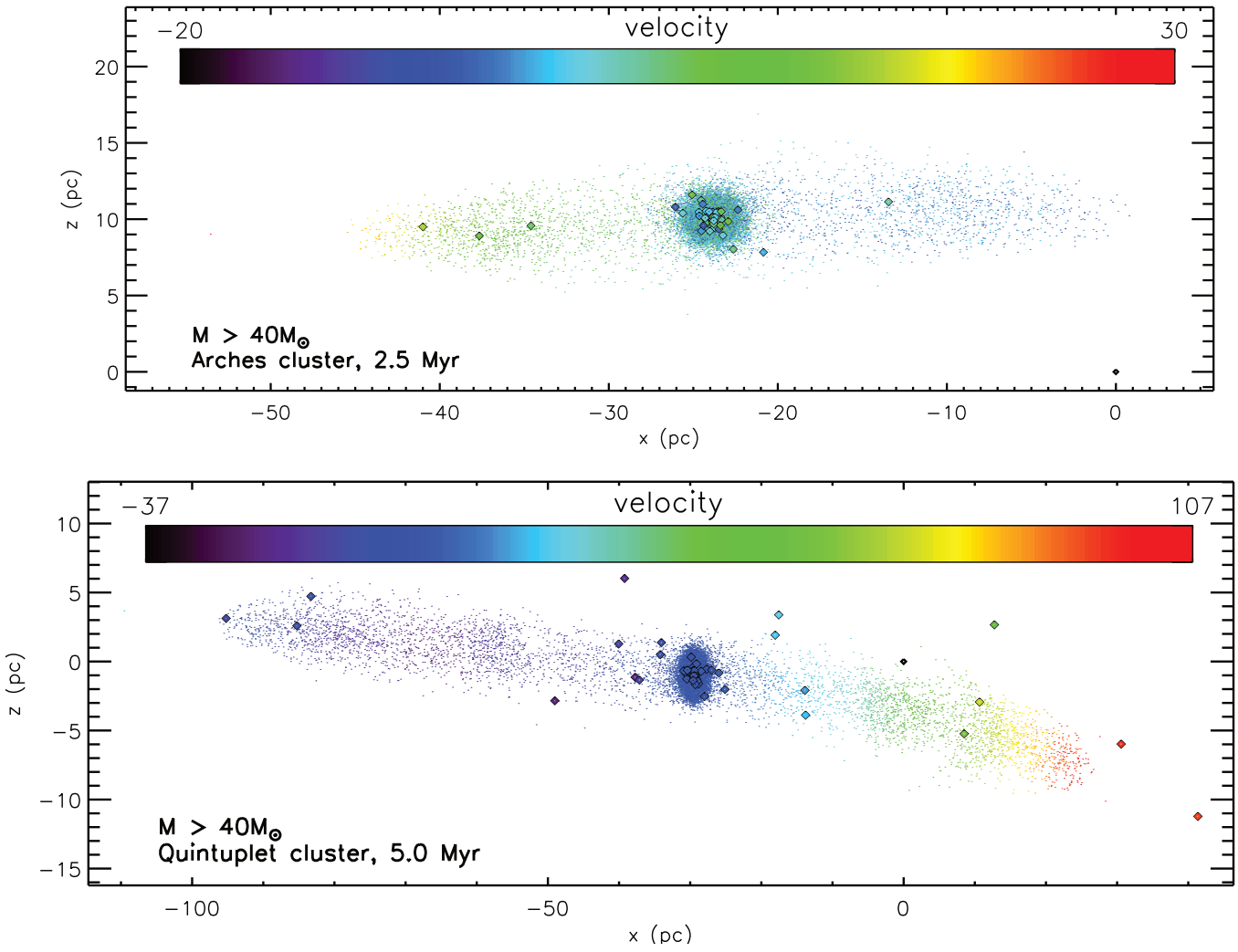

Figure 4.6: Velocity variation within the tidal arms for one realization of the simulated cluster at an age of 2.5 Myr (up) and 5 Myr (down). Massive stars, $M > 40M\odot$, are illustrated with larger symbols. Cluster members are color coded according to their velocities along the Galactic plane, V_x.

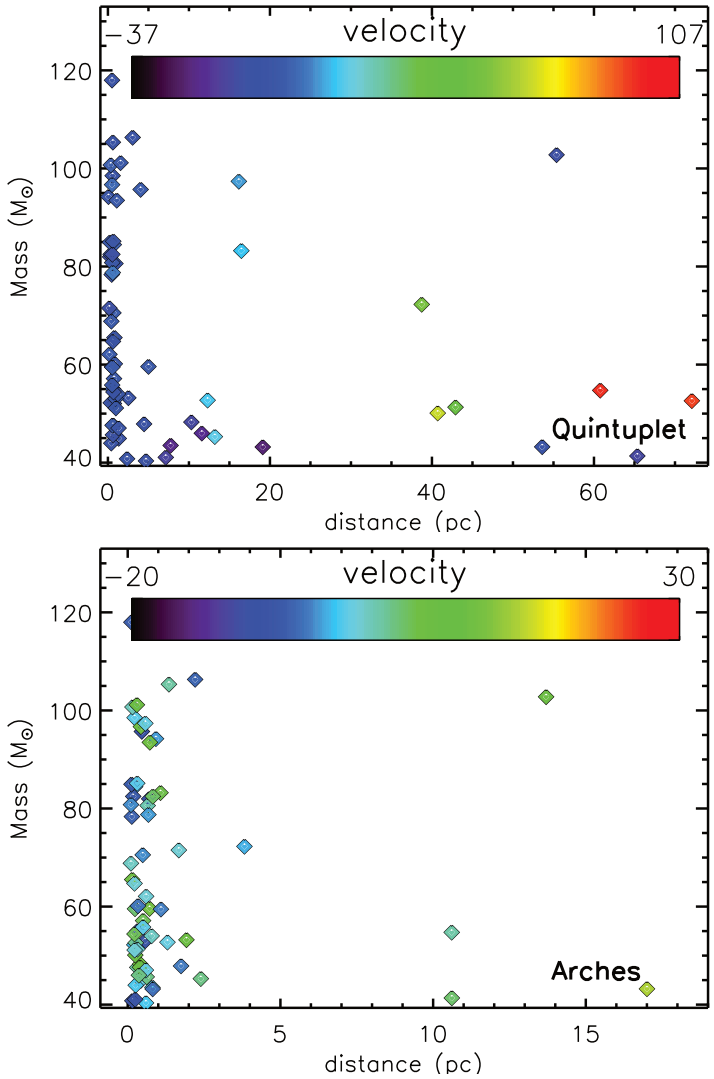

Figure 4.7: Initial masses are plotted over the distance from the cluster center for the massive stars, $M > 40M\odot$. Stars are color coded according to their velocities along the Galactic plane, V_x. Plotted populations are for one of the realizations of the model.

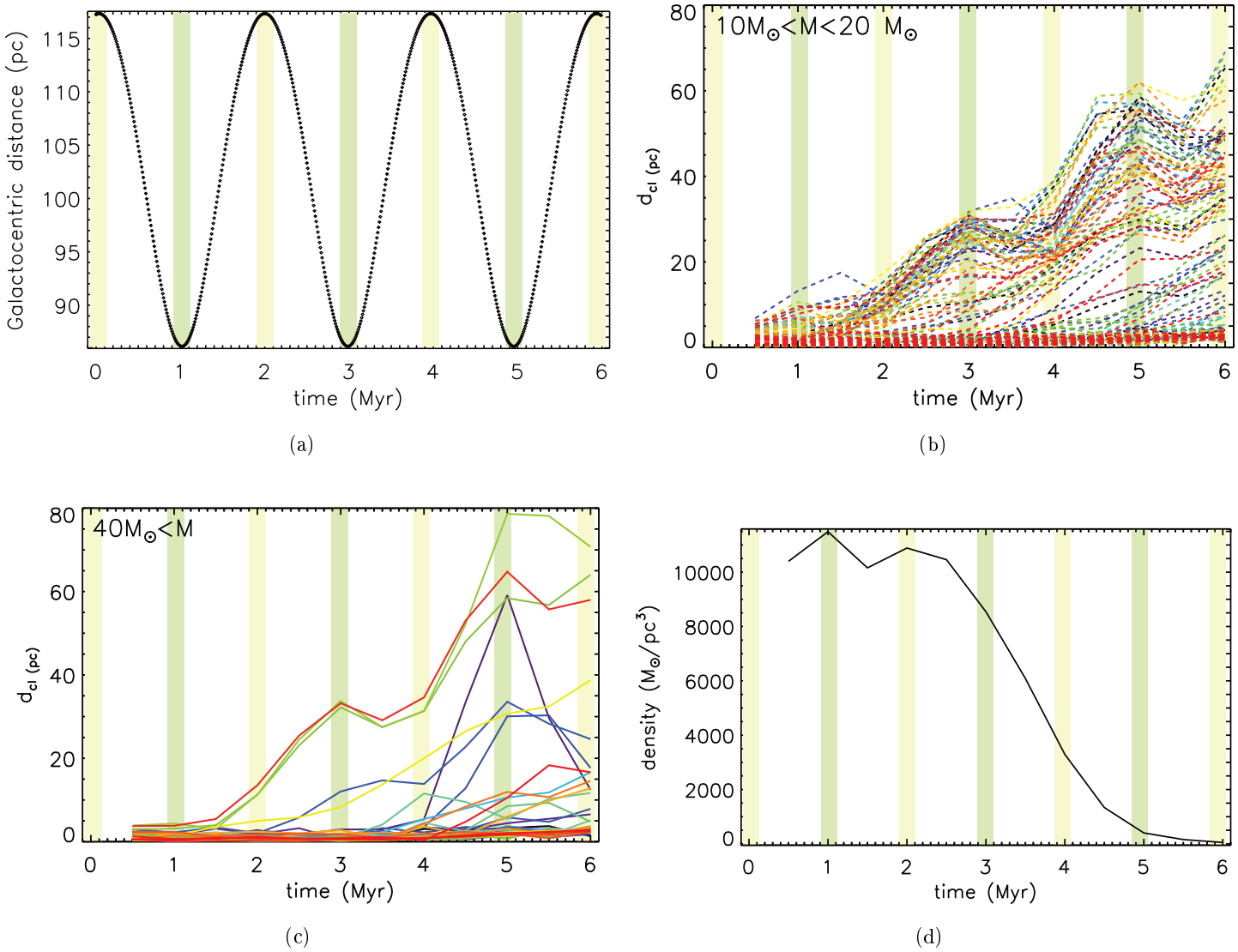

Figure 4.8: (a): The projected galactocentric distance of the cluster on the plane of the sky (x,z) is plotted over time. As the cluster moves along its open eccentric orbit, it encounters the variable tidal field caused by the GC. In Figures (a) to (d) regions of maximum and minimum Galactocentric distances are marked with yellow and green boxes respectively. (b, c): The projected distance of stars on the plane of the sky with reference to the cluster's center, d_{cl}, is plotted over time. Each line represents a trajectory of one star and colors are different to better distinguish lines. Trajectories of the cluster members are illustrated for the two mass ranges of $10_{M\odot} < M < 20\,M_{\odot}$ and $M > 40\,M_{\odot}$ in Figures (b) and (c) respectively. (d): The surface mass density of the center of the cluster is plotted over time. The density is calculated for a cylinder of 0.5 pc perpendicular to the plane of the sky.

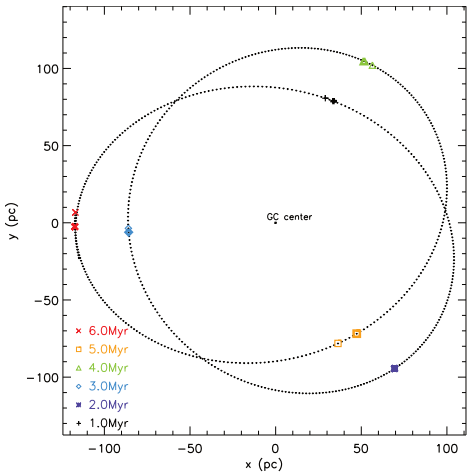

(a)

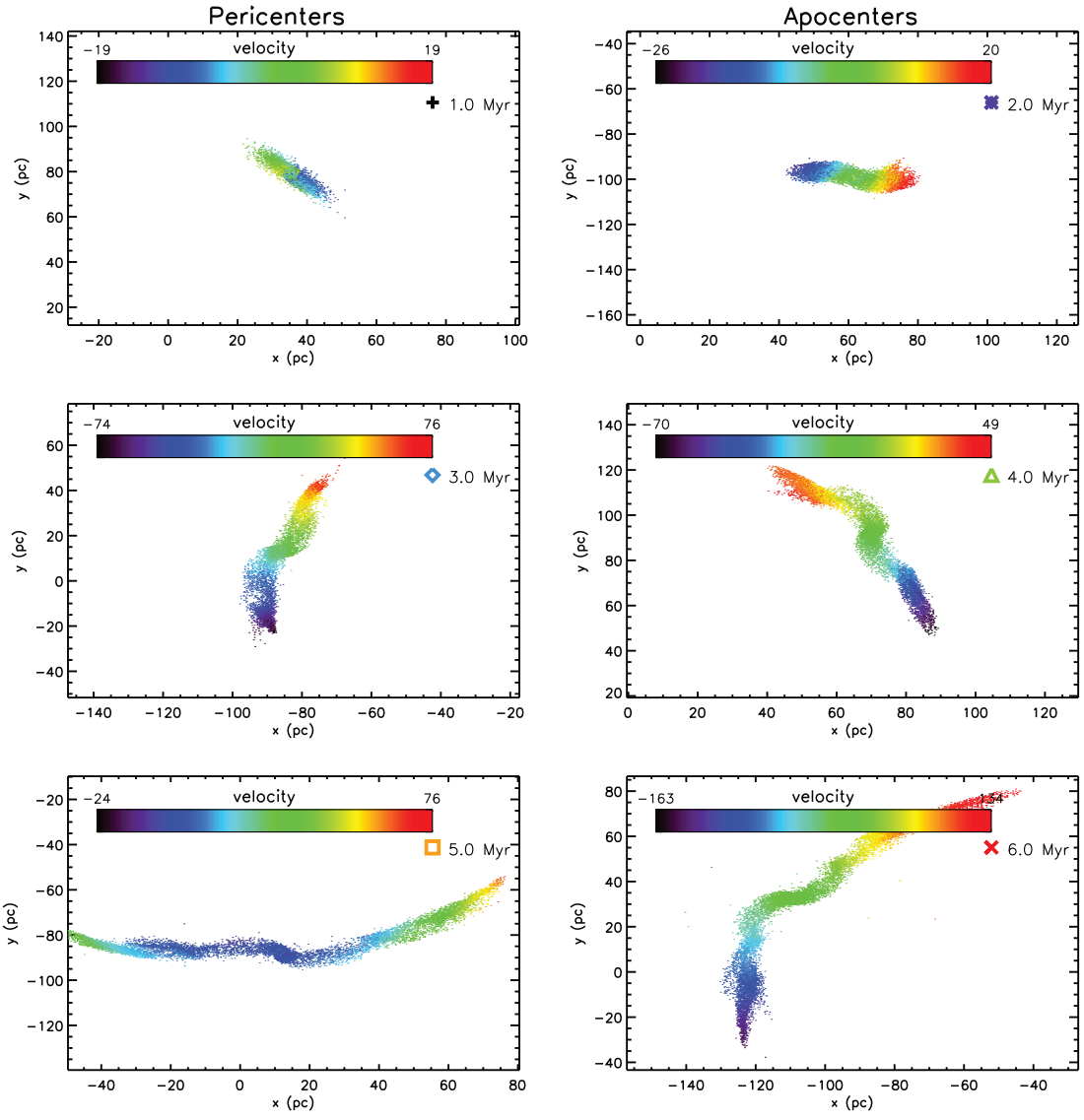

(b)

Figure 4.9: (Caption in the next page)

Figure 4.9: (From previous page) (a) The projected orbit of the cluster on the xy-plane, which is close to the cluster's orbital plane, is illustrated. The symbols on the orbit mark the apsides of the 3D orbit. Each symbol/color corresponds to a particular age. The thick symbols mark the exact position of the apsides, while the thin symbols refer to the closest available snapshot of the simulated cluster by considering the time resolution of the simulations. (b) The projected snapshots of the cluster on the xy-plane are shown at apocenters and pericenters. Each snapshot corresponds to one marked apside on the projected orbit. The sources are colored based on the present velocity variation in the cluster and its tidal tails.

originating from the Arches and Quintuplet are located at large distances from the tidal tails. On the other hand, the best-matching model predicts 20% more massive stars outside the clusters, when we perform the comparison between the best-matching model and the list of observed WR stars only, which excludes the less complete sample of OB sources (see Fig 4.4).

4. The best-matching model predicts 26 massive stars outside the clusters, as compared to the 35 observed massive stars outside the three clusters in the Paα survey region. According to our best-matching models, the majority of the simulated massive sources are located close to the tidal structure of the clusters, while the list of 35 observed massive stars includes 27 sources close to the tidal arms and 8 sources, which are not close to the tidal structure of the Arches and the Quintuplet cluster. Histograms of the spatial distribution of the observed sources display a major characteristic peak at $\sim 15\,\mathrm{pc}$ from the center of the Arches cluster. This peak is well reproduced in the best-matching model (see Fig. 4.4). However, two minor peaks at the distances of $\sim 40\,\mathrm{pc}$ and $\sim 60\,\mathrm{pc}$ from the Arches center are absent in the model. Possible origins of these sources are supernova kicks or dynamical ejections involving tight initial binary systems. In this case, these additional WR stars could also have emerged from the Arches and Quintuplet clusters. Currently, we cannot also exclude the possibility that these high-mass stars might have formed in smaller clusters or in isolation. Finally, a deviation, especially in the orbit of the Quintuplet cluster, could also give rise to the remaining differences between the observed and the simulated spatial distribution of high-mass stars in the GC.

5. According to our models, the projected tidal arms of the Quintuplet cluster at the age of 5 Myr extends out to 60 pc and reaches to the Sagittarius B2 region. This implies that the evolved massive stars observed in projection toward this region might originate in the tidally drifted sources from the Quintuplet cluster.

6. The tidal structure of both clusters form as a result of velocity variation in the cluster. The velocity variation along the tidal arms of the Arches cluster reaches $50\,\mathrm{km\,s^{-1}}$. This value is as high as 140 $\mathrm{km\,s^{-1}}$ for the Quintuplet cluster, which is detectable in a proper motion diagram of high precision astrometric studies of

the Quintuplet cluster.

7. The trajectories of the sources in different mass ranges in our models show that the tidal drifting of the cluster stars by the GC potential is an effective process, which causes the stars to recede out to 70 pc from the center of the Arches cluster. Both massive, $M > 40\,M_{\odot}$, and intermediate mass stars, $10M_{\odot} < M < 20\,M_{\odot}$, follow a similar pattern; they gain energy in the center of the cluster, which causes these sources to exceed the cluster's escape velocity. This suggests that the massive and intermediate-mass stars are evolved from the clusters by the same dynamical processes into tidal tails. The extended radial coverage of the high-mass stars inside the tidal tails implies that up to 80% of the isolated observed WR population can be explained by cluster stars.

Table 4.2: Positions and spectral types of the observed isolated massive sources in the GC region within the area covered by the Paα survey. From left to right, the columns are as follows: Sequential ID for stars, R.A., Dec., spectral type, and the reference study (a). The last two columns of the table present the Poisson distribution, $P(n) = \lambda^n e^{-\lambda}/n!$, of an observing one star, $P(1)$, and one or more stars, $P(n \geq 1) = \sum_{i=1}^{\infty} P(n)$, in the assigned Voronoi cell of each particular star on the density map of the observed isolated massive stars illustrated in Fig. 4.5. It is important to notice that the maximum value of the Poisson probability of observing one star, $P(1) = \lambda e^{-\lambda}$, is $\sim 37\%$.

ID	*R.A.* (deg, J2000)	*Dec.* (deg, J2000)	Spectral type	references	P(1)	P(≥1)
1	266.2797	-29.199789	WC	1	0.000	0.000
2	266.34123	-29.199841	WC	1	0.335	0.777
3	266.29086	-29.236897	WC	1	0.268	0.330
4	266.35067	-29.01608	OB	1	0.222	0.259
5	266.38129	-28.954669	OB	1	0.222	0.259
6	266.38549	-29.082757	WC	1	0.311	0.817
7	266.42203	-28.863311	OIf	1	0.222	0.259
8	266.42639	-28.879828	OB	1	0.090	0.095
9	266.47251	-28.827035	WN	1	0.193	0.926
10	266.50699	-28.920983	OI	1	0.164	0.181
11	266.51091	-28.903941	WC	1	0.359	0.551
12	266.54181	-28.925694	WN	1	0.090	0.095
13	266.57324	-28.884391	WN	1	0.090	0.095
14	266.59932	-28.803129	WN	1	0.002	1.000
15	266.54652	-28.818221	WN	1	0.031	0.994
16	266.4607	-28.957282	WC	1	0.222	0.259
17	266.52344	-28.858866	LBV	1	0.368	0.632
18	266.26195	-29.14986	OB	2	0.000	0.000
19	266.28733	-29.20495	WN	2	0.000	0.000
20	266.31744	-29.0543	WN	2,4	0.000	0.000
21	266.31969	-28.97364	WN	2	0.000	0.000
22	266.32974	-29.05609	WC	2	0.090	0.095
23	266.34453	-28.97895	WN	2	0.090	0.095
24	266.38652	-28.93797	OI	2	0.329	0.451
25	266.40056	-28.94405	WN	2	0.000	0.000
26	266.40538	-28.89827	OB	2	0.354	0.727
27	266.48067	-28.85738	WN	2,3	0.090	0.095
28	266.57119	-28.85871	Of	2,3	0.222	0.259
29	266.5743	-28.83541	WC	2	0.366	0.667
30	266.46089	-28.98879	WN	2,4,5	0.359	0.551
31	266.45185	-28.834709	WN	5	0.231	0.900
32	266.42696	-28.881472	WC	6	0.090	0.095
33	266.49075	-28.912806	WC	6	0.268	0.330
34	266.56456	-28.838492	WC	7	0.361	0.699
35	266.41381	-28.88923	OB	4,5	0.222	0.259

(a) References: (1) Mauerhan et al. (2010a); (2) Mauerhan et al. (2010b); (3) Mauerhan, Muno & Morris (2007); (4) Muno et al. (2006); (5) Cotera et al. (1999); (6) Homeier et al. (2003); (7) Figer, McLean & Morris (1999)

Table 4.3: In the Paα survey region, 35 massive stars are observed outside the three clusters (outside their approximate tidal radius) in the GC region. Among these massive stars are 24 Wolf-Rayet stars. The predicted number of massive stars of each model is presented below.

	$N_{massive}$ outside the clusters					
	WR-L=20$M_\odot$	StdDev	WR-L=40 $M_\odot$	StdDev	WR-L=60 $M_\odot$	StdDev
Q_{age}=4 Myr	62	$\sigma_{4,20} = 8$	**22**	$\sigma_{4,40} = 5$	11	$\sigma_{4,60} = 4$
Q_{age}=4.5 Myr	80	$\sigma_{4.5,20} = 12$	**30**	$\sigma_{4.5,40} = 4$	13	$\sigma_{4.5,60} = 2$
Q_{age}=5.0 Myr	68	$\sigma_{5,20} = 8$	**26**	$\sigma_{5,40} = 3$	10	$\sigma_{5,60} = 2$

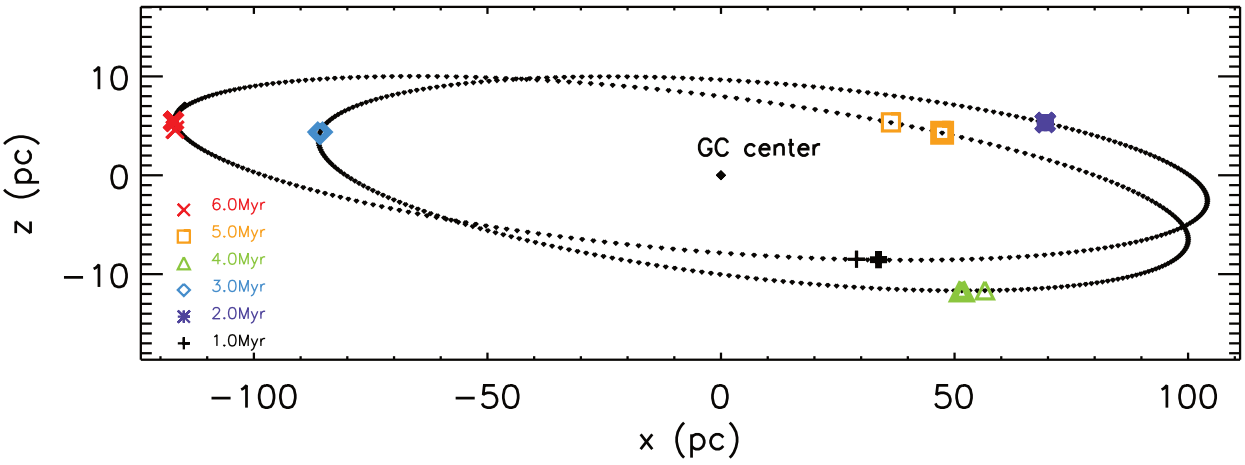

(a)

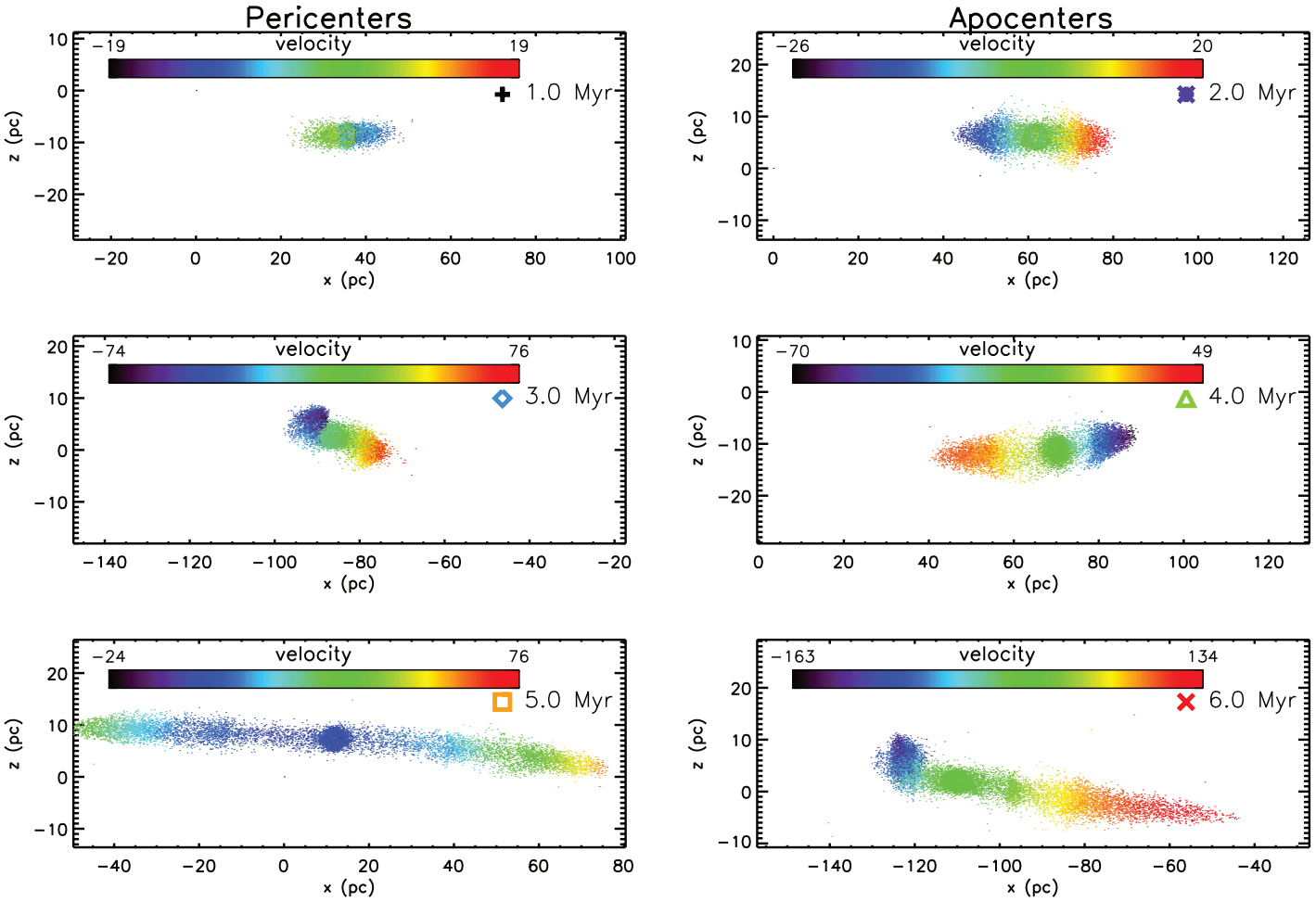

(b)

Figure 4.10: (Caption in the next page)

Figure 4.10: (From previous page) (a) The projected orbit of the cluster on the plane of the sky, xz-plane, is illustrated. The symbols on the orbit mark the apsides of the 3D orbit. Each symbol/color corresponds to a particular age. The thick symbols display the exact position of the apsides, while the thin symbols refer to the closest available snapshot of the simulated cluster by considering the time resolution of the simulations. (b) The projected snapshots of the cluster on the plane of the sky are shown at apocenters and pericenters. Each snapshot corresponds to one marked apside on the projected orbit. The sources are colored based on the present velocity variation in the cluster and its tidal tails.

Chapter 5

Summary and outlook

Massive stars are rare in the solar neighborhood, therefore, their IMF is less constrained and their formation scenarios are less understood. The center of our Galaxy hosts a rich population of massive stars which mostly live in three young starburst clusters: The Arches, Quintuplet and the Nuclear clusters (Krabbe et al., 1991; Nagata et al., 1995; Okuda et al., 1990; Becklin & Neugebauer, 1968). Besides, a population of apparently isolated massive stars is detected in the GC region (Dong et al., 2011a; Mauerhan et al., 2010a,b; Wang et al., 2010). The formation scenarios of the clusters and the observed isolated massive stars in the extreme environment of the GC are not known. It has been discussed that characteristics of the molecular clouds in the CMZ, for example high cloud temperatures and strong magnetic fields, influence the IMF (e.g. Morris, 1993; Klessen, Spaans & Jappsen, 2007). Formation of massive stars in isolation implies a very deviating IMF. A deviating IMF also has been suggested to describe the mass spectrum of the three clusters. Previous observations of the clusters in the GC have revealed a flat mass function in their central region (e.g. Stolte et al., 2005; Hußmann et al., 2012; Lu et al., 2013). However, the question of the IMF of the three clusters in the GC, as the most powerful tracer of their birth properties, is coupled with the dynamical evolution of the clusters. The dynamical evolution of star clusters in the GC region can become dramatic under the strong effect of the GC tidal field. With the aim to address the question of a deviating *initial* mass function in the GC environment, we compared the observed present-day mass function of the youngest cluster in the GC, the Arches cluster, with simulations of the cluster's dynamical evolution. We also analyzed N-body models of the cluster evolving in the GC tidal field to probe the contribution of drifted sources from the clusters to the observed population of isolated massive stars in the GC.

We analyzed high-resolution Ks and H -band adaptive optics data from VLT/NACO in combination with seeing-limited J-band observations from Subaru/Cisco of the Arches cluster. These observations allowed us to study the cluster out to its tidal radius for the first time. The extinction correction is a determining factor to interpret the observations towards the GC. Therefore, as a major part of our research on the Arches cluster, we studied the effects of the extinction law on the derived stellar parameters. We derived individual extinction values and stellar masses by dereddening of the cluster member candidates along the extinction law in the colour-magnitude diagram. The intersection of the line of reddening with a non-extincted 2.5 Myr theoretical isochrone at the distance of the GC determines the intrinsic magnitude and stellar mass of each star. A realistic extinction map of the cluster was constructed using a Bayesian method and by assuming two different extinction laws. Applying the Rieke & Lebofsky

(1985) extinction law ($A_\lambda \propto \lambda^{-1.61}$), which has been commonly used in previous studies toward the Arches cluster, we derived a high and variable extinction within the range of $2.7 < A_{Ks} < 4.5$ mag. The patchiness of the extinction map is high and hardly follows any trend; nevertheless, a region of relatively low extinction is present toward the center of the cluster. An area of high extinction is located in the southwest and partly northwest of the cluster. The extinction law derived by Nishiyama et al. (2009) similar to several recent studies toward the GC (e.g. Schödel et al., 2010; Stead & Hoare, 2009) suggests a steeper wavelength dependence of the infrared extinction law ($A_\lambda \propto \lambda^{-2}$). The obtained extinction values applying the Nishiyama et al. (2009) extinction law are lower on average by 24%, up to 1.1 mag lower in Ks-band as compared to the values derived assuming the Rieke & Lebofsky (1985) extinction law. A moderate change in the extinction law cause a substantial changes in the extinction measure of each star and alters the derived stellar masses. In this study, the initial mass of the most massive star in our sample decreases from 104 $M_\odot$ to 80 $M_\odot$ when using the steeper extinction law, i.e, by $\sim 30\%$. Such a decrease of the individual masses changes our understanding of these clusters, especially as the Arches cluster was used to derive a possible upper-mass limit of $M = 150\,M_\odot$ for the star formation process in the Milky Way (Figer, 2005).

In the study of the massive stellar population of the Arches cluster, we constructed the present-day mass function of the cluster in an area that reaches out to the tidal radius ($r_t \sim 1.6$ pc). The derived mass functions cover the high-mass part of the mass spectrum (present-day mass range: $10 - 66 M_\odot$) and are obtained in three different annuli: r < 0.2 pc (core), $0.2 <$ r < 0.4 (intermediate annulus), and $0.4 <$ r < 1.5 pc (outer annulus). The derived present-day mass function of the cluster using the Nishiyama et al. (2009) extinction law increases from a flat slope of $\alpha = -1.50 \pm 0.35$ in the core, compared to the Salpeter IMF with $\alpha = -2.3$, to $\alpha = -2.21 \pm 0.27$ in the intermediate annulus, and becomes deficient of massive stars, $\alpha = -3.21 \pm 0.30$, in the outer annulus. Our mass functions show that, while in the core of the cluster massive stars are more abundant compared to the standard Salpeter mass function ($\alpha = -2.35$, Salpeter 1955), the outskirts are depleted of high-mass stars. The steepening of the mass function toward the outskirts of the cluster guided us to investigate the dynamical state of the cluster. We compared the derived slope of the mass functions in different annuli with a series of dynamical N-body simulations with different assumed initial mass functions performed by Harfst, Portegies Zwart & Stolte (2010). The derived simulated slope from a Salpeter IMF model at the radius of 1 pc was in very good agreement with our finding. It was discussed previously that the IMF might be top-heavy in the GC because of increased magnetic fields and cloud temperatures (Morris 1993, Dib, Kim & Shadmehri 2007, see also 1.2.2.3 for discussions). However, our observations are consistent with the expectations of the dynamical evolution of the cluster starting from a Salpeter IMF at birth. We therefore do not need to invoke a primordially deviating flat mass function to explain the spatial distribution of stars in the Arches cluster (Habibi et al., 2013).

The comparison between the observed trend in the present-day mass function of the Arches cluster and N-body simulations revealed that the Arches cluster exhibits

characteristics of a cluster born with a normal IMF, which is, however, dynamically evolved. The dynamical evolution of young star clusters not only changes the distribution of stars inside the cluster, but also changes the distribution of field stars through tidal drift and high-speed escapers. Therefore, our finding motivated us to probe the contribution of drifted sources from the star clusters into the observed population of isolated massive stars in the GC (Dong et al. 2011a; Mauerhan et al. 2010a; Mauerhan et al. 2010b; Wang et al. 2010). As discussed in the introduction of this thesis (Sect. 1.1.1), most of the stars in the solar neighborhood are found to have formed in clusters (Lada & Lada, 2003; Gutermuth et al., 2011; Allen et al., 2007). Therefore, the detection of isolated massive stars in the GC has raised questions on their origin. Studies which focused on observations of massive field stars in our Galaxy (de Wit et al., 2004, 2005) found a predominant population of $\sim 95\%$ of all O-type stars can be considered as formed within a cluster environment. However, it is not clear if we can generalize these findings to the unique environment of the GC.

In our study, we analyzed N-body simulations of the dynamical evolution of the Arches cluster in the GC tidal field to create combined models of the Arches and Quintuplet clusters. The main goal was to compare the population of ejected and drifted massive sources in models of the two clusters to the HST/NICMOS Paschen-α survey of the Galactic center, which detected a population of isolated young massive stars in the GC region (Mauerhan et al., 2010a). The cluster models analyzed in this thesis are based on the work by Harfst, Portegies Zwart & Stolte (2010), in which the properties of the simulated cluster is fitted to the observational data from the central 0.4 pc of the Arches cluster (Stolte et al., 2005). For our study, this model was extended to incorporate the effect of the Galactic center tidal field.

The Arches and Quintuplet clusters share similar properties like their estimated mass (Hußmann (2014), Habibi et al. (2013), Clarkson et al. (2012)) and bulk motion velocity (Stolte et al., 2014a). This implies that to probe the contribution of GC star clusters to the observed population of isolated massive stars, we should take into account a possible contribution of both star clusters. Moreover, their similarity allowed us to use one set of models to probe their dynamical evolution. The Quintuplet cluster appears more dispersed (Figer, 2008) and is estimated to be older than the Arches cluster (Figer, McLean & Morris, 1999). Therefore, we assumed the Quintuplet cluster is a snapshot of the Arches cluster at older ages as it evolves in the GC region. The age of the Quintuplet cluster and the minimum initial mass of a WR progenitor star are two less constrained parameters which have a significant effect on the predicted number of WR stars outside the clusters in the GC region. Various models were constructed assuming different ages for the Quintuplet cluster and distinct values for the initial mass of a WR progenitor. We compared these models to the observed population of massive stars (Mauerhan et al., 2010a) by employing a method which calculates histogram differences of the spatial distributions of observed and simulated stars. Among all the models, the model which assumes an age of 5 Myr for the Quintuplet and an initial mass of $40\,M_{\odot}$ for a WR progenitor, is the most similar (best-matching) model to the spatial distribution of the observed isolated high-mass stars.

The trajectories of the sources in different mass ranges in the models indicate that

the tidal drifting of cluster stars by the GC potential is an effective process, which causes stars originating from both clusters to reach a maximum distance of 70 pc from the center of the Arches cluster. Both massive, $M > 40\,M_{\odot}$, and intermediate mass stars, $10\,M_{\odot} < M < 20\,M_{\odot}$, follow a similar pattern. The strong tidal field of the GC triggers the formation of extended tidal arms for both the Arches and Quintuplet clusters at their current age. The tidal structures of both clusters form as a result of velocity variation inside the cluster. During the evolution of the cluster along its orbit, as it moves away from the apocenter toward pericenter, its velocity increases, and consequently, individual orbits of stars on the tidal structures diverge spatially. As individual stars gain energy in the center of the cluster their velocity may exceed the cluster's escape velocity, and lie outside the varying tidal radius of the cluster. Consequently, they may be removed by the tidal field and form a tidal structure. The velocity variation along the tidal arms of the Arches cluster reaches $50\,\mathrm{kms}^{-1}$. This value is as high as $140\,\mathrm{kms}^{-1}$ for the Quintuplet cluster, which should be detectable in a proper motion survey using high precision astrometric studies of the Quintuplet's tidal tail.

The tidal arms of the Arches cluster appear stretched out to 20 pc in each direction on the plane of the sky, in the best-matching model. The tidal arms of the Quintuplet cluster extend out to 65 pc along the Galactic plane. These arms reproduce the observations of massive stars in the GC region (Mauerhan et al., 2010a) which reveal two strips along the Galactic plane with a prominent gap along the direction of the galactic poles. According to our models, the eastern projected tidal arm of the Quintuplet cluster at the age of 5 Myr reaches to the Sagittarius B2 region. This implies that the evolved massive stars observed in projection toward this region might originate in the tidally drifted sources from the Quintuplet cluster.

The quantitative comparison of the models to observed massive sources outside the clusters in the Paschen-α survey area is performed using two different methods. In the first method we constructed histograms of the spatial distributions of observed and simulated stars with reference to the center of the Arches cluster. Comparing histograms shows that the best-matching model reproduces 80% of the observed population out to 21 pc and 67% of the observed population out to a distance of 80 pc from the Arches cluster. As the second method, we constructed a density map of observed isolated massive stars using Voronoi diagrams. Based on the density map, we could calculate the probability of observing one or more stars in each Voronoi cell by assuming our best-matching model. In the case of 62% of the observed isolated massive stars, at least one of the ten random realizations of our best-matching model predicts a star that can explain the observed star. When we only consider the Voronoi cells within the central 20 pc from the center of the Arches cluster, this number increases to 72%. The best-matching model predicts 26 massive stars outside the clusters, as compared to the 35 observed massive stars outside the three clusters in the Paschen-α survey region. Our models do not include the Nuclear cluster, since we do not expect that ejected sources from the Nuclear cluster linger in the GC region. Based on the proper motion studies of stars in the central 1 pc of the GC (Schödel, Merritt & Eckart, 2009) and the maximum predicted ejection rate of hyper-velocity stars from the Nuclear cluster (Yu & Tremaine

(2003); Perets, Hopman & Alexander (2007)), we estimate ~ 1 star to be originated from the Nuclear cluster which contributes to the observed sample of massive stars in the GC at any given time. In Sect. 4.4.3 of this thesis, we discuss alternative scenarios for the origin of the isolated massive sources in the GC, for example supernova kicks or dynamical ejections involving tight initial binary systems. Currently, we can also not exclude the possibility that these high-mass stars might have formed in smaller clusters or in isolation. Our models can reproduce a considerable fraction of 60-80% of the observed population of isolated massive stars, depending on the method and the area in which we perform our comparative study. This finding opens up a new possibility for the origin of massive stars which are spread in the central 100 pc of our Galaxy (Habibi, Stolte & Harfst, 2014). Especially a very deviating IMF in the sense of truly isolated high-mass star formation seems not required to explain the WR population observed in the CMZ.

In summary, we have found that the Arches cluster is consistent with a normal Salpeter IMF at birth, the shape of which is altered by subsequent dynamical evolution. Comparing the distribution of observed isolated population of high-mass stars in the CMZ with models of dynamically drifted sources from the Arches and Quintuplet clusters, we also find that most massive stars in the GC environment can be explained as drifters from these two young starburst clusters. This leads us to the conclusion that the evidence for a strongly deviating *initial* stellar mass function in the wider GC environment is weak.

Outlook and future studies

Further observations of the Arches cluster

One useful supplementary observational effort to constrain properties of the Arches cluster is to perform a proper motion study in the outskirts of the cluster. The main goal is to derive the mass function of the cluster based on proper motion membership. Currently, the mass function of the proper motion members of the Arches cluster is available only in the central 0.4 pc (Stolte et al., 2008a; Clarkson et al., 2012). A study by Stolte et al. (2014b) has obtained a proper motion membership sample of the Arches cluster within $r < 1.5\,\mathrm{pc}$. This sample, which is based on two epochs of K_s-band observations, is used to investigate the circumstellar disc fraction of the cluster. Their proper motion member sample can provide a base for constructing the present-day mass function of the cluster. To measure the velocity dispersion of proper motion members, more epochs are needed. At the present time, proper motion studies of the outskirts of the Arches cluster are limited by the performance of the AO system which is sensitive to the location of the guide star in each observed field. As the Arches cluster is more compact compared to the Quintuplet cluster, it offers less bright guide stars for the AO correction in the outskirts of the cluster. If we measure a large velocity dispersion in the outskirts as compared to the central population of the cluster, it will support that the mass segregation is indeed a result of dynamical evolution. Contrarily, a smooth velocity distribution would favor the primordial segregation scenario. A proper motion

study from multiple epochs provides a higher astrometric accuracy, which would help to constrain the radial variation in the velocity dispersion. This study out to the Arches cluster's tidal radius would also provide a more realistic estimate of the dynamical mass of the cluster. The current dynamical mass might be underestimated in the presence of mass segregation, as suggested from the variation in the mass function slope and the comparison with dynamical models presented in this thesis.

In case further observations reveal that the velocity dispersion increases towards larger radii, as predicted by N-body simulations of the dynamical evolution of the cluster, the current estimate for the dynamical mass of the cluster needs to increase (Olczak & Stolte, 2014). The ideal ground-based proper motion study of the Arches outskirts needs an adaptive optics system with a laser guide star on an instrument with a large field of view which simultaneously covers the cluster center and the outskirts.

Further observations on the origin of isolated massive stars in the GC

One essential step forward toward answering the question of star formation in the GC region is to perform a deep spectral study of the areas around isolated massive stars, based on the comparative study that we performed during this thesis. The main goal would be to investigate whether the remaining population of isolated massive sources that we can not explain with our model have been formed in lower mass or already dissolved clusters. The integral-field spectrograph SINFONI at the VLT is able to provide observations with high-angular resolution and the required sensitivity. It is necessary to study surrounding main sequence stars that are not evolved to WR objects, using high S/N spectra in the heavily obscured GC region. Spectral observations can distinguish between the young main sequence candidates of the host cluster around the massive star and the evolved field population. The radial velocities of the detected main sequence or young stellar objects can be determined from the Doppler-shift of the prominent stellar lines. If the present dispersion of the observed radial velocities is small ($\sim$ 40km/s; Liermann, Hamann & Oskinova 2009), these sources can belong to the host cluster close to the target WR star. The measured radial velocities will be compared to the radial velocities of the atomic and molecular gas at similar galactocentric distances and also to the observed radial velocity of the Arches and Quintuplet clusters to deduce the most likely origin of these sources. Such spectroscopic studies will help to constrain whether some of the observed high-mass stars might still have formed in isolation or in smaller clusters. As discussed in this thesis, this will strengthen the final conclusions as to whether high-mass star formation and the high-mass IMF in the GC environment are different from moderate star-forming regions in the solar neighborhood, or whether the IMF is the same even for high-mass stars forming in the GC extreme environment.

Bibliography

Allen D. A., Hyland A. R., Hillier D. J., 1990, MNRAS, 244, 706 (Cited on page 14.)

Allen L. et al., 2007, Protostars and Planets V, 361 (Cited on pages 4 and 101.)

An D. et al., 2011, ApJ, 736, 133 (Cited on page 11.)

Andersen M., Zinnecker H., Moneti A., McCaughrean M. J., Brandl B., Brandner W., Meylan G., Hunter D., 2009, ApJ, 707, 1347 (Cited on page 9.)

Ankerst M., Kriegel H.-P., Seidl T., 1998, Knowledge and Data Engineering, IEEE Transactions on, 10, 996 (Cited on page 76.)

Aurenhammer F., Klein R., 2000, Handbook on Computational Geometry, Sack J., Urrutia G., eds., Elsevier Science Publishing, Amsterdam, pp. 201–290 (Cited on pages 56 and 82.)

Banerjee S., Kroupa P., Oh S., 2012, MNRAS, 426, 1416 (Cited on page 8.)

Bartko H. et al., 2009, ApJ, 697, 1741 (Cited on pages 14 and 15.)

Bartko H. et al., 2010, ApJ, 708, 834 (Cited on pages 14 and 15.)

Bastian N., Covey K. R., Meyer M. R., 2010, ARA&A, 48, 339 (Cited on pages iii, 5 and 6.)

Becklin E. E., Neugebauer G., 1968, ApJ, 151, 145 (Cited on pages 8, 10, 19 and 99.)

Beech M., Mitalas R., 1994, ApJS, 95, 517 (Cited on page 7.)

Binney J., Gerhard O. E., Stark A. A., Bally J., Uchida K. I., 1991, MNRAS, 252, 210 (Cited on page 13.)

Blaauw A., 1961, Bull. Astron. Inst. Netherlands, 15, 265 (Cited on page 84.)

Blum R. D., Schaerer D., Pasquali A., Heydari-Malayeri M., Conti P. S., Schmutz W., 2001, AJ, 122, 1875 (Cited on pages 16, 43, 64 and 71.)

Bonnell I. A., Rice W. K. M., 2008, Science, 321, 1060 (Cited on page 14.)

Brandner W., Clark J. S., Stolte A., Waters R., Negueruela I., Goodwin S. P., 2008, A&A, 478, 137 (Cited on page 8.)

Bressert E. et al., 2010, MNRAS, 409, L54 (Cited on page 4.)

Cardelli J. A., Clayton G. C., Mathis J. S., 1989, ApJ, 345, 245 (Cited on page 20.)

Carollo C. M., Stiavelli M., Mack J., 1998, AJ, 116, 68 (Cited on page 13.)

Carpenter J. M., 2000, AJ, 120, 3139 (Cited on page 4.)

Chabrier G., 2003, PASP, 115, 763 (Cited on page 5.)

Chabrier G., 2005, in Astrophysics and Space Science Library, Vol. 327, The Initial Mass Function 50 Years Later, Corbelli E., Palla F., Zinnecker H., eds., p. 41 (Cited on pages 5 and 9.)

Clarkson W. I., Ghez A. M., Morris M. R., Lu J. R., Stolte A., McCrady N., Do T., Yelda S., 2012, ApJ, 751, 132 (Cited on pages 16, 18, 62, 72, 85, 101 and 103.)

Comerón F., Pasquali A., 2005, A&A, 430, 541 (Cited on page 52.)

Cotera A. S., Erickson E. F., Colgan S. W. J., Simpson J. P., Allen D. A., Burton M. G., 1996, ApJ, 461, 750 (Cited on pages 8 and 16.)

Cotera A. S., Simpson J. P., Erickson E. F., Colgan S. W. J., Burton M. G., Allen D. A., 1999, ApJ, 510, 747 (Cited on pages 16 and 95.)

Crowther P. A., Schnurr O., Hirschi R., Yusof N., Parker R. J., Goodwin S. P., Kassim H. A., 2010, MNRAS, 408, 731 (Cited on page 7.)

Cutri R. M. et al., 2003, VizieR Online Data Catalog, 2246, 0 (Cited on page 70.)

de Mink S. E., Langer N., Izzard R. G., Sana H., de Koter A., 2013, ApJ, 764, 166 (Cited on page 5.)

de Wit W. J., Testi L., Palla F., Vanzi L., Zinnecker H., 2004, A&A, 425, 937 (Cited on pages 4 and 101.)

de Wit W. J., Testi L., Palla F., Zinnecker H., 2005, A&A, 437, 247 (Cited on pages 4 and 101.)

Devillard N., 2001, in Astronomical Society of the Pacific Conference Series, Vol. 238, Astronomical Data Analysis Software and Systems X, Harnden Jr. F. R., Primini F. A., Payne H. E., eds., p. 525 (Cited on page 33.)

Dib S., Kim J., Shadmehri M., 2007, MNRAS, 381, L40 (Cited on pages 66 and 100.)

Diolaiti E., Bendinelli O., Bonaccini D., Close L., Currie D., Parmeggiani G., 2000, A&AS, 147, 335 (Cited on page 30.)

Do T., Lu J. R., Ghez A. M., Morris M. R., Yelda S., Martinez G. D., Wright S. A., Matthews K., 2013, ApJ, 764, 154 (Cited on page 14.)

Dong H. et al., 2011a, MNRAS, 417, 114 (Cited on pages 11, 18, 68, 99 and 101.)

Dong H. et al., 2011b, in Astronomical Society of the Pacific Conference Series, Vol. 439, The Galactic Center: a Window to the Nuclear Environment of Disk Galaxies, Morris M. R., Wang Q. D., Yuan F., eds., p. 104 (Cited on pages 18 and 68.)

Dong H., Wang Q. D., Morris M. R., 2012, MNRAS, 425, 884 (Cited on pages 56 and 70.)

Eckart A., Genzel R., Hofmann R., Sams B. J., Tacconi-Garman L. E., 1993, ApJ, 407, L77 (Cited on page 68.)

Eddington A. S., 1926, The Internal Constitution of the Stars (Cited on page 7.)

Eggleton P. P., Fitchett M. J., Tout C. A., 1989, ApJ, 347, 998 (Cited on page 71.)

Eisenhauer F. et al., 2005, ApJ, 628, 246 (Cited on page 14.)

Ekström S. et al., 2012, A&A, 537, A146 (Cited on page 73.)

Eldridge J. J., Tout C. A., 2004, MNRAS, 353, 87 (Cited on page 73.)

Elmegreen B. G., Klessen R. S., Wilson C. D., 2008, ApJ, 681, 365 (Cited on page 17.)

Englmaier P., Gerhard O., 1999, MNRAS, 304, 512 (Cited on page 13.)

Espinoza P., Selman F. J., Melnick J., 2009, A&A, 501, 563 (Cited on pages v, 16, 17, 19, 22, 34, 42, 43, 50, 51, 52, 56, 57, 60, 62, 64, 68, 71 and 77.)

Ferrière K., Gillard W., Jean P., 2007, A&A, 467, 611 (Cited on pages 11 and 68.)

Figer D. F., 1995, PhD thesis, UNIVERSITY OF CALIFORNIA, LOS ANGELES. (Cited on page 70.)

Figer D. F., 2004, in Astronomical Society of the Pacific Conference Series, Vol. 322, The Formation and Evolution of Massive Young Star Clusters, Lamers H. J. G. L. M., Smith L. J., Nota A., eds., p. 49 (Cited on pages 15 and 41.)

Figer D. F., 2005, Nature, 434, 192 (Cited on pages 7, 16, 17, 60 and 100.)

Figer D. F., 2008, in IAU Symposium, Vol. 250, IAU Symposium, Bresolin F., Crowther P. A., Puls J., eds., pp. 247–256 (Cited on pages 72, 77 and 101.)

Figer D. F., Kim S. S., Morris M., Serabyn E., Rich R. M., McLean I. S., 1999, ApJ, 525, 750 (Cited on pages 8, 16, 17, 19, 42 and 68.)

Figer D. F., McLean I. S., Morris M., 1995, ApJ, 447, L29 (Cited on page 15.)

Figer D. F., McLean I. S., Morris M., 1999, ApJ, 514, 202 (Cited on pages 15, 16, 59, 72, 73, 95 and 101.)

Figer D. F., Morris M., 2002, in Astronomical Society of the Pacific Conference Series, Vol. 285, Modes of Star Formation and the Origin of Field Populations, Grebel E. K., Brandner W., eds., p. 381 (Cited on page 68.)

Figer D. F., Morris M., McLean I. S., 1996, in Astronomical Society of the Pacific Conference Series, Vol. 102, The Galactic Center, Gredel R., ed., p. 263 (Cited on page 15.)

Figer D. F. et al., 2002, ApJ, 581, 258 (Cited on pages v, 16, 18, 50, 51, 52, 68 and 71.)

Figer D. F., Najarro F., Morris M., McLean I. S., Geballe T. R., Ghez A. M., Langer N., 1998, ApJ, 506, 384 (Cited on page 16.)

Fitzpatrick E. L., 2004, in Astronomical Society of the Pacific Conference Series, Vol. 309, Astrophysics of Dust, Witt A. N., Clayton G. C., Draine B. T., eds., p. 33 (Cited on pages 42 and 56.)

Fruchter A. S., Hook R. N., 2002, PASP, 114, 144 (Cited on pages 28 and 30.)

Gaume R. A., Claussen M. J., de Pree C. G., Goss W. M., Mehringer D. M., 1995, ApJ, 449, 663 (Cited on page 11.)

Geballe T. R., Najarro F., Figer D. F., 2000, ApJ, 530, L97 (Cited on page 16.)

Gennaro M., Brandner W., Stolte A., Henning T., 2011, MNRAS, 412, 2469 (Cited on page 8.)

Genzel R., Eisenhauer F., Gillessen S., 2010, Reviews of Modern Physics, 82, 3121 (Cited on page 14.)

Genzel R. et al., 2003, ApJ, 594, 812 (Cited on page 15.)

Genzel R., Thatte N., Krabbe A., Kroker H., Tacconi-Garman L. E., 1996, ApJ, 472, 153 (Cited on page 14.)

Gerhard O., 2001, ApJ, 546, L39 (Cited on page 14.)

Ghez A. M. et al., 2003, ApJ, 586, L127 (Cited on page 14.)

Ghez A. M., Salim S., Hornstein S. D., Tanner A., Lu J. R., Morris M., Becklin E. E., Duchêne G., 2005, ApJ, 620, 744 (Cited on page 14.)

Ghez A. M. et al., 2008, ApJ, 689, 1044 (Cited on pages 13, 43, 67 and 69.)

Gies D. R., Bolton C. T., 1986, ApJS, 61, 419 (Cited on pages 19, 69 and 85.)

Gillessen S., Eisenhauer F., Fritz T. K., Bartko H., Dodds-Eden K., Pfuhl O., Ott T., Genzel R., 2009, ApJ, 707, L114 (Cited on pages 67 and 69.)

Goodwin S. P., Bastian N., 2006, MNRAS, 373, 752 (Cited on page 10.)

Gutermuth R. A., Pipher J. L., Megeath S. T., Myers P. C., Allen L. E., Allen T. S., 2011, ApJ, 739, 84 (Cited on pages 4 and 101.)

Gvaramadze V. V., Bomans D. J., 2008, A&A, 490, 1071 (Cited on pages 4, 18 and 68.)

Habibi M., Stolte A., Brandner W., Hußmann B., Motohara K., 2013, A&A, 556, A26 (Cited on pages 68, 72, 73, 77, 100 and 101.)

Habibi M., Stolte A., Harfst S., 2014, A&A, 566, A6 (Cited on page 103.)

Hafner J., Sawhney H., Equitz W., Flickner M., W. N., 1995, EEE TRANSACTIONS ON PATTERN ANALYSIS AND MACHINE INTELLIGENCE, 17, 729 (Cited on pages 75 and 76.)

Hamann W.-R., Gräfener G., Liermann A., 2006, A&A, 457, 1015 (Cited on page 74.)

Harayama Y., Eisenhauer F., Martins F., 2008, ApJ, 675, 1319 (Cited on page 8.)

Harfst S., Portegies Zwart S., Stolte A., 2010, MNRAS, 409, 628 (Cited on pages vii, 17, 19, 42, 59, 60, 61, 66, 68, 69, 71, 100 and 101.)

Harris W. E., 1996, AJ, 112, 1487 (Cited on page 10.)

Hasegawa T., Sato F., Whiteoak J. B., Miyawaki R., 1994, ApJ, 429, L77 (Cited on pages 12 and 13.)

Hillebrandt W., Thielemann F.-K., Langer N., 1987, ApJ, 321, 761 (Cited on page 7.)

Hills J. G., 1988, Nature, 331, 687 (Cited on page 73.)

Homeier N. L., Blum R. D., Pasquali A., Conti P. S., Damineli A., 2003, A&A, 408, 153 (Cited on pages 15 and 95.)

Hußmann B., 2014, PhD thesis, Universität Bonn <EMAIL>hussmann@astro.uni-bonn.de</EMAIL> (Cited on pages 16, 26, 72, 73 and 101.)

Hußmann B., Stolte A., Brandner W., Gennaro M., Liermann A., 2012, A&A, 540, A57 (Cited on pages 8, 16, 19, 57, 64, 68, 77 and 99.)

Hut P., 2003, in IAU Symposium, Vol. 208, Astrophysical Supercomputing using Particle Simulations, Makino J., Hut P., eds., p. 331 (Cited on page 71.)

Iye M. et al., 2004, PASJ, 56, 381 (Cited on page 22.)

Jeans J. H., 1919, Problems of cosmogony and stellar dynamics (Cited on page 9.)

Kahn F. D., 1974, A&A, 37, 149 (Cited on page 7.)

Kendrew S., Ginsburg A., Johnston K., Beuther H., Bally J., Cyganowski C. J., Battersby C., 2013, ApJ, 775, L50 (Cited on page 11.)

Kim S. S., Figer D. F., Kudritzki R. P., Najarro F., 2006, ApJ, 653, L113 (Cited on pages 17, 42, 49, 59 and 60.)

Kim S. S., Figer D. F., Lee H. M., Morris M., 2000, ApJ, 545, 301 (Cited on pages 17, 19, 62 and 69.)

Kim S. S., Figer D. F., Lee M. G., 2006, PASP, 118, 62 (Cited on page 52.)

Kim S. S., Morris M., 2003, ApJ, 597, 312 (Cited on page 14.)

King I. R., 1966, AJ, 71, 64 (Cited on page 71.)

Klessen R. S., Spaans M., Jappsen A.-K., 2007, MNRAS, 374, L29 (Cited on pages 9, 17, 66 and 99.)

Koen C., 2006, MNRAS, 365, 590 (Cited on page 7.)

Krabbe A., Genzel R., Drapatz S., Rotaciuc V., 1991, ApJ, 382, L19 (Cited on pages 10 and 99.)

Krabbe A. et al., 1995, ApJ, 447, L95 (Cited on page 14.)

Kroupa P., 2001, MNRAS, 322, 231 (Cited on pages 5, 9 and 10.)

Kroupa P., 2002, Science, 295, 82 (Cited on pages 5 and 9.)

Kroupa P., Weidner C., Pflamm-Altenburg J., Thies I., Dabringhausen J., Marks M., Maschberger T., 2013, The Stellar and Sub-Stellar Initial Mass Function of Simple and Composite Populations, Oswalt T. D., Gilmore G., eds., p. 115 (Cited on page 5.)

Kudryavtseva N. et al., 2012, ApJ, 750, L44 (Cited on page 8.)

Kuiper R., Klahr H., Beuther H., Henning T., 2010, ApJ, 722, 1556 (Cited on page 7.)

Küpper A. H. W., Kroupa P., Baumgardt H., Heggie D. C., 2010, MNRAS, 401, 105 (Cited on page 87.)

Lada C. J., Lada E. A., 2003, ARA&A, 41, 57 (Cited on pages 3, 4, 18, 68 and 101.)

Lang C. C., Goss W. M., Rodriguez L. F., 2001, in IAU Symposium, Vol. 205, Galaxies and their Constituents at the Highest Angular Resolutions, Schilizzi R. T., ed., p. 276 (Cited on page 57.)

Langer N., 1998, A&A, 329, 551 (Cited on page 71.)

Larsen S. S., Brodie J. P., Hunter D. A., 2004, AJ, 128, 2295 (Cited on page 10.)

Larson R. B., Starrfield S., 1971, A&A, 13, 190 (Cited on page 7.)

Launhardt R., Zylka R., Mezger P. G., 2002a, A&A, 384, 112 (Cited on page 11.)

Launhardt R., Zylka R., Mezger P. G., 2002b, A&A, 384, 112 (Cited on page 62.)

Law C., Yusef-Zadeh F., 2003, Astronomische Nachrichten Supplement, 324, 271 (Cited on page 57.)

Lawrence A. et al., 2007, MNRAS, 379, 1599 (Cited on page 34.)

Lebofsky M. J., 1979, AJ, 84, 324 (Cited on page 19.)

Lee E. J., Murray N., Rahman M., 2012, ApJ, 752, 146 (Cited on page 11.)

Lejeune T., Schaerer D., 2001, A&A, 366, 538 (Cited on page 43.)

Lenzen R. et al., 2003, in Society of Photo-Optical Instrumentation Engineers (SPIE) Conference Series, Vol. 4841, Instrument Design and Performance for Optical/Infrared Ground-based Telescopes, Iye M., Moorwood A. F. M., eds., pp. 944–952 (Cited on page 21.)

Liermann A., Hamann W.-R., Oskinova L. M., 2009, A&A, 494, 1137 (Cited on pages 16 and 104.)

Liermann A., Hamann W.-R., Oskinova L. M., 2012, A&A, 540, A14 (Cited on pages 15 and 73.)

Liermann A., Hamann W.-R., Oskinova L. M., Todt H., Butler K., 2010, A&A, 524, A82 (Cited on pages 15, 16 and 73.)

Lim B., Chun M.-Y., Sung H., Park B.-G., Lee J.-J., Sohn S. T., Hur H., Bessell M. S., 2013, AJ, 145, 46 (Cited on page 8.)

Lis D. C., Goldsmith P. F., 1990, ApJ, 356, 195 (Cited on page 11.)

Longmore S. N. et al., 2013, MNRAS, 433, L15 (Cited on pages iii, 12 and 13.)

Longmore S. N. et al., 2012, ApJ, 746, 117 (Cited on pages 13 and 85.)

Lu J. R., Do T., Ghez A. M., Morris M. R., Yelda S., Matthews K., 2013, ApJ, 764, 155 (Cited on pages 14, 15 and 99.)

Lu J. R., Ghez A. M., Hornstein S. D., Morris M., Matthews K., Thompson D. J., Becklin E. E., 2006, Journal of Physics Conference Series, 54, 279 (Cited on page 15.)

Lu J. R., Ghez A. M., Hornstein S. D., Morris M. R., Becklin E. E., Matthews K., 2009, ApJ, 690, 1463 (Cited on page 15.)

Lucas P. W. et al., 2008, MNRAS, 391, 136 (Cited on pages 22, 34 and 57.)

Lutz D. et al., 1996, A&A, 315, L269 (Cited on page 20.)

Maíz Apellániz J., 2008, ApJ, 677, 1278 (Cited on page 7.)

Maíz Apellániz J., Úbeda L., 2005, ApJ, 629, 873 (Cited on page 57.)

Marco O., Chauvin G., Ageorges N., Hainaut O., Kaufer A., 2007, in , Vol. 81 (Cited on page 28.)

Martin A. H. M., Downes D., 1972, Astrophys. Lett., 11, 219 (Cited on page 11.)

Martins F., Gillessen S., Eisenhauer F., Genzel R., Ott T., Trippe S., 2008a, ApJ, 672, L119 (Cited on page 14.)

Martins F., Hillier D. J., Paumard T., Eisenhauer F., Ott T., Genzel R., 2008b, A&A, 478, 219 (Cited on pages 16, 41, 43, 64 and 71.)

Massey P., Hunter D. A., 1998, ApJ, 493, 180 (Cited on page 9.)

Mauerhan J. C., Cotera A., Dong H., Morris M. R., Wang Q. D., Stolovy S. R., Lang C., 2010a, ApJ, 725, 188 (Cited on pages vii, viii, xi, 11, 16, 18, 19, 68, 69, 70, 77, 78, 80, 81, 83, 84, 88, 95, 99, 101 and 102.)

Mauerhan J. C., Muno M. P., Morris M., 2007, ApJ, 662, 574 (Cited on page 95.)

Mauerhan J. C., Muno M. P., Morris M. R., Stolovy S. R., Cotera A., 2010b, ApJ, 710, 706 (Cited on pages 11, 18, 68, 70, 79, 95, 99 and 101.)

McMillan S. L. W., 1996, in Astronomical Society of the Pacific Conference Series, Vol. 90, The Origins, Evolution, and Destinies of Binary Stars in Clusters, Milone E. F., Mermilliod J.-C., eds., p. 413 (Cited on page 71.)

Mehringer D. M., Menten K. M., 1997, ApJ, 474, 346 (Cited on page 11.)

Mengel S., Lehnert M. D., Thatte N., Genzel R., 2002, A&A, 383, 137 (Cited on page 10.)

Meynet G., Maeder A., 2003, A&A, 404, 975 (Cited on page 74.)

Mezger P. G., Zylka R., Philipp S., Launhardt R., 1999, A&A, 348, 457 (Cited on page 71.)

Molinari S. et al., 2011, ApJ, 735, L33 (Cited on pages iii, 12 and 13.)

Moneti A., Glass I. S., Moorwood A. F. M., 1994, MNRAS, 268, 194 (Cited on page 15.)

Morris M., 1993, ApJ, 408, 496 (Cited on pages 17, 66, 99 and 100.)

Morris M., Serabyn E., 1996a, ARA&A, 34, 645 (Cited on pages 10, 11 and 19.)

Morris M., Serabyn E., 1996b, ARA&A, 34, 645 (Cited on page 68.)

Motohara K. et al., 2002, PASJ, 54, 315 (Cited on page 22.)

Muno M. P. et al., 2009, VizieR Online Data Catalog, 218, 10110 (Cited on page 70.)

Muno M. P., Bower G. C., Burgasser A. J., Baganoff F. K., Morris M. R., Brandt W. N., 2006, ApJ, 638, 183 (Cited on page 95.)

Nagata T., Woodward C. E., Shure M., Kobayashi N., 1995, AJ, 109, 1676 (Cited on pages 8, 10, 16 and 99.)

Nagata T., Woodward C. E., Shure M., Pipher J. L., Okuda H., 1990, ApJ, 351, 83 (Cited on pages 8 and 15.)

Nagayama T. et al., 2003, in Society of Photo-Optical Instrumentation Engineers (SPIE) Conference Series, Vol. 4841, Instrument Design and Performance for Optical/Infrared Ground-based Telescopes, Iye M., Moorwood A. F. M., eds., pp. 459–464 (Cited on pages 56 and 70.)

Najarro F., Figer D. F., Hillier D. J., Kudritzki R. P., 2004, ApJ, 611, L105 (Cited on pages 16, 41, 43, 64, 71 and 72.)

Nishiyama S. et al., 2006, ApJ, 638, 839 (Cited on pages 49, 56 and 59.)

Nishiyama S., Tamura M., Hatano H., Kato D., Tanabé T., Sugitani K., Nagata T., 2009, ApJ, 696, 1407 (Cited on pages v, vi, xi, 20, 43, 44, 46, 47, 48, 55, 59, 64, 65 and 100.)

Odenkirchen M. et al., 2001, ApJ, 548, L165 (Cited on pages 19 and 69.)

Oey M. S., Clarke C. J., 2005, ApJ, 620, L43 (Cited on page 7.)

Offner S. S. R., Clark P. C., Hennebelle P., Bastian N., Bate M. R., Hopkins P. F., Moraux E., Whitworth A. P., 2013, ArXiv e-prints (Cited on page 5.)

Okuda H. et al., 1990, ApJ, 351, 89 (Cited on pages 8, 10, 15 and 99.)

Olczak C., Kaczmarek T., Harfst S., Pfalzner S., Portegies Zwart S., 2012, ApJ, 756, 123 (Cited on page 71.)

Olczak C., Stolte A., 2014, In prepration (Cited on page 104.)

Oskinova L. M., Steinke M., Hamann W.-R., Sander A., Todt H., Liermann A., 2013, MNRAS, 436, 3357 (Cited on pages 18 and 68.)

Pang X., Grebel E. K., Allison R. J., Goodwin S. P., Altmann M., Harbeck D., Moffat A. F. J., Drissen L., 2013, ApJ, 764, 73 (Cited on pages 8 and 9.)

Paresce F., De Marchi G., 2000, ApJ, 534, 870 (Cited on page 5.)

Paumard T. et al., 2006, ApJ, 643, 1011 (Cited on pages 14 and 15.)

Perets H. B., Hopman C., Alexander T., 2007, ApJ, 656, 709 (Cited on pages 73 and 103.)

Phillips A. C., Illingworth G. D., MacKenty J. W., Franx M., 1996, AJ, 111, 1566 (Cited on page 13.)

Pilbratt G. L. et al., 2010, A&A, 518, L1 (Cited on page 12.)

Porras A., Christopher M., Allen L., Di Francesco J., Megeath S. T., Myers P. C., 2003, AJ, 126, 1916 (Cited on page 4.)

Portegies Zwart S. F., Makino J., McMillan S. L. W., Hut P., 1999, A&A, 348, 117 (Cited on page 8.)

Portegies Zwart S. F., Makino J., McMillan S. L. W., Hut P., 2001a, ApJ, 546, L101 (Cited on pages 19, 69 and 85.)

Portegies Zwart S. F., Makino J., McMillan S. L. W., Hut P., 2002, ApJ, 565, 265 (Cited on page 62.)

Portegies Zwart S. F., McMillan S. L. W., Gerhard O., 2003, ApJ, 593, 352 (Cited on page 14.)

Portegies Zwart S. F., McMillan S. L. W., Hut P., Makino J., 2001b, MNRAS, 321, 199 (Cited on page 71.)

Portegies Zwart S. F., Verbunt F., 1996, A&A, 309, 179 (Cited on page 71.)

Poveda A., Ruiz J., Allen C., 1967, Boletin de los Observatorios Tonantzintla y Tacubaya, 4, 86 (Cited on pages 19, 69 and 85.)

Qin S.-L., Schilke P., Rolffs R., Comito C., Lis D. C., Zhang Q., 2011, A&A, 530, L9 (Cited on page 11.)

Rieke G. H., Lebofsky M. J., 1985, ApJ, 288, 618 (Cited on pages v, vi, xi, 19, 42, 43, 46, 47, 48, 51, 53, 54, 55, 56, 59, 65, 66, 99 and 100.)

Rieke G. H., Rieke M. J., Paul A. E., 1989, ApJ, 336, 752 (Cited on pages 42, 49 and 59.)

Rousset G. et al., 2003, in Society of Photo-Optical Instrumentation Engineers (SPIE) Conference Series, Vol. 4839, Adaptive Optical System Technologies II, Wizinowich P. L., Bonaccini D., eds., pp. 140–149 (Cited on page 21.)

Salpeter E. E., 1955, ApJ, 121, 161 (Cited on pages 4, 5, 9, 19, 42, 59, 60, 66, 68, 71 and 100.)

Sana H. et al., 2012, Science, 337, 444 (Cited on pages 5 and 84.)

Sander A., Hamann W.-R., 2012, in Astronomical Society of the Pacific Conference Series, Vol. 465, Proceedings of a Scientific Meeting in Honor of Anthony F. J. Moffat, Drissen L., Rubert C., St-Louis N., Moffat A. F. J., eds., p. 243 (Cited on page 74.)

Sato F., Hasegawa T., Whiteoak J. B., Miyawaki R., 2000, ApJ, 535, 857 (Cited on pages 11 and 12.)

Scalo J., 1998, in Astronomical Society of the Pacific Conference Series, Vol. 142, The Stellar Initial Mass Function (38th Herstmonceux Conference), Gilmore G., Howell D., eds., p. 201 (Cited on page 9.)

Schilbach E., Röser S., 2008, A&A, 489, 105 (Cited on page 4.)

Schneider F. R. N. et al., 2014, ApJ, 780, 117 (Cited on pages 7 and 8.)

Schödel R., Genzel R., Ott T., Eckart A., 2003, Astronomische Nachrichten Supplement, 324, 535 (Cited on page 14.)

Schödel R., Merritt D., Eckart A., 2009, A&A, 502, 91 (Cited on pages 73 and 102.)

Schödel R., Najarro F., Muzic K., Eckart A., 2010, A&A, 511, A18 (Cited on pages 20, 44, 64 and 100.)

Schwarzschild M., Härm R., 1959, ApJ, 129, 637 (Cited on page 7.)

Selman F. J., Melnick J., 2013, A&A, 552, A94 (Cited on page 9.)

Smith L. J., Gallagher J. S., 2001, MNRAS, 326, 1027 (Cited on page 10.)

Stead J. J., Hoare M. G., 2009, MNRAS, 400, 731 (Cited on pages 20, 44, 64 and 100.)

Sternberg A., 1998, ApJ, 506, 721 (Cited on page 10.)

Stolte A., 2003, PhD thesis, PhD Thesis, Combined Faculties for the Natural Sciences and for Mathematics of the Ruperto-Carola University of Heidelberg, Germany for the degree of Doctor of Natural Sciences. III + 156 pp. (2003) (Cited on page 22.)

Stolte A., Brandner W., Brandl B., Zinnecker H., Grebel E. K., 2004, AJ, 128, 765 (Cited on page 8.)

Stolte A., Brandner W., Grebel E. K., Lenzen R., Lagrange A.-M., 2005, ApJ, 628, L113 (Cited on pages vii, 8, 17, 19, 22, 42, 60, 61, 66, 68, 71, 99 and 101.)

Stolte A., Ghez A. M., Morris M., Lu J. R., Brandner W., Matthews K., 2008a, ApJ, 675, 1278 (Cited on pages 13, 18, 72, 77 and 103.)

Stolte A., Ghez A. M., Morris M. R., Lu J. R., Brandner W., Matthews K., 2008b, Journal of Physics Conference Series, 131, 012015 (Cited on pages 72 and 86.)

Stolte A., Grebel E. K., Brandner W., Figer D. F., 2002, A&A, 394, 459 (Cited on pages 16, 42, 43, 57 and 59.)

Stolte A. et al., 2014a, ApJ, 789, 115 (Cited on pages 72, 85 and 101.)

Stolte A., Hußmann B., Olczak C., Brandner W., Habibi M., Ghez A. M., Morris M., Lu J. R., 2014b, Submitted to A&A (Cited on pages 53 and 103.)

Stone R. C., 1991, AJ, 102, 333 (Cited on page 84.)

Strehl K., 1902, Zeitschrift fur Instrumentenkunde, 22, 213 (Cited on page 32.)

Sung H., Bessell M. S., 2004, AJ, 127, 1014 (Cited on page 8.)

Tody D., 1993, in Astronomical Society of the Pacific Conference Series, Vol. 52, Astronomical Data Analysis Software and Systems II, Hanisch R. J., Brissenden R. J. V., Barnes J., eds., p. 173 (Cited on page 26.)

Tout C. A., Aarseth S. J., Pols O. R., Eggleton P. P., 1997, MNRAS, 291, 732 (Cited on page 71.)

Wang Q. D. et al., 2010, MNRAS, 402, 895 (Cited on pages 11, 18, 68, 69, 99 and 101.)

Weidner C., Kroupa P., 2004, MNRAS, 348, 187 (Cited on page 7.)

Weidner C., Kroupa P., Maschberger T., 2009, MNRAS, 393, 663 (Cited on page 7.)

Werner M. W. et al., 2004, ApJS, 154, 1 (Cited on page 4.)

Whitmore B. C., Zhang Q., Leitherer C., Fall M., Schweizer F., Miller B. W., 1999, in Bulletin of the American Astronomical Society, Vol. 31, American Astronomical Society Meeting Abstracts #194, p. 843 (Cited on page 10.)

Williams J. P., Blitz L., McKee C. F., 2000, Protostars and Planets IV, 97 (Cited on page 19.)

Wolfire M. G., Cassinelli J. P., 1987, ApJ, 319, 850 (Cited on page 7.)

Yorke H. W., Sonnhalter C., 2002, ApJ, 569, 846 (Cited on page 7.)

Yu Q., Tremaine S., 2003, ApJ, 599, 1129 (Cited on pages 73 and 102.)

Yusef-Zadeh F. et al., 2009, ApJ, 702, 178 (Cited on pages 11 and 41.)

Zinnecker H., Yorke H. W., 2007, ARA&A, 45, 481 (Cited on pages 18 and 68.)

Acknowledgements

Doing this PhD was my first step to enter an amazing new world. I had dreamed about being involved in research since I was a child. The real world of research, although tougher than what I expected, proved to be as amazing and rewarding as I envisioned. More than anything, I am happy that after all the ups and downs, my passion is still alive, becoming deeper and deeper.

First, and foremost I want to thank my supervisor, Dr. Andrea Stolte, for giving me this opportunity and for introducing me to the wonders and frustrations of scientific research. I have learned a lot from her precision and scientific honesty. I am also grateful for the opportunities to travel and attend different conferences and schools. Thank you for all the insightful discussions, guidance, lots of patience and of course all the home-made bread!

My special thanks to Dr. Wolfgang Brandner for providing part of the data which are analysed in this thesis, and for helpful comments. Also, thanks for stimulating discussions and wonderful time in Heidelberg!

Thanks to Dr. Stefan Harfst for a great collaboration, providing models and guiding me to analyse them.

I would like to thank Dr. Adriane Liermann, Dr. Christoph Olczak, and Dr. Douglas Applegate for very useful discussions about my research.

Dr. Benjamin Hussman, thank you for answering my many questions, patiently and so precisely.

Prof. Norbert Langer, I am very grateful for your support and would like to thank for your interest in my research, and also for accepting our "Emmy Noether group" in your lively and friendly research group.

Prof. Pavel Kroupa, thank you for letting me be a part of your 16:16 seminars. The seminars helped me to gain so many ideas.

I also want to thank the members of my examination board, specially Dr. Kerp who kindly accepted to be on the board on a short notice.

To all the colleagues and friends I met in Bonn and Cologne, I want to thank you for the great time; in particular Nicolas Gonzalez Jimenez, Dr. Alexandra Kozyreva, Dr. Mohammad Zamaninasab, Dr. Hanyeh Mahmoudian, Dr. Sambaran Banerjee, Dr. Jonathan Mackey. I especially thank Zeinab Shafiee for all the wonderful break

times in AIfA .

I can never thank enough my parents, Zahra Tehranchi and Mohammad Habibi, for their love and lifetime support and their inspirational faith in good. "Baba", thank you for your optimism, encouragement and reminding me the beauty of life. "Maman", thank you for all the dreams I inherited from you and for your trust and faith in me.

My special thanks to my lifetime friend, soon to be Dr. Sepideh Pashami, for her company. It was great that I could discuss everything with you from my work to deepest thoughts and concerns, even when there was a cold sea between us.

Last but certainly not least, I want to thank Dr. Masoud Abkenar, with whom I've discussed my work more than any colleague. Thank you for listening to all my frustrated complaints and excited midnight speeches. This thesis would not have been written without your immense support.